# Numerical modeling of streamer discharges in preparation of the TARANIS space mission

Mohand Ameziane Ihaddadene

# UNIVERSITÉ D'ORLÉANS

## ÉCOLE DOCTORALE

## ÉNERGIE-MATÉRIAUX-SCIENCES DE LA TERRE ET DE L'UNIVERS

ÉQUIPE de RECHERCHE et LABORATOIRE :

Plasmas Spatiaux, Laboratoire de Physique et Chimie de l'Environnement et de l'Espace (LPC2E)

**THÈSE** présentée par :

**Mohand Ameziane Ihaddadene**

soutenue le : **06 Décembre 2016**

pour obtenir le grade de : **Docteur de l'Université d'Orléans**

Discipline/ Spécialité : **Physique**

# Numerical Modeling of Streamer Discharges in Preparation of the TARANIS Space Mission

**THÈSE dirigée par :**

| | |
|---|---|
| **Michel Tagger** | Professeur, Directeur du LPC2E, France |

**RAPPORTEURS :**

| | |
|---|---|
| **Ningyu Liu** | Professeur, University of New Hampshire, NH, USA |
| **Serge Soula** | Professeur, Université de Toulouse, France |

---

**JURY :**

| | |
|---|---|
| **Anne Bourdon** | Directeur de Recherche, Ecole Polytechnique, Palaiseau, France |
| **Jean-Louis Pinçon** | Chargé de Recherche, LPC2E, Orléans, France |
| **Michel Tagger** | Professeur, Directeur du LPC2E, Orléans, France |
| **Ningyu Liu** | Professeur, University of New Hampshire, NH, USA |
| **Sébastien Célestin** | Maître de Conférences, Université d'Orléans, France |
| **Serge Soula** | Professeur, Université de Toulouse, France |
| **Thomas Farges** | Ingénieur Checheur, CEA, DAM, DIF, Arpajon, France |

# Table of Contents

# List of Figures

# List of Tables

# Acknowledgments

My sincere gratitude go to Michel Tagger, the Head of the LPC2E, for his mentoring and encouragement during my PhD thesis. I would like to thank deeply my research advisor Sebastien Celestin for his guidance during these three years of PhD and I am very grateful for his great support, enormous help, patience, enthusiasm and advice, he offered me during the course of the thesis, and without him this work would not have been accomplished.

Many thanks go as well to Jean-Louis Pinçon, the principal investigator of the TARANIS space mission, for his advice, instructions, comments, help, and fruitful discussions we had during the course of this PhD.

I would like also to acknowledge all the members of the jury, Anne Bourdon, Jean-Louis Pinçon, Michel Tagger, Ningyu Liu, Sebastien Celestin, Serge Soula, and Thomas Farges, for their feedback, insightful comments, suggestions, instructions and continual friendly support.

I would like to especially thank my parents Adidi Iddir and Kaci Ihaddadene for their great endless support, love, encouragement they have provided me over the years, and for being proud of me and the work that I have achieved. Many thanks also go to my sisters and brother for all their kind of continual support and encouragement.

I want also to gratefully thank all my teachers and friends who greatly supported and encouraged me during the undergraduate and graduate period.

Finally, I thank all the colleagues of the LPC2E with who I worked and interacted with and for the good atmosphere and great moments of interaction we had together.

# Funding Agencies

I gratefully acknowledge the French Space Agency (CNES) and the French Region Centre-Val de Loire for funding my PhD in the framework of the TARANIS space mission and allowing me to carry out research at the LPC2E.

**“Believe in your capabilities and reach the top of success”**

# Dedication

to my mother and father,

Adidi Iddir and Kaci Ihaddadene

# Chapter 1

# Introduction

Sprites are large optical phenomena that last a few milliseconds and that are produced typically by positive cloud-to-ground (+CG) lightning between 40 and 90 km altitude [e.g., *Franz et al.*, 1990; *Winckler et al.*, 1993; *Pasko*, 2007; *Chen et al.*, 2008; *Stenbaek-Nielsen et al.*, 2013; *Pasko et al.*, 2013, and references therein]. Figure 1.1 shows an overview of the macroscopic process of sprite production by +CG lightning. Charges in the atmosphere above the thundercloud produce an opposite electric field to the one caused by the charge separation inside the thundercloud. A +CG very quickly transfer positive charges from the thundercloud to the ground resulting in a strong quasi-electrostatic electric field between the thunderclouds and in the ionosphere that lasts in a short period of time proportional to the local relaxation time $\tau = \frac{\epsilon_0}{q\mu_e n_e}$, where $\epsilon_0$, $q$, $\mu_e$, and $n_e$ are respectively, the permittivity of the free space, the electron charge, the electron mobility, and a local electron density. This local relaxation time varies between 40 and 100 km altitude from $\sim 10^{-2}$ to $\sim 10^{-6}$ s [e.g., *Hale*, 1994, see Figure 3]. Under the effect of the quasi-static electric field produced by +CG, electrons accelerate, collide with neutral air molecules, heat up the medium, and luminous flashes called sprites are then produced. To ignite sprites, the quasi-electrostatic electric field needs to be higher than the breakdown electric field ($E_k \sim 29$ kV/cm) [*Pasko et al.*, 1997, references therein], which is determined by the equality between the ionization and attachment processes [e.g., *Morrow and Lowke*, 1997]. This condition has been found to occur at altitudes around 70-80 km [*Wilson*, 1925]. Sprites belong to the wider family of transient luminous events

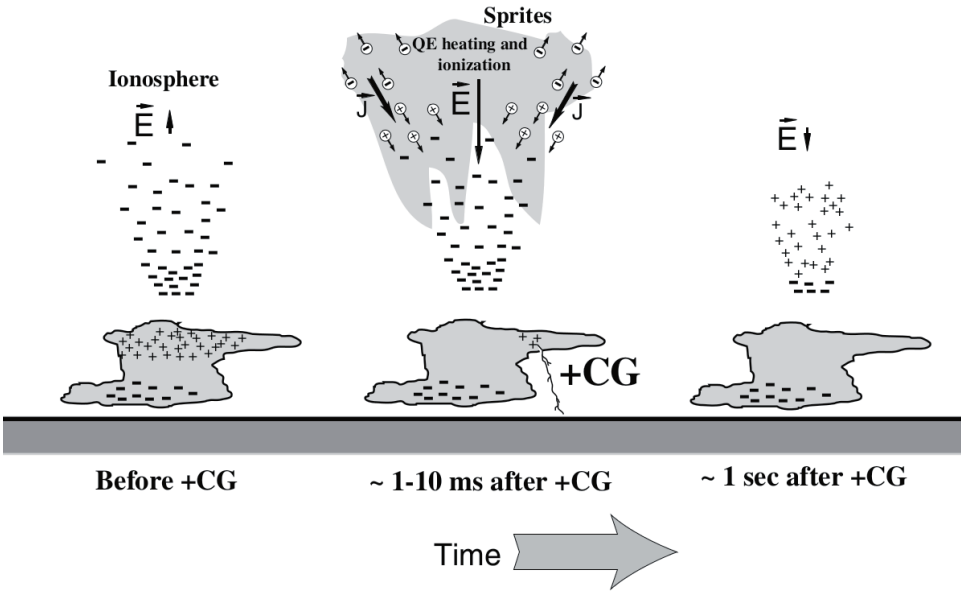


Figure 1.1 – Illustration of the process of the production of sprites by +CG lightning. Reproduced from [*Liu*, 2006].

(TLEs, e.g., blue jets, gigantic jets, elves, halos. See Figure 1.2) [e.g., *Pasko et al.*, 2012]. Studies have showed that sprites are composed of filamentary plasma structures (see Figure 1.3) called streamer discharges [e.g., *Pasko et al.*, 1998; *Gerken et al.*, 2000; *Stanley et al.*, 1999]. Some sprites can be highly complex and composed of many streamers [e.g., *Stanley et al.*, 1999; *Gerken et al.*, 2000; *Stenbaek-Nielsen et al.*, 2000], while some are composed of only a few filaments [e.g., *Wescott et al.*, 1998; *Adachi et al.*, 2004]. The different sprite morphologies are understood to be due to different upper atmospheric ambient conditions and the characteristics of the causative lightning discharge [e.g., *Hu et al.*, 2007; *Li et al.*, 2008; *Qin et al.*, 2013a,b, 2014, and references therein].

Under the effect of an external electric field, local seed electrons start to get accelerated. These electrons collide with the neutral air molecules and can produce secondary electrons and an exponential amplification of the process occurs and form an electron avalanche [*Raizer*, 1991]. The process of amplification continues and meanwhile an internal electric field starts to form within the avalanche due to the polarization of the former electron inhomogeneity under the effect of the external applied electric field. If the formed electric field is strong enough ($\sim E_k$), an avalanche-to-streamer transition may occur [*Qin*, 2013] and a streamer discharge is

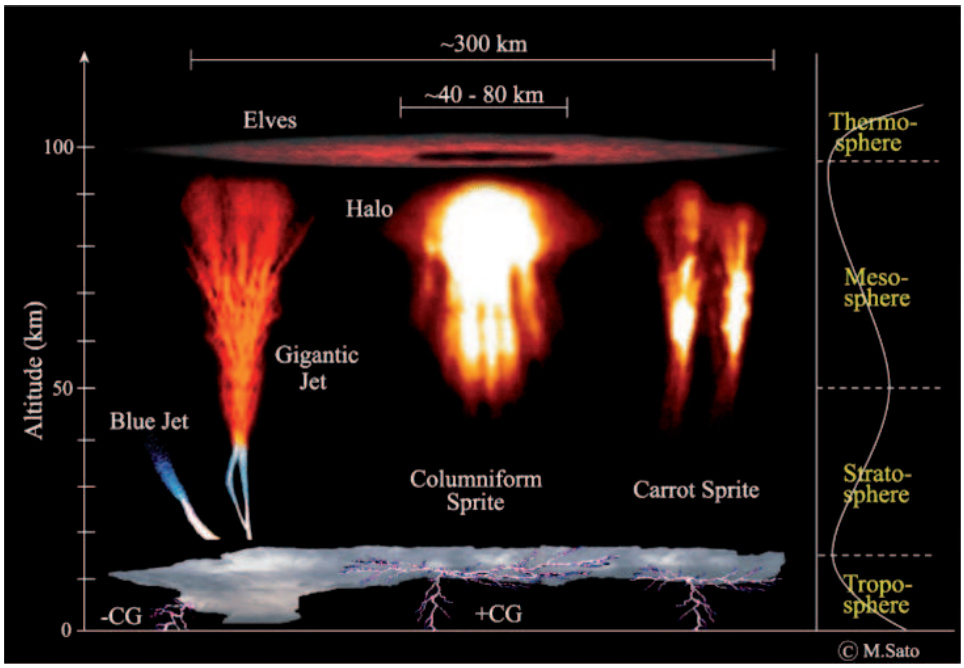


Figure 1.2 – Illustration of different types of TLEs with their spatial dimensions. Reproduced from [*Sato et al.*, 2011].

ignited. Streamer discharges are non-thermal plasma filaments, highly collisional, characterized with high electric fields at their heads (∼150 kV/cm in ground level air density) propagating as ionization waves with velocities up to $10^7$ m/s [*Li and Cummer*, 2009]. We distinguish two types of streamers, positive and negative characterized respectively, with dominant positive and negative charge densities in their heads. Streamers are involved in TLEs phenomena, lightning leaders, and at smaller scales such as in laboratory gas discharge experiments. The physics of streamers is very important to study in order to understand the microphysics of TLEs, energetic radiation from thunderstorms named TGFs (terrestrial gamma ray flashes), and lightning physics. Moreover, streamers are used in many technological and medical applications such as plasma assisted combustion, pollution control, ozone production, and treatment of skin diseases[e.g., *Kadowaki and Kitani*, 2010; *Babaeva and Kushner*, 2010; *Duten et al.*, 2011; *Starikovskaia*, 2014; *Lu et al.*, 2014, and references therein].

Streamer discharges usually consist of thermal electrons with energies up to few eVs in their channels and tips. Streamer discharges with higher electric fields in their heads ($E_h \simeq 260$ kV/cm in ground level air density) accelerate these thermal

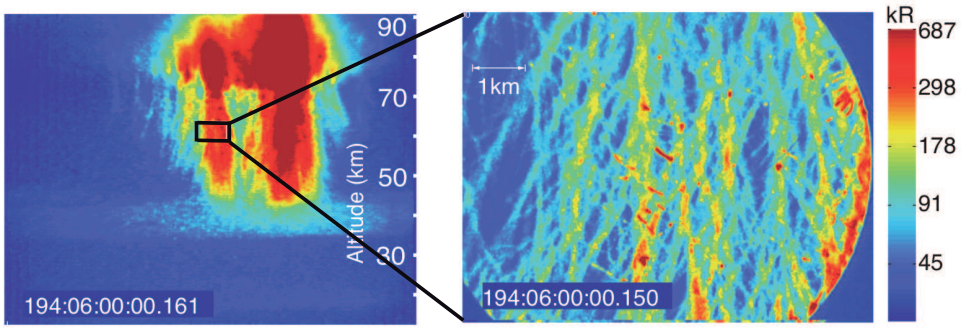


Figure 1.3 – A sprite and its streamer filamentary structure. Adapted from [*Gerken et al.*, 2000].

electrons to runaway regimes [e.g., *Moss et al.*, 2006; *Celestin and Pasko*, 2011]. These thermal electrons will gain energy per unit distance greater than the maximum of the friction force caused by collisions with a gas. In ground level air density, this friction force has a value ∼260 keV/cm for an electron with an energy 126 eV (see Figure 1.4). The runaway electrons are deflected by nuclei of air molecules and hence produce electromagnetic emissions (e.g., $\gamma$-rays, X-rays, if the electron energy energy is sufficient ), usually named the bremsstrahlung.

The production of energetic radiations by gas discharges was investigated a long time ago. Several gas discharge experiments conducted in the sixties and early seventies by Soviet scientists focused on observations of X-rays in their results [e.g., *Stankevich and Kalinin*, 1968; *Tarasova and Khudyakova*, 1970; *Kremnev and Kurbatov*, 1972, and references therein]. A large body of theoretical work was also conducted to understand the physics of gas discharges such as the energy deposited by the discharge, the processes of the acceleration of electrons to runaway regimes in strong electric fields, the production of X-rays, and the electron emission near the cathode [e.g., *Gurevich*, 1961; *Stankevich*, 1971; *Mesyats et al.*, 1972; *Babich and Stankevich*, 1973; *Bugaev et al.*, 1975; *Litvinov et al.*, 1983, and references therein].

Despite the efforts mentioned above and the actual advance in numerical modeling and experimental techniques, the processes responsible for the production of high-energy radiation in laboratory discharges and thunderstorms are not fully understood yet. X-ray bursts have been detected from the ground during the descent of natural negative lightning stepped leader [*Moore et al.*, 2001] and rocket-triggered lightning flashes [*Dwyer et al.*, 2003]. Recently, observational studies have been ded-

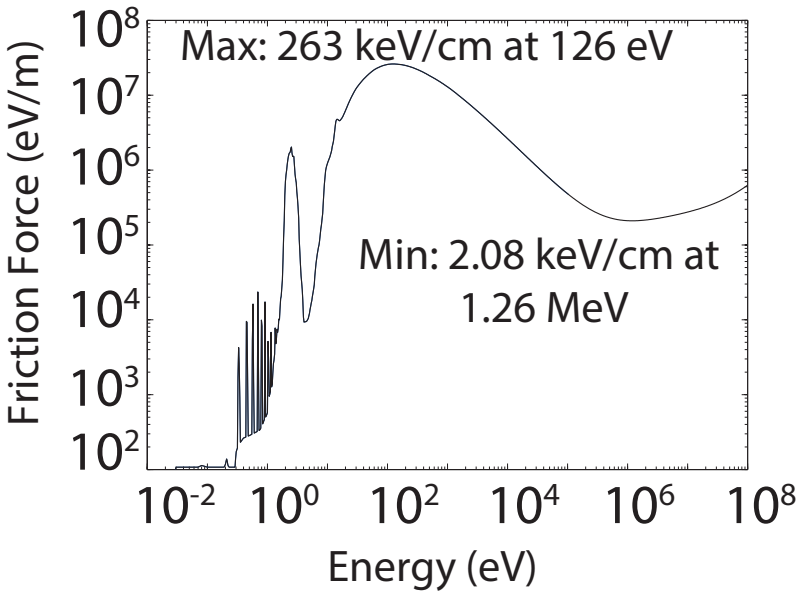


Figure 1.4 – Friction force at ground level air versus electron energy.

icated to understand these emissions in lightning [e.g., *Howard et al.*, 2008; *Saleh et al.*, 2009; *Dwyer et al.*, 2011; *Schaal et al.*, 2014] and laboratory experiments have confirmed that meter-scale atmospheric pressure discharges produce X-rays [e.g., *Dwyer et al.*, 2005; *Rahman et al.*, 2008; *Nguyen et al.*, 2008, 2010; *March and Montanyà*, 2011; *Kochkin et al.*, 2012, 2015b,a].

The emission of X-rays by lightning discharges is believed to be caused by the production of thermal runaway electrons [*Dwyer*, 2004]. Indeed, *Moss et al.* [2006] have suggested that the strong electric fields that are produced in streamer heads could be responsible for thermal runaway electron production and *Celestin and Pasko* [2011] have shown how large fluxes of runaway electrons could be produced by streamer discharges propagating under strong electric fields such as those present at the leader tip. Recently, *Babich et al.* [2015] have suggested that thermal runaway electrons could be produced by streamer discharges guided by precursor streamer channels. Moreover, it is interesting to note that based on the theory of production of thermal runaway electrons by streamers at the leader tip, *Xu et al.* [2014] have shown that negative leaders forming potential drops of approximately 5 MV in their tip region would produce X-ray spectra similar to observational results of *Schaal et al.* [2012] in terms of general shape and spectral hardness.

Encounters between streamers of opposite polarities are believed to be very common in nature and laboratory experiments. In particular, during the formation of a new leader step, the negative streamer zone around the tip of a negative leader and the positive streamers initiated from the positive part of a bidirectional space leader strongly interact and numerous head-on encounters are expected. In laboratory experiments, when streamers are approaching a sharp electrode, streamer discharges with the opposite polarity are initiated from this electrode and collide with the approaching streamers. *Cooray et al.* [2009] suggested that head-on collisions between negative and positive streamers could produce extremely strong electric fields that would lead to the production of thermal runaway electrons and corresponding X-rays. On the basis of experimental evidence, *Kochkin et al.* [2012] recently concluded that X-ray bursts over a timescale shorter than a few nanoseconds were indeed produced by collisions between positive and negative streamers, but X-ray detections could not be related to specific streamer collisions (see also [*Kochkin et al.*, 2015b, Section 3.5.2]).

In the context of sprites, encounters between upward negative streamers and downward positive streamers may occur frequently and high-energy electrons and corresponding X-rays might be produced, but it has not been observed in sprite yet and it is not clear if satellite-based detectors could have made the corresponding observations. Additionally, encounters between negative and positive streamers increase the local electron density and produce local visible optical emission patches [*Ihaddadene and Celestin*, 2015] that might be associated to the sprite beads [e.g., *Cummer et al.*, 2006; *Stenbaek-Nielsen and McHarg*, 2008; *Luque and Gordillo-Vasquesz*, 2011; *Ihaddadene and Celestin*, 2015]. Interestingly, during their laboratory discharge experiments, *Kochkin et al.* [2014], and *Kochkin et al.* [2015b], have mentioned observations of structures named pilot systems, composed of dots and streamer branches and produce backward positive streamers, which collide with negative ones. They suggested that this mechanism could produce X-rays. It is likely that such collisions between negative and positive streamers happen in sprites. Sprite beads themselves may be associated with upward streamers (see dots designated by arrows in Figure 1.6 (1)-(2)).

The notion of the energy deposited by a streamer is an important quantity that

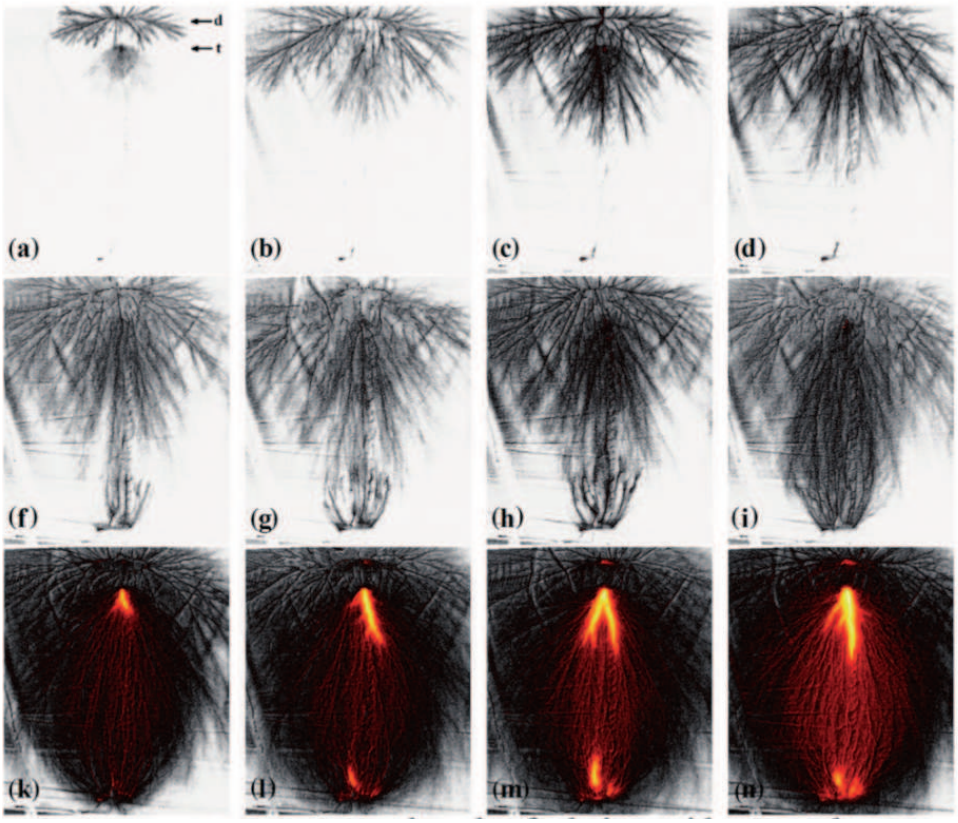


Figure 1.5 – Laboratory encounter between upward positive and downward negative propagating streamers. Reproduced from [*Kochkin et al.*, 2012].

needs to be quantified to better understand the local effect of either laboratory or sprite streamers. The energy deposited by a small scale laboratory streamer is typically of a few microjoules [e.g., *Pai et al.*, 2010] and the energy deposited by streamers in a sprite event has been quantified using optical emissions and estimated to be typically 22 MJ by *Kuo et al.* [e.g., 2008].

One of the methods used to explore the physical properties of sprites is the spectroscopic diagnostic of their optical emissions, specifically in the following bands systems of $N_2$: the Lyman-Birge-Hopfield (LBH) ($a^1\Pi_g \rightarrow X^1\Sigma_g^+$) [e.g., *Liu and Pasko*, 2005; *Liu et al.*, 2006, 2009a; *Gordillo-Vázquez et al.*, 2011], the first positive $1PN_2$ ($B^3\Pi_g \rightarrow A^3\Sigma_u^+$) [e.g., *Mende et al.*, 1995; *Hampton et al.*, 1996; *Green et al.*, 1996; *Morrill et al.*, 1998; *Milikh et al.*, 1998; *Bucsela et al.*, 2003; *Kanmae et al.*, 2007; *Siefring et al.*, 2010; *Gordillo-Vázquez*, 2010; *Gordillo-Vázquez et al.*, 2011, 2012], the second positive $2PN_2$ ($C^3\Pi_u \rightarrow B^3\Pi_g$) [e.g., *Armstrong et al.*, 1998; *Morrill et al.*, 1998; *Milikh et al.*, 1998; *Suszcynsky et al.*, 1998; *Heavner et al.*, 2010; *Gordillo-Vázquez*, 2010; *Gordillo-Vázquez et al.*, 2011, 2012], as well as the first negative bands systems of $N_2^+$ ($1NN_2^+$) ($B^2\Sigma_u^+ \rightarrow X^2\Sigma_g^+$) [e.g., *Armstrong et al.*, 1998; *Suszcynsky et al.*, 1998; *Kanmae et al.*, 2010a]. Several works have been realized to determine the electric fields involved in sprite streamers based on their produced optical emissions [e.g., *Morrill et al.*, 2002; *Kuo et al.*, 2005; *Adachi et al.*, 2006; *Kanmae et al.*, 2010b] and some have shown an acceptable agreement with simulations [*Liu et al.*, 2006]. However, theoretical studies have also shown the existence of correction factors to take into account to determine an accurate value of the peak electric field in streamer heads. The correction factors are due to both a spatial shift between the maximum in the electric field at the head of the streamer and the maximum in the production of excited species and the fact that most photons are produced some distance away from the filament symmetry axis [*Celestin and Pasko*, 2010; *Bonaventura et al.*, 2011].

The experiment LSO (Lightning and Sprite Observations) developed by the French Atomic Energy Commission (CEA) with the participation of the French Space Agency (CNES) [*Blanc et al.*, 2004], the Japanese Aerospace Exploration Agency (JAXA) mission GLIMS (Global Lightning and sprIte MeasurementS) [*Sato et al.*, 2015], and the future European Space Agency (ESA) mission ASIM (Atmosphere-

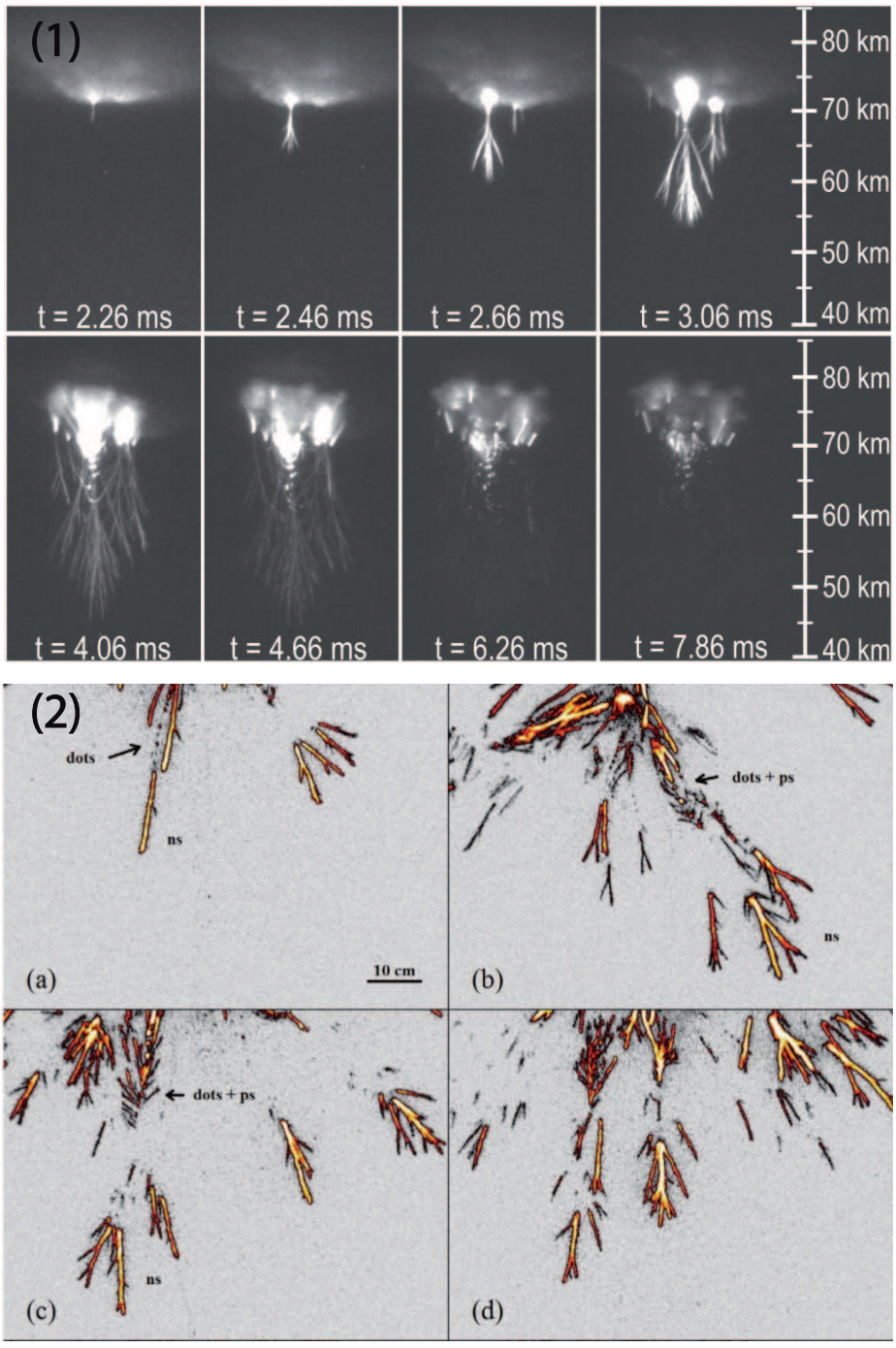


Figure 1.6 – (1) Illustration of sprite beads (luminous dots designated by arrows) during a sprite formation process. (2) Pilot system structures (dots designated by arrows) produced in laboratory discharge experiment. Adapted from [*Cummer et al.*, 2006; *Kochkin et al.*, 2012], respectively.

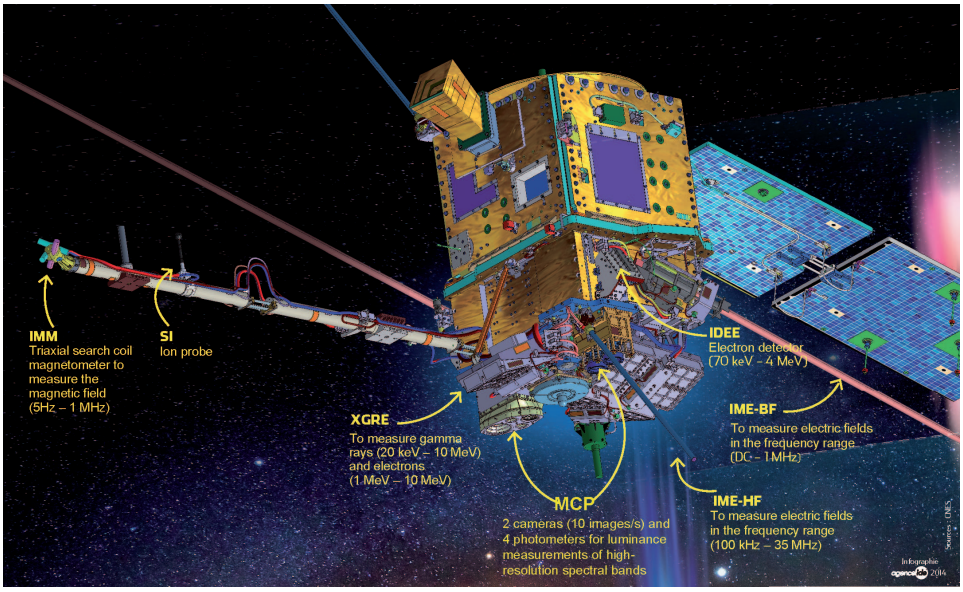


Figure 1.7 – TARANIS satellite mission. Credit: CNES.

Space Interactions Monitor) [*Neubert*, 2009] are dedicated to the observation of TLEs from the International Space Station (ISS). The Lomonosov Moscow State University (MSU) satellite Universitetsky-Tatiana-2 observed TLEs from a sun-synchronous orbit at 820-850 km altitude [*Garipov et al.*, 2013]. The future satellite mission TARANIS (Tool for the Analysis of RAdiation from lightNIng and Sprites), funded by CNES, will observe TLEs from a sun-synchronous orbit at an altitude of ∼700 km [*Lefeuvre et al.*, 2008]. TARANIS is dedicated to the study of impulsive couplings in the atmosphere-ionosphere-magnetosphere system. Two instruments that are relevant to the present study will be carried on board TARANIS to detect optical emissions from TLEs and measure energetic electrons and the corresponding emissions: Micro-Cameras and Photometers (MCP) and X-rays, Gamma-rays, and Relativistic Electrons (XGRE). The MCP instrument is composed of two micro-cameras that will observe TLEs and four photometers: PH1 (160 to 260 nm), mostly covered by the LBH bands systems, PH2 (337±5 nm), is centered on the most intense band of $2PN_2$, PH3 (762±5 nm), is centered on the most intense band of $1PN_2$, and PH4 (600 to 900 nm), which will be dedicated to lightning flash measurements. XGRE will measure energetic radiations with energies between 20 keV and 10 MeV and electrons with energies between 1 MeV and 10 MeV. A whole view of the satellite and the payloads is shown in Figure 1.7.

All the mentioned space missions (LSO, GLIMS, Tatiana-2, ASIM, and TARANIS) have adopted strategies based on nadir observation of TLEs. Observation from a nadir-viewing geometry is indeed especially interesting as it reduces the distance between the observation point and the event, and hence minimizes atmospheric absorption and maximizes the chance of observing TLEs and their associated phenomena, such as electromagnetic radiation or possible high-energy emissions. However, in this observation geometry, the vertical dimension and hence the altitude of downward propagating streamers is poorly resolved, and so are the speeds of sprite substructures.

In this dissertation, we present an investigation of streamer properties using numerical tools in order to address the following questions:

1. Is the process of head-on collision between negative and positive streamers a likely source of energetic electrons and radiation such as X-rays?
2. Could the process of head-on collision between negative and positive streamers be one of the mechanisms associated with sprite beads?
3. How can we determine the altitude, electric field and velocity of sprite streamers using optical emissions in case of nadir-viewing geometry ?
4. Is a single streamer discharge, under specific conditions, a source of energetic radiation?
5. What is the energy deposited by the streamer discharge at small scales (laboratory) and large scales (sprites)?

The scientific work of this dissertation will help advance the understanding of the microphysics of streamer discharges involved in laboratory experiments and TLEs, particularly in view of future space missions, such as TARANIS (CNES) and ASIM (ESA) that are devoted to the study of TLEs and energetic radiation from thunderstorms.

In Chapter 2, we present the streamer plasma fluid model that have been developed during the course of this PhD, in Chapter 3, we investigate the head-on collision process between negative and positive streamer discharges, in Chapter 4, we present the spectrophotometric method that have been developed to estimate the altitude of sprite streamers, in Chapter 5, by using the developed streamer plasma

fluid model, we reproduce experimental results of a laboratory discharge that produces X-rays and present some points related to the energetics of streamers, and finally in Chapter 6, we summarize the main conclusions and suggestions for future work.

# Chapter 2

# Streamer model formulation

**Abstract in French**

Dans ce chapitre, on présente le modèle numérique de simulation des plasmas filamentaires de type streamer dans l'air, dans différentes configurations, et à différentes altitudes developpé pendant la thèse. Ce modèle est couplé avec un modèle simplifié de production d'espèces excitées et leurs émissions optiques associées. Plus précisement, on présente les équations de dérive-diffusion des électrons et des ions, le calcul du champ électrique via l'équation de Poisson, les processus physiques impliqués et leur résolution. On presente les problémes numériques rencontrés durant la construction du modèle et les techniques utilisées pour les résoudre. Des fronts très raides apparaissent et la solution numérique nécessite ainsi un traitement particulier. Nous utilisons la technique Flux Corrected Transport (FCT) introduite pour résoudre des problèmes de chocs en physique des fluides. Nous détaillons l'utilisation de cette technique et son application aux simulations de types streamers.

## 2.1 Introduction

In this section, we present the full plasma streamer fluid model that has been developed during the PhD. The model simulates streamer discharges in air at different altitudes. The model simulates different configurations such as parallel and point-to-plane electrodes, which is practical to study different physical situations, e.g., laboratory streamer discharges, sprite streamers, double headed streamers, and

streamer head-on collisions, under various external electric fields. The model itself is coupled with an optical emission model that quantifies the excited species produced by the streamer and their associated optical emissions. In Section 2.2, we explain the physical processes involved in the model, and in Section 2.3, we present the numerical approach.

## 2.2 Streamers equations

The streamer discharge model is based on an ensemble of partial differential equations that describe the motion of electrons, and positive and negative ions (charged species) under the effect of an electric field in a highly collisional environment. The streamer discharge is a non-thermal plasma, i.e, the temperature of electrons is different from that of the ions and molecules. These equations are the so-called drift-diffusion equations for charged species and they are coupled with Poisson's equation as follows:

$$\frac{\partial n_{\mathrm{e}}}{\partial t} + \nabla . n_{\mathrm{e}} \vec{v}_{\mathrm{e}} - D_{\mathrm{e}} \nabla^2 n_{\mathrm{e}} = S_{\mathrm{ph}} + S_{\mathrm{e}}^{+} - S_{\mathrm{e}}^{-} \tag{2.1}$$

$$\frac{\partial n_{\mathrm{p}}}{\partial t} = S_{\mathrm{ph}} + S_{\mathrm{p}}^{+} \tag{2.2}$$

$$\frac{\partial n_{\mathrm{n}}}{\partial t} = S_{\mathrm{n}}^{+} \tag{2.3}$$

$$\nabla^2 \phi = -\frac{q}{\varepsilon_0}(n_{\mathrm{p}} - n_{\mathrm{n}} - n_{\mathrm{e}}) \tag{2.4}$$

where subscripts 'e','p', and 'n' refer to electrons, positive and negative ions, respectively, $n_{\mathrm{i=e,p,n}}$ is the number density of species i, $v_{\mathrm{e}}$ is the electron drift velocity, and $D_{\mathrm{e}}$, $q$, $\varepsilon_0$, and $\phi$ are the electron diffusion coefficient, the absolute value of the electron charge, the permittivity of free space, and the electric potential, respectively. The term $S$ is the source term related to the production ($S^{+}$) and loss ($S^{-}$) of charged species.

The equation (2.1) describes the dynamics (evolution in space and time) of electrons supposed to be in equilibrium under a given electric field. The drift-diffusion approach takes into account the drift of the electrons under the effect of the electric field and their physical diffusion, which are described respectively by the terms:

$\nabla.n_e\vec{v}_e$ and $D_e\nabla^2 n_e$.

The equations (2.2) and (2.3) describe the dynamics of the ions involved in the streamer discharge (e.g., $N_2^+$, $O_2^+$, $O^-$, $O_2^-$). In the present model, we consider ions motionless over short time scales because they are heavier than electrons, and thus we neglect the ions drift velocity and the ions diffusion.

The above equations (2.1)-(2.3) are derived from the Boltzmann's equation. Poisson's equation is critical in the system of the equations (2.1)-(2.3) because of the dependence of the source and transport coefficients (e.g., ionization, attachment, mobility, etc.) on the electric field. In the present model, we employ the local electric field approximation, and thus the transport coefficients and the local energy of electrons are explicit functions of the electric field [e.g., *Morrow and Lowke*, 1997]. Hence, in our model, determining the energy or the electric field is equivalent, and the link between these two quantities is given by Einstein relation: $k_B T_e = \frac{qD_e(E)}{\mu_e(E)}$, where $k_B$ is the Boltzmann constant, $T_e$ is the electron temperature, $\mu_e$ is the mobility of electrons, and $E$ is the local electric field. Each transport coefficient and source term is a quantity defined for a large ensemble of particles to describe the motion of charged species. In the local field approximation, we make the assumption that electrons are in equilibrium in an homogeneous local electric field and transport coefficients are derived from the electron energy distribution function (EEDF) $f(\epsilon)$ that depends only on the local electric field. Using the EEDF, source terms $S_i$ are calculated as follows:

$$S_i = \int_0^\infty f(\epsilon)\sigma_i(\epsilon)v(\epsilon)d\epsilon \tag{2.5}$$

where $\sigma_i$ is the cross section corresponding to a given source process, $v$ is the velocity of an electron, and $\epsilon$ is the electron energy ($\epsilon = \frac{1}{2}m_e v^2$, where $m_e$ is the electron mass).

### 2.2.1 Ionization and attachment processes

The principal processes behind the production and loss of electrons in the streamer discharge are ionization and attachment and both of these processes depend on the local electric field.

Secondary electrons are produced through collisions between primary electrons accelerated under the effect of the electric field and neutral molecules (e.g., $N_2$ and

$O_2$). The ionization process can be described as:

$$e + \mathrm{A} \rightarrow 2\mathrm{e} + \mathrm{A}^+$$

The attachment process consists in the attachment of an electron with a neutral molecule and the production of a negative ion. We consider that mainly two attachment processes are dominant in the present study: two-body attachment, also named dissociative attachment, and three body attachment. They can be described as:

$$e + \mathrm{O}_2 \rightarrow \mathrm{O}^- + \mathrm{O}$$
$$e + \mathrm{O}_2 + \mathrm{A} \rightarrow \mathrm{O}_2^- + \mathrm{A}$$

The three above processes are included in the set of streamer model equations (2.1)-(2.4) through the terms:

$S_\mathrm{e}^+ = \nu_i n_\mathrm{e}$ and $S_\mathrm{e}^- = (\nu_{2a} + \nu_{3a}) n_\mathrm{e}$, for the ionization and attachment, respectively, where $\nu_i$, $\nu_{2a}$, and $\nu_{3a}$ are the ionization frequency, the two-body attachment frequency, and the three-body attachment frequency.

### 2.2.2 Photoionization process

In addition to local processes of production and loss of electrons (e.g., ionization), we take into account the photoionization process, which is a non-local process that contributes to the generation of electrons far away from the photon source. According to [e.g., *Liu*, 2006], the process can be described as:

$$\mathrm{e} + \mathrm{N}_2 \rightarrow \mathrm{e} + \mathrm{N}_2^\star$$
$$\mathrm{N}_2^\star \rightarrow \mathrm{N}_2 + \mathrm{h}\nu$$
$$h\nu + \mathrm{O}_2 \rightarrow \mathrm{e} + \mathrm{O}_2^+$$

Through the collision of electrons with $\mathrm{N}_2$, the latter is excited from the ground state ($X^1\Sigma_g^+$) to specific high energy states (e.g., $b^1\Pi_u$, $b_1^{'}\Sigma_u^+$ or $c_4^{'1}\Sigma_u^+$), which after de-excitation emit a photon in the wavelength range $980 < \lambda < 1025$ $\mathring{A}$ responsible for the ionization of $\mathrm{O}_2$ [e.g., *Liu*, 2006].

In the set of the streamer model equations, the photoionization process is described by the term $S_{\rm ph}$ and it is calculated as follows [e.g., *Liu*, 2006]:

$$S_{\rm ph} = \iiint \frac{1}{4\pi R^2} \frac{p_q}{p+p_q} \xi \frac{\nu_*}{\nu_i} S_i \frac{\exp(-\chi_{min} p_{o_2} R) - \exp(-\chi_{max} p_{o_2} R)}{R \ \ln\left(\frac{\chi_{max}}{\chi_{min}}\right)} dV \qquad (2.6)$$

where $S_i = \nu_i n_{\rm e}$ is the photoionization source. $p$, $p_q$, and $p_{O_2}$ are the gas pressure, the quenching pressure, and the oxygen partial pressure, respectively. The quantities $\chi_{min}$ and $\chi_{max}$ are the minimum and maximum absorption coefficients of $O_2$. The quantities $\xi$ and $\nu_*$ are the average photoionization efficiency and excitation frequency of $N_2$ in the wavelength interval $980< \lambda <1025$ $\mathring{A}$. $R$ is the distance between the source of photons and the location of photoelectron production. From Figure 2.1 the distance $R$ is calculated in cylindrical coordinates as follows:

$R^2 = L^2 + (z-z^{'})^2 = h^2 + (r-l)^2 + (z-z^{'})^2 = (r^{'}\sin\theta^{'})^2 + (r - r^{'}\cos\theta^{'})^2 + (z-z^{'})^2 = r^2 + (r^{'})^2 - 2rr^{'}\cos\theta^{'} + (z-z^{'})^2$

where $(r,z)$ and $(r^{'},z^{'})$ are the coordinates of the source and the photoelectron production points.

In this work, we use the integral approach of the photoionization process [*Zheleznyak et al.*, 1982; *Liu and Pasko*, 2004], which is based on equation (2.6).

### 2.2.3 Effect of space charge

In the streamer head region, a high density of space charge is present. To take into account the effect of the space charge at the limits of the simulation domain while a streamer propagates, we need to define boundary conditions for Poisson's equation. In this case, we use the integral form of the electric potential to compute respectively the potential at the boundaries which defines open boundary conditions for Poisson's equations (see Section 2.3.2).

$$\phi = \frac{1}{4\pi\epsilon_0} \iiint \frac{q(n_{\rm p} - n_{\rm n} - n_{\rm e})}{R} dV \qquad (2.7)$$

where $\phi$ is the electric potential, $q(n_{\rm p} - n_{\rm n} - n_{\rm e})$ is the density of the space charge, and $R$ is the distance between the density of the space charge and the point located at the boundaries of the simulation domain.

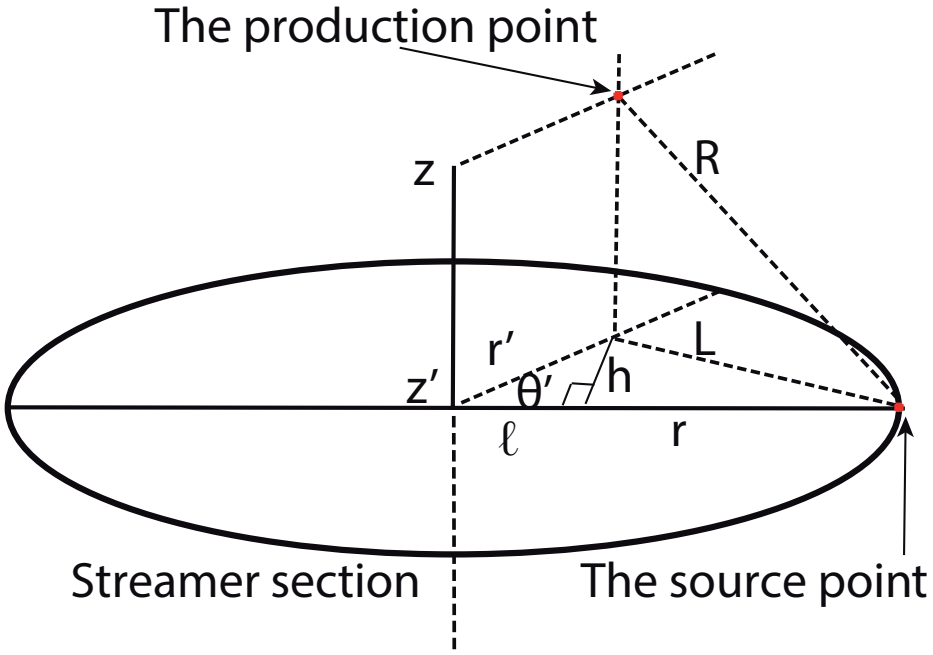


Figure 2.1 – Geometrical view of the distance between a source point $(z^{'}, r^{'})$ located on a streamer section and the production point $(z, r)$ located on another streamer section in case of the photoionization process.

### 2.2.4 Optical emission model

The streamer optical emission model is based on the following equations [e.g., *Liu*, 2006]:

$$\frac{\partial n_k}{\partial t} = -\frac{n_k}{\tau_k} + \nu_k n_e + \sum_m n_m A_m \tag{2.8}$$

$$I_k = 10^{-6} \int_L A_k n_k dl \tag{2.9}$$

where the quantities $n_k$ and $\nu_k$ are respectively the density and the excitation frequency of the excited species $k$. As the streamer model is based on the local electric field approximation, $\nu_k$ depends on the local electric field or equivalently on the electron energy. The quantities $\tau_k = [A_k + \alpha_1 N_{N_2} + \alpha_2 N_{O_2}]^{-1}$ and $A_k$ are the characteristic life time and Einstein's coefficient of the excited species $k$. The quantity $\frac{1}{A_k}$ defines the radiative de-excitation time and the term $\alpha_1 N_{N_2} + \alpha_2 N_{O_2}$ takes into account the collisional de-excitation process of the excited species with

the neutral molecules (quenching process), where $N_{N_2}$ and $N_{O_2}$ are the densities of $N_2$ and $O_2$ molecules.

The equation (2.8) quantifies the evolution of the densities of excited species in space and time generated in the streamer discharge (e.g., $N_2(B^3\Pi_g)$, $N_2(C^3\Pi_u)$, $N_2(a^1\Pi_g)$, and $N_2^+(B^2\Sigma_u^+)$) taking into account the cascading of excited species from higher energy levels $m$ to the level $k$ defined by the term: $\sum_m n_m A_m$ . In this work, we only take into account the cascading term from $N_2(C^3\Pi_u)$ to $N_2(B^3\Pi_g)$. The equation (2.9) quantifies the flux of photons $I_k$ in Rayleighs ($s^{-1}cm^{-2}$) produced along the line of sight after de-excitation of $N_2$ and $N_2^+$ levels.

From the densities of excited species of $N_2(B^3\Pi_g)$, $N_2(C^3\Pi_u)$, $N_2(a^1\Pi_g)$ and $N_2^+(B^2\Sigma_u^+)$ and equation (2.9), we evaluate respectively the associated optical emissions of the first positive bands system of $N_2$ ($1PN_2$) ($B^3\Pi_g \rightarrow A^3\Sigma_u^+$), the second positive bands system of $N_2$ ($2PN_2$) ($C^3\Pi_u \rightarrow B^3\Pi_g$), the Lyman-Birge-Hopfield bands system (LBH) ($a^1\Pi_g \rightarrow X^1\Sigma_g^+$) and the first negative bands system of $N_2^+$ ($1NN_2^+$) ($B^2\Sigma_u^+ \rightarrow X^2\Sigma_g^+$), respectively. As reported in the study by *Liu and Pasko* [2005], we consider that $N_2(a^1\Pi_g)$ is quenched by $N_2$ and $O_2$ with rate coefficients $\alpha_1 = 10^{-11}$ $cm^3/s$ and $\alpha_2 = 10^{-10}$ $cm^3/s$, respectively. As used by *Xu et al.* [2015], the quenching of $N_2(B^3\Pi_g)$ and $N_2(C^3\Pi_u)$ is considered to occur through collisions with $N_2$ and $O_2$ with rate coefficients $\alpha_1 = 10^{-11}$ $cm^3/s$ [*Kossyi et al.*, 1992] and $\alpha_2 = 3 \times 10^{-10}$ $cm^3/s$ [*Vallance Jones*, 1974, p. 119], respectively. $N_2^+(B^2\Sigma_u^+)$ is quenched by $N_2$ with a rate coefficient $\alpha_1 = 4.53 \times 10^{-10}$ $cm^3/s$ and by $O_2$ with a rate coefficient $\alpha_2 = 7.36 \times 10^{-10} cm^3/s$ [e.g., *Mitchell*, 1970; *Pancheshnyi et al.*, 1998; *Kuo et al.*, 2005]. The corresponding $A_k$ [e.g., *Liu*, 2006] and quenching coefficients taken into account for $N_2(a^1\Pi_g)$, $N_2(B^3\Pi_g)$, $N_2(C^3\Pi_u)$, and $N_2^+(B^2\Sigma_u^+)$ are shown in Table 1. In the present model, we consider a simple atmospheric composition of 80 % of nitrogen and 20% oxygen: $N_{N_2} = 0.8 \times N$ and $N_{O_2} = 0.2 \times N$ where $N = 2.688 \times 10^{25} m^{-3}$ is the density of the air at the ground level. The local air density at higher altitudes is taken based on the US Standard Atmosphere [*COESA*, 1976].

Table 2.1 – Einstein coefficient $A_k$ ($s^{-1}$), quenching coefficients $\alpha_{1,2}$ ($cm^3/s$), lifetime $\tau_k$ (s) at ground level air of different excited states of $N_2$ molecule, and quenching altitudes $h_Q$ (km).

| | $N_2(a^1\Pi_g)$ | $N_2(B^3\Pi_g)$ | $N_2(C^3\Pi_u)$ | $N_2^+(B^2\Sigma_u^+)$ |
|---|---|---|---|---|
| $A_k$ | $1.8 \times 10^4$ | $1.7 \times 10^5$ | $2 \times 10^7$ | $1.4 \times 10^7$ $s^{-1}$ |
| $\alpha_1$ | $10^{-11}$ | $10^{-11}$ | $10^{-11}$ | $4.53 \times 10^{-10}$ |
| $\alpha_2$ | $10^{-10}$ | $3 \times 10^{-10}$ | $3 \times 10^{-10}$ | $7.36 \times 10^{-10}$ |
| $\tau_k$ | $1.33 \times 10^{-9}$ | $5.47 \times 10^{-10}$ | $5.41 \times 10^{-10}$ | $7.29 \times 10^{-11}$ |
| $h_Q$ | 77 | 67 | 31 | 48 |

### 2.2.5 Similarity laws

The scaling laws, or similarity laws allow to understand the behavior of streamer discharges under different pressures. *Pasko* [2006] and *Qin and Pasko* [2015] give a comprehensive review of useful similarity relationships for gas discharges:

$$\text{Length } L = L_0 \frac{N_0}{N}$$

$$\text{Time } \tau = \tau_0 \frac{N_0}{N}$$

$$\text{The velocity } v = \frac{L}{\tau} = constant$$

$$\text{Electric field } E = E_0 \frac{N}{N_0}$$

$$\text{Mobility } \mu = \mu_0 \frac{N_0}{N}$$

$$\text{Diffusion coefficient } D = D_0 \frac{N_0}{N}$$

$$\text{Electron density } n = n_0 \frac{N^2}{N_0^2}$$

$$\text{Electric charge } Q = Q_0 \frac{N_0}{N}$$

$$\text{Ionization frequency } \nu = \frac{1}{\tau} = \nu_0 \frac{N}{N_0}$$

$$\text{Conductivity } \sigma = en\mu = \sigma_0 \frac{N}{N_0}$$

$$\text{Current density } J = env = J_0 \frac{N^2}{N_0^2}$$

$$\text{Electric current } I = JL^2 = constant$$

where subscripts "$0''$, represent quantities at ground level and the absence of subscripts represent quantities at given altitude, respectively. Above ~25 km sprite streamers are understood to be nearly perfectly similar (i.e., the scaling laws hold). Below this altitude *Liu and Pasko* [2004] have shown that similarity is broken by the quenching of excited states responsible for the photoionization (see Section 3.1.4). However, the similarity laws listed above are a good order of magnitude approximation below 25 km. To simulate sprite streamers at different altitudes, we scale the spatial resolution of the simulation domain $\Delta z$ and $\Delta r$, the external applied

electric field $E_0$, and the oxygen pressure $p_{O_2}$ (see equation (2.6)).

## 2.3 Numerical approach

In this section, we explain how we solve the streamer model equations, we expose the different numerical issues that we have encountered and the numerical techniques we have used to solve them. We start by solving Poisson's equation, the photoionization integral, the drift-diffusion equations of electrons and ions, and finally the optical emission model equations.

### 2.3.1 Discretized domain of simulation

Before solving the streamer model equations, a discretized domain of simulation in cylindrical coordinates must be defined. Since we assume a cylindrical symmetry, we set all variables such that $\frac{\partial}{\partial\theta} = 0$. We first define $N_z$ ($z$-axis: $i = 1, N_z$) and $N_r$ ($r$-axis: $j = 1, N_r$) the maximum number of grid points along $z$- and $r$- axes, respectively. We use a Cartesian grid which implies $\Delta z{=}\Delta r$. We also define the interfaces between grid points (see dashed red lines on Figure 2.2) named by $z_{m_{i+\frac{1}{2}}}$ and $r_{m_{j+\frac{1}{2}}}$. For the precision, $r_{j=1} = 0$, $z_{i=1} = 0$, $r_{m_{j=1}} = \frac{\Delta r}{2}$ and $z_{m_{i=1}} = \frac{\Delta z}{2}$. One defines the surfaces ($S_{i+\frac{1}{2}}$, $S_{j+\frac{1}{2}}$) and volumes ($V_{j+\frac{1}{2}}$).

In the vicinity of the axis of symmetry ($j = 1$):

$$S_{j+\frac{1}{2}} = 2\pi\Delta z(r_{m_{j=1}}) = 2\pi\Delta z(\tfrac{\Delta r}{2})$$
$$S_{i+\frac{1}{2}} = \pi(r_{m_{j=1}})^2 = \pi(\tfrac{\Delta r}{2})^2$$
$$V_{j+\frac{1}{2}} = \pi(r_{m_{j=1}})^2\Delta z = \pi(\tfrac{\Delta r}{2})^2\Delta z$$

Away from the axis of symmetry ($j \neq 1$):

$$S_{j+\frac{1}{2}} = 2\pi\Delta z(r_{m_j}) = 2\pi\Delta z(r_j + \tfrac{\Delta r}{2})$$
$$S_{i+\frac{1}{2}} = \pi((r_{m_j})^2 - (r_{m_{j-1}})^2) = \pi((r_j + \tfrac{\Delta r}{2})^2 - (r_{j-1} + \tfrac{\Delta r}{2})^2)$$
$$V_{j+\frac{1}{2}} = \pi((r_{m_j})^2 - (r_{m_{j-1}})^2)\Delta z = \pi((r_j + \tfrac{\Delta r}{2})^2 - (r_{j-1} + \tfrac{\Delta r}{2})^2)\Delta z$$

The notation $i + \frac{1}{2}$ and $j + \frac{1}{2}$ refer to the interfaces (red dashed lines on a Figure 2.2). Note that, for ($i = 1, j = 1, N_r$) and ($i = N_z, j = 1, N_r$), the volume of the grid cells is half that of the volume of the cells ($i_{=1} + 1, j = 1, N_r$) and ($i_{=N_z} - 1, j = 1, N_r$). Interesting cases to test the implementation of boundary

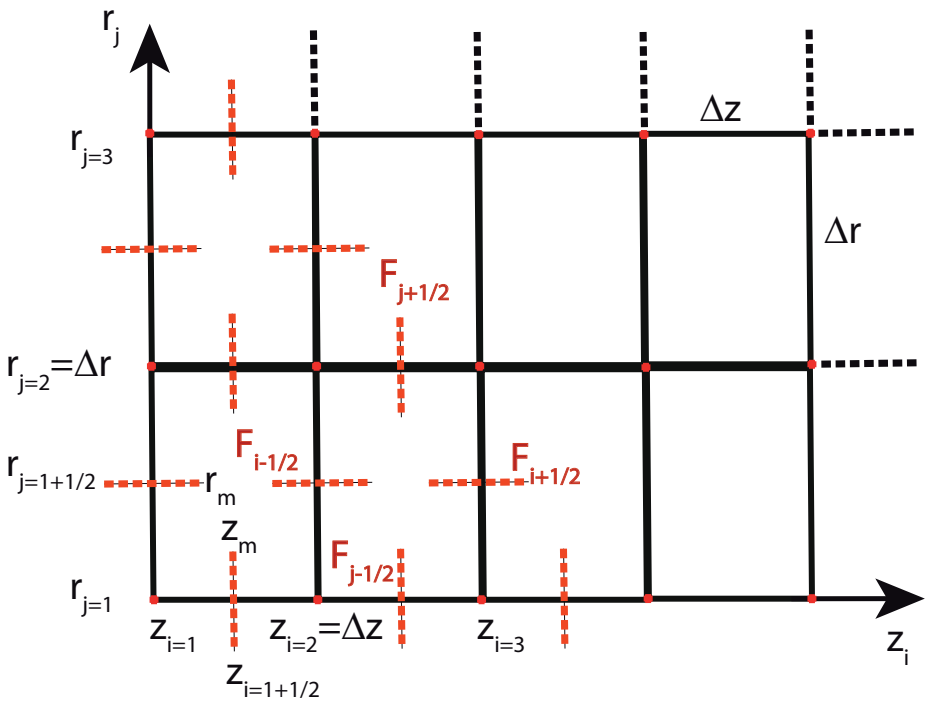


Figure 2.2 – Illustration of the discrete domain of simulation with grid points (red marks) and interfaces (dashed red lines)

conditions are the region where the streamer discharge is ignited and when the discharge is approaching the limits of the domain of simulation.

### 2.3.2 Poisson's solver

To solve Poisson's equation, we have developed a Poisson solver based on the successive overrelaxation method (SOR) in cylindrical symmetry ($\frac{\partial \phi}{\partial \theta}$=0). Assuming cylindrical symmetry, Poisson's equation in cylindrical coordinates can be written:

$$\frac{1}{r}\frac{\partial \phi}{\partial r} + \frac{\partial^2 \phi}{\partial r^2} + \frac{\partial^2 \phi}{\partial z^2} = \frac{-\rho}{\epsilon_0} \tag{2.10}$$

where $\rho$ is the charge density

Using L'hôpital's rule, the equation (2.10) can be rewritten as follows in the vicinity of the axis of symmetry ($r \to 0$):

$$2\frac{\partial^2 \phi}{\partial r^2} + \frac{\partial^2 \phi}{\partial z^2} = \frac{-\rho}{\epsilon_0} \tag{2.11}$$

Discrete forms of the equation (2.10) at $r \neq 0$ and (2.11) at $r = 0$, are derived using finite differences method with an additional term $(1 - W)\phi^N$, where $N$ is the number of iterations required for the convergence of the solver, and $W$ is a coefficient set between zero and one [*Demmel*, 1996]:

$$\phi_{ij}^{N+1} = \phi_{ij}^N + W(\alpha(\beta\phi_{ij-1}^N + \gamma\phi_{ij+1}^N + \xi(\phi_{i+1j}^N + \phi_{i-1j}^N) - (1/\alpha)\phi_{ij}^N) + \frac{\rho_{ij}}{\epsilon_0})) \quad (2.12)$$

$$\phi_{i1}^{N+1} = \phi_{i1}^N + W(\alpha(\beta\phi_{i2}^N + \gamma(\phi_{i+11}^N + \phi_{i-11}^N) - (1/\alpha)\phi_{i1}^N) + \frac{\rho_{i1}}{\epsilon_0})) \quad (2.13)$$

In the equation (2.13), because of the cylindrical symmetry assumption, we consider that $\phi_{ij-1} = \phi_{ij+1}$ when $j \to 1$.

The coefficients:

$$\begin{cases} \alpha = \frac{1}{\frac{2}{(\Delta r)^2} + \frac{2}{(\Delta z)^2}} \\ \beta = \frac{1}{(\Delta r)^2} + \frac{1}{2r_j\Delta r} \\ \gamma = \frac{1}{(\Delta r)^2} - \frac{1}{2r_j\Delta r} \\ \xi = \frac{1}{(\Delta z)^2} \end{cases}$$

can be easily found after the discretization of equations (2.10) and (2.11).

To calculate the potential at a point of coordinates $(i, j)$, points with coordinates $(i - 1, j)$, $(i + 1, j)$, $(i, j - 1)$ and $(i, j + 1)$ are needed. The equations (2.12) and (2.13) are used as follows:

1. In the first part of the solver, we calculate the potential in the cases of odd $i$ and $j$ (see yellow marks in Figure 2.3) and of even $i$ and $j$ (see red marks in Figure 2.3), respectively.
2. In the second part, we use the estimated potential values at the same iteration in the first part of the solver (yellow and red marks) to calculate the cases ($i$ odd, $j$ even) at the green marks and ($i$ even, $j$ odd) at the blue marks in Figure 2.3.

In the SOR method, the coefficient $0< W <1$ is called "weight" and is used to control the convergence of the solver (in our preliminary studies, we have seen that $W = 0.9$ leads to a fast convergent solver). $\phi^{N=1}$ is the first guessed solution and $\phi^{N+1}$ is the satisfied solution after $N + 1$ iterations.

The convergence criteria of the solver is based on the following relative error,

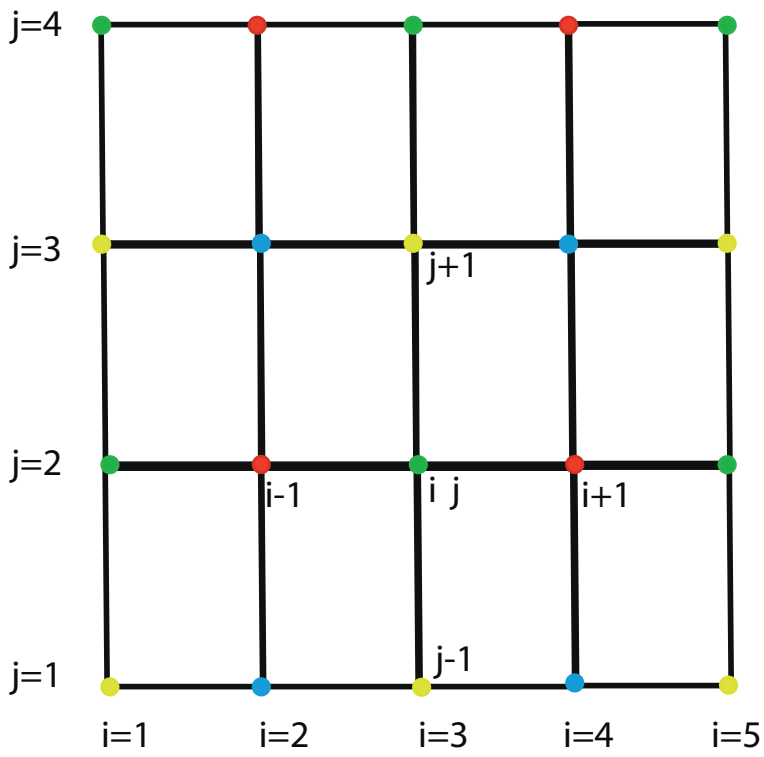


Figure 2.3 – Illustration of the discrete domain of simulation in case of Poisson's SOR solver.

which is the sum over all the relative errors in every point (red, blue, green, and yellow) averaged over the total number of points excluding the boundaries:

$$\frac{\delta\phi}{\phi} = \frac{1}{(N_z-2)(N_r-1)} \left( \sum_{i=1,j=1}^{Nz,Nr} \frac{\phi_{ij}^{N+1} - \phi_{ij}^{N}}{\phi_{ij}^{N}} \right) \tag{2.14}$$

when $\frac{\delta\phi}{\phi} \leq \varepsilon$, where $\varepsilon$ is the chosen precision, the solver stops running at a given number of iterations. The precision that has been chosen in our calculation is lower than $\varepsilon = 10^{-7}$. Under this precision, we conducted tests of the solver by comparing the analytical and numerical solutions of different electrostatic problems (punctual charge, charged filament, charged sphere, etc.) and we found a very good agreement. The solution of our solver has also been compared to the D03EBF module of the NAG FORTRAN library ($http://www.nag.co.uk$). The electric potential $\phi_{ij}$ is calculated locally at each point of coordinates ($i$, $j$) of the simulation domain.

One defines two sets of boundary conditions used in the present work:

**External Dirichlet boundary conditions and parallel plane-to-plane electrodes:** This configuration is governed by the following conditions $\phi(z = z_{i=1} = 0, r = r_{j=1,N_r}) = 0$, $\phi(z = z_{i=N_z} = d, r = r_{j=1,N_r}) = V$ and $\phi(z = z_{i=1,N_z}, r = r_{j=N_r}) = V\frac{z_i}{d}$, where $d$ and $V$ are the length of the simulation domain and the applied electric potential, respectively. This configuration is practical for the study of laboratory gas discharges propagating in an homogeneous electric field produced in parallel electrodes in the plane-to-plane configuration.

**Open boundary conditions and point-to-plane electrodes:** The open boundary conditions are based on the integral equation of the electric potential (2.7). The integral takes into account the effect of the density of the space charge as illustrated in Figure 2.4. To accelerate the computation, we take into account the effect of every local source satisfying $\rho(r^{'}, z^{'}) \geq \frac{\rho_{max}}{200}$, where $\rho_{max}$ is the maximum density of space charge. This configuration is practical to study streamer propagation in a specific region under a spatially homogeneous external electric field of large dimension. The integral is simply calculated at the first order ($\int f(x)dx = \sum_{i=1}^{i=m} f(x_i)\delta x$) every ten points and a linear interpolation between each two calculated points is used. After a few lines of calculations in cylindrical coordinates and considering $\theta^{'} = \pi + 2\theta$,

the effect of the space charge on the electric potential at the boundaries excluding the sources along the axis of symmetry ($\rho(r^{'} \neq 0, z^{'})$) is evaluated as follows [e.g., *Liu*, 2006]:

$$\phi_{\rho(r'\neq 0,z')} = \frac{1}{4\pi\epsilon_0} \iint \frac{dr^{'} dz^{'} r^{'} 2\pi\rho(r^{'}, z^{'})}{\sqrt{(r+r')^2 + (z-z')^2}} \frac{4K(k)}{2\pi} \tag{2.15}$$

where $\rho(r^{'}, z^{'})$ is the density of charge at the source point located at the position $r^{'} \neq 0$ and $z^{'} \neq 0$. The quantity $dr^{'} dz^{'} r^{'} 2\pi\rho(r^{'}, z^{'})$ is the net charge within two rings of radius $r^{'}$ and $r^{'} + dr^{'}$ and thickness $dz^{'}$ of a volume $\pi dz^{'}(r^{'} + dr^{'})^2 - \pi dz^{'}(r^{'})^2 \simeq 2\pi r^{'} dr^{'} dz^{'}$. The quantity $K(k)$ is the elliptic integral of first kind:

$$K(k) = \int_0^{\frac{\pi}{2}} (1 - k^2 \sin^2\theta)^{-\frac{1}{2}} d\theta \tag{2.16}$$

where $k^2 = 4\frac{rr^{'}}{(r+r^{'})^2+(z-z^{'})^2}$. The integral is calculated for each value of $k$, numerically at the first order.

If $r^{'} \to 0$, $k \to 0$, and $K(0) \to \frac{\pi}{2}$ the elementary net charge becomes $\rho(r^{'} = 0, z^{'})\pi(\frac{\Delta r^{'}}{2})^2 dz^{'}$ and thus the effect of the space charge located along the axis of the symmetry of the streamer ($\rho(r^{'} = 0, z^{'})$) is evaluated as follows:

$$\phi_{\rho(r'=0,z')} = \frac{1}{4\pi\epsilon_0} \int \frac{dz^{'}\pi(\frac{\Delta r^{'}}{2})^2 \rho(r^{'} = 0, z^{'})}{\sqrt{r^2 + (z-z')^2}} \tag{2.17}$$

At $r^{'} = 0$, we considered that the source points are located at a distance $\frac{\Delta r^{'}}{2}$ from the axis. Both equations (2.15) and (2.17) are used to calculate the space charge potential at the simulation domain boundaries.

Another interesting configuration to study the propagation of streamers in an inhomogeneous electric field [e.g., *Babaeva and Naidis*, 1996a,b] is the point-to-plane electrode configuration. In addition to the effects of the streamer space charge described by the equations (2.15) and (2.17), the effects of the image charge in the sphere of radius $b$ set to an electric potential $\phi_s$ and immersed in an homogeneous external electric field $E_0$ need to be taken into account (see Figure 2.5). At the surface of the sphere the electric field is high and weak far from it. Hence, this configuration allows the ignition of the streamer discharge near the sphere and for its propagation in a region of a weak electric field. It is a practical configuration

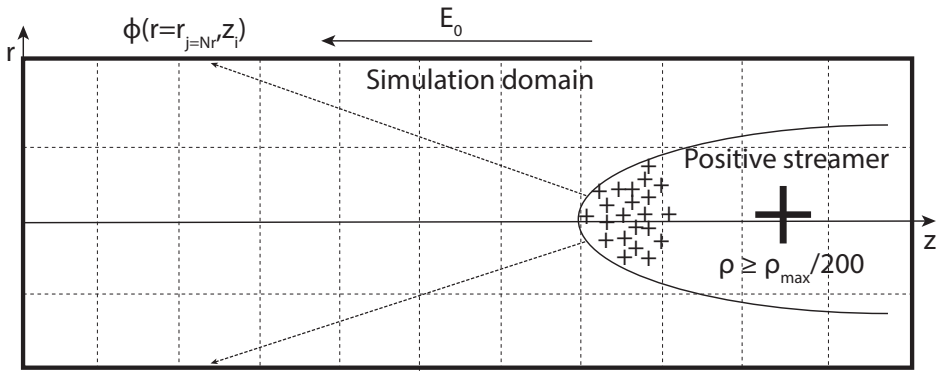


Figure 2.4 – Illustration of the effect of the streamer space charge on the electric potential at the border of the simulation domain (open boundary conditions).

to study sprite streamers and laboratory streamer discharges ignited in a point-to-plane electrodes configuration. in this case, the additional equations to add to equations (2.15) and (2.17) are the following [e.g., *Liu*, 2006]:

$$\phi_{\rho(r'\neq 0,z')} = \frac{1}{4\pi\epsilon_0}\iint \frac{dr'dz'r'(\frac{b}{l})2\pi\rho(r'\neq 0,z')}{\sqrt{(r+r'_c)^2+(z-z'_c)^2}}\frac{4K(k_c)}{2\pi} \tag{2.18}$$

$$\phi_{\rho(r'=0,z')} = \frac{1}{4\pi\epsilon_0}\int \frac{dz'(\frac{b}{l})\pi(\frac{\Delta r'}{2})^2\rho(r'=0,z')}{\sqrt{r^2+(z-z'_c)^2}} \tag{2.19}$$

where $z'_c = \frac{b^2}{l^2}(z'+b)-b$ and $r'_c = \frac{b^2}{l^2}r'$ are the coordinates of the image charge situated on the surface of the sphere, where $l = \sqrt{(b+z')^2+r'^2}$ is the distance between the observation point in the simulation domain and the center of the sphere.

In addition to the effects of image charges, a Laplacian electric potential $\phi_L$ needs to be added to the electric potential $\phi_{SD}$ calculated in the simulation domain (SD):

$$\phi_L = \phi_s\left(\frac{b}{l}\right) - E_0\left(1-\left(\frac{b}{l}\right)^3\right)(z+b) \tag{2.20}$$

Finally, we obtain the total potential as $\phi_{total} = \phi_L + \phi_\rho + \phi_{SD}$. Note that $\phi_\rho$ is calculated as the contributions of all the equations 2.15, 2.17, 2.18, and 2.19.

In order to optimize the computation time, we only take into account the effect of space charges when they are most significant, i.e., near the streamer head-region. Hence, one only considers the charge density fulfilling the condition $\rho(r',z') \geq \frac{\rho_{max}}{200}$.

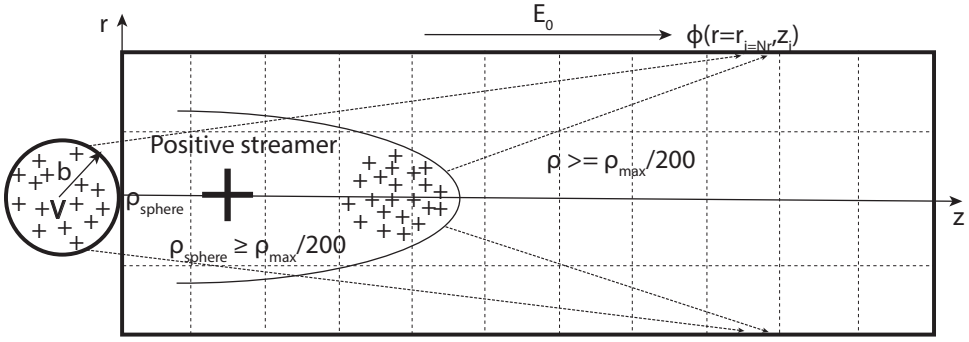


Figure 2.5 – Illustration of the effect of the streamer space charge and the sphere charge images on the border of the simulation domain (open boundary conditions and point-to-plane configuration)

### 2.3.3 Calculation of the photoionization process

The integral of photoionization presented in equation (2.6) can be rewritten in cylindrical coordinates as:

$$S_{\rm ph} = \iint \Gamma\zeta S_i \int_0^{2\pi} \frac{r^{'}}{4\pi} \frac{\exp(-\chi_{min} p_{o_2} R) - \exp(-\chi_{max} p_{o_2} R)}{R\ \ln\left(\frac{\chi_{max}}{\chi_{min}}\right)} d\theta^{'} dz^{'} dr^{'} \qquad (2.21)$$

where $R = \sqrt{r^2 - 2rr^{'}\cos\theta^{'} + r^{'2} + (z - z^{'})^2}$, $\Gamma = \frac{p_q}{p+p_q}$, and $\zeta = \xi\frac{\nu_*}{\nu_i}$. The coordinates $(r^{'}, z^{'})$ and $(r, z)$ are to localize the source and the photoelectron production, respectively.

One can identify a purely geometrical part and write it in a 3-D array of dimension ($N_r$,$N_r$,$N_z$) [e.g., *Liu*, 2006].

$$M_{ph}(r, z, r^{'}, z^{'}) = \int_0^{2\pi} \frac{r^{'}}{4\pi} \frac{\exp(-\chi_{min} p_{o_2} R) - \exp(-\chi_{max} p_{o_2} R)}{R\ \ln\left(\frac{\chi_{max}}{\chi_{min}}\right)} d\theta^{'} \qquad (2.22)$$

Noting $x = z - z^{'}$, one has $R = \sqrt{r^2 - 2rr^{'}\cos\theta^{'} + r^{'2} + x^2}$. Replacing in equation (2.22), one can reduce $M_{\rm ph}(r, z, r^{'}, z^{'})$ as $M_{ph}(r, r^{'}, x)$ and tabulate $M_{\rm ph}$ in a 3-D array. One can see, that if $r^{'} = 0$, then $S_{\rm ph} = 0$, which is not consistent with the numerical grid used because the sources of photoionization located along the axis of symmetry of the streamer also contribute the photoelectron production. In this case, we calculate differently the $M_{\rm ph}$ matrix along the axis. In this case, we

suppose that the photoionization sources are located at $r^{'} = \frac{\Delta r}{2}$:

$$M_{ph}(r, z, r^{'} = 0, z^{'}) = \int_0^{2\pi} \frac{\Delta r}{8\pi} \frac{\exp(-\chi_{min} p_{o_2} R) - \exp(-\chi_{max} p_{o_2} R)}{R \ \ln\left(\frac{\chi_{max}}{\chi_{min}}\right)} d\theta^{'} \quad (2.23)$$

where $R = \sqrt{r^2 - r\frac{\Delta r}{2}\cos\theta' + \frac{\Delta r^2}{2} + x^2}$. Finally, we solve the integral numerically at the first order.

The physical part contains the coefficients $\Gamma$, $\xi$ and $S_i$ and it is calculated numerically at the first order as well. In our case, we set $\chi_{min} = 3.5$ Torr$^{-1}$cm$^{-1}$, $\chi_{max} = 200$ Torr$^{-1}$cm$^{-1}$, and $\Gamma = 0.038$ at ground level [*Bourdon et al.*, 2007]. We assume $\zeta = 0.1$ [*Liu and Pasko*, 2004]. Rigorously, this parameter is a weak function of the local electric field based on a set of data given in [*Zheleznyak et al.*, 1982], however we have verified that the error introduced by this assumption in the streamer dynamics is negligible.

This photoionization integral approach is highly time consuming. To reduce the time consumption, we calculate it in the streamer head region and the region where the initial plasma cloud distribution is placed to ignite the streamer discharge. Outside these regions, we calculate the $S_{\text{ph}}$ term in only one over ten points and a linear interpolation between two calculated points is used (see Figure 2.6 and 2.7). This technical approach has been tested and compared with more advanced photoionization methods developed in [*Bourdon et al.*, 2007] and a very good agreement was obtained.

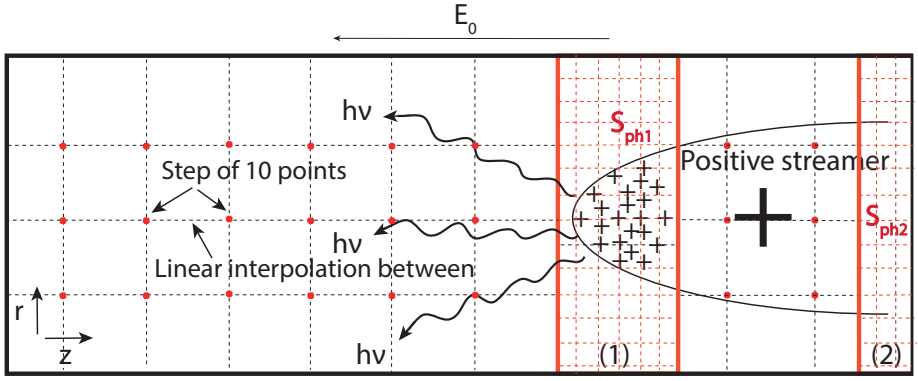


Figure 2.6 – Illustration of the photoionization process and the interpolation technique. Areas (1) and (2) are the regions where the photoionization is fully calculated, outside these regions, it is calculated every step of 10 points and a linear interpolation is considered between each two calculated points.

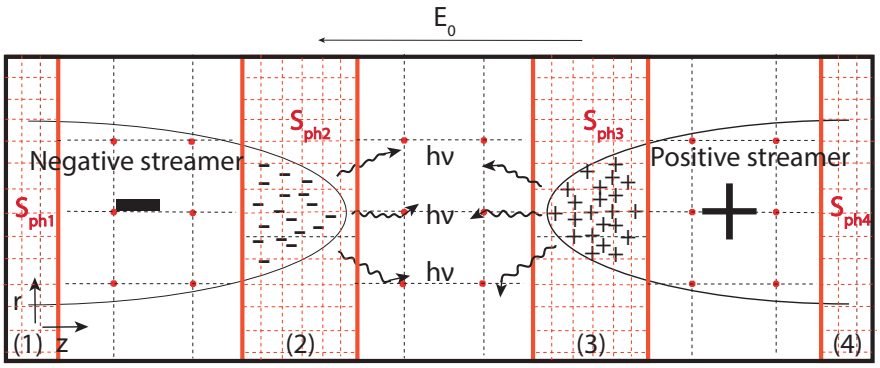


Figure 2.7 – Illustration of the photoionization process and the interpolation technique in case of head-on collision of positive and negative streamers. Areas (1), (2), (3), and (4) are the regions where the photoionization is fully calculated, outside these regions it is calculated every step of 10 points and a linear interpolation is performed between each two calculated points. When the streamers start approaching each other the areas (2) and (3) are merged into one area.

### 2.3.4 Drift-diffusion equations for electrons and ions

In this part, we show how we proceed to solve the equations (2.1)-(2.3) numerically. We first integrate the equations over the volume of the cell $V_{ij}$ following the finite volume method. Thus, one obtains:

$$\frac{\partial \bar{n}_\mathrm{e}}{\partial t} + \frac{1}{V_{ij}} \int \nabla . n_\mathrm{e} \vec{v}_\mathrm{e} dV - \frac{1}{V_{ij}} \int D_\mathrm{e} \nabla^2 n_\mathrm{e} dV = \bar{S}_\mathrm{e} \tag{2.24}$$

$$\frac{\partial \bar{n}_\mathrm{p}}{\partial t} = \bar{S}^+ \tag{2.25}$$

$$\frac{\partial \bar{n}_\mathrm{n}}{\partial t} = \bar{S}^- \tag{2.26}$$

where $\bar{n} = \frac{1}{V_{ij}} \int n dV$ represents the electron, positive, or negative ions density integrated over the volume of the cell. $\bar{S} = \frac{1}{V_{ij}} \int S(n) dV$ represents the electron, positive, or negative ions source terms integrated over the volume of the cell.

Using the Ostrogradsky's theorem, $\int_V \nabla . \vec{f} dV = \int_s \vec{f} . \vec{ds}$, where $\vec{ds}$ is the normal vector to an elementary surface. The second and third terms of the equation (2.24) , respectively become:

$$\int \nabla . n_\mathrm{e} \vec{v}_\mathrm{e} dV = \int n_\mathrm{e} \vec{v}_\mathrm{e} . \vec{ds} \tag{2.27}$$

$$\int D_\mathrm{e} \nabla^2 n_\mathrm{e} dV = \int D_\mathrm{e} \nabla . (\nabla n_\mathrm{e}) dV = \int D_\mathrm{e} (\nabla n_\mathrm{e}) . \vec{ds} \tag{2.28}$$

Finally, the equations (2.24)-(2.26) become:

$$\frac{\partial \bar{n}_{\mathrm{e}}}{\partial t} + \frac{1}{V_{ij}} \int n_{\mathrm{e}} \vec{v}_{\mathrm{e}} . \vec{ds} - \frac{1}{V_{ij}} \int D_{\mathrm{e}} (\nabla n_{\mathrm{e}}) . \vec{ds} = \bar{S}_{\mathrm{e}} \tag{2.29}$$

$$\frac{\partial \bar{n}_{\mathrm{p}}}{\partial t} = \bar{S}^{+} \tag{2.30}$$

$$\frac{\partial \bar{n}_{\mathrm{n}}}{\partial t} = \bar{S}^{-} \tag{2.31}$$

### 2.3.5 Numerical computation of source terms

We now proceed to the numerical resolution of the equations (2.30) and (2.31). Identifying the equations (2.30) and (2.31), to $\frac{\partial x}{\partial t} = g(x)$ and applying a Runge-Kutta 4 numerical scheme ($4^{th}$ order accurate in time) [*Schafer*, 2006]:

$$x^{t+\delta t} = x^{t} + \tfrac{\delta t}{6}(f_1 + 2f_2 + 2f_3 + f_4) \text{ where } f_1 = g(x),\ f_2 = g(x + \tfrac{\delta t}{2} f_1),$$
$$f_3 = g(x + \tfrac{\delta t}{2} f_2), \text{ and } f_4 = g(x + \delta t f_3),$$

and thus equations (2.30) and (2.31) become:

$$\bar{n}_{\mathrm{p}}^{t+\delta t} = \bar{n}_{\mathrm{p}}^{t} + \frac{\delta t}{6}(\bar{S}_1^{+} + 2\bar{S}_2^{+} + 2\bar{S}_3^{+} + \bar{S}_4^{+}) \tag{2.32}$$

$$\bar{n}_{\mathrm{n}}^{t+\delta t} = \bar{n}_{\mathrm{n}}^{t} + \frac{\delta t}{6}(\bar{S}_1^{-} + 2\bar{S}_2^{-} + 2\bar{S}_3^{-} + \bar{S}_4^{-}) \tag{2.33}$$

where $\bar{S}^{+} = \frac{1}{V_{ij}} \int S^{+}(n_{\mathrm{e}}) dV + \frac{1}{V_{ij}} \int S_{\mathrm{ph}}(n_{\mathrm{e}}) dV = \frac{1}{V_{ij}} \int \nu_i(n_{\mathrm{e}}) n_{\mathrm{e}} dV + \bar{S}_{\mathrm{ph}}(\bar{n}_e) = \nu_i(\bar{n}_{\mathrm{e}}) \bar{n}_{\mathrm{e}} + \bar{S}_{\mathrm{ph}}(\bar{n}_e)$. The same procedure is applied for $\bar{S}^{-} = \nu_a(\bar{n}_{\mathrm{e}}) \bar{n}_{\mathrm{e}}$

### 2.3.6 Discretization of fluxes

For one given grid cell $(i, j)$, the second and third terms of equation (2.29) are evaluated as follows:

$$\int n_{\mathrm{e}} \vec{v}_{\mathrm{e}} . \vec{ds} = F_{i+\frac{1}{2}} + F_{j+\frac{1}{2}} - F_{i-\frac{1}{2}} - F_{j-\frac{1}{2}} = \sum F \tag{2.34}$$

where $F_{i+\frac{1}{2}}$ is the convective flux at the interface located between the $i$ and $i+1$ (idem for $F_{j+\frac{1}{2}}$).

$$\int D_{\mathrm{e}}(\nabla n_{\mathrm{e}}).\vec{ds} = F^D_{i+\frac{1}{2}} + F^D_{j+\frac{1}{2}} - F^D_{i-\frac{1}{2}} - F^D_{j-\frac{1}{2}} = \sum F^D \tag{2.35}$$

where $F^D_{i+\frac{1}{2}}$ is the diffusive flux at the interface located between the grid points $i$ and $i+1$ (idem for the $F^D_{j+\frac{1}{2}}$). The explicit form of the convective and diffusive fluxes will be described in the Section 2.3.9.

In one grid cell $(i,j)$, the equation (2.29) becomes:

$$\bar{n}_{\mathrm{e}}^{t+\delta t} = \bar{n}_{\mathrm{e}}^{t} + \frac{\delta t}{V_{ij}} \sum F - \frac{\delta t}{V_{ij}} \sum F^D + \delta t(\bar{S}_{\mathrm{ph}} + \bar{S}_e^+ - \bar{S}_{\mathrm{e}}^-) \tag{2.36}$$

where $\bar{S}_{\mathrm{e}}^+ = \nu_i(\bar{n}_{\mathrm{e}})\bar{n}_e$, $\bar{S}_{\mathrm{e}}^- = \nu_a(\bar{n}_{\mathrm{e}})\bar{n}_e$ and $\bar{S}_{\mathrm{ph}} = \frac{1}{V_{ij}} \int S_{\mathrm{ph}}(n_{\mathrm{e}})dV = S_{\mathrm{ph}}(\bar{n}_{\mathrm{e}})$.

The term $\bar{S}_e = \bar{S}_{\mathrm{e}}^+ - \bar{S}_{\mathrm{e}}^- + \bar{S}_{\mathrm{ph}}$, where $\bar{S}_{\mathrm{e}}^+ = \nu_i(\bar{n}_{\mathrm{e}})\bar{n}_{\mathrm{e}}$ and $\bar{S}_{\mathrm{e}}^- = \nu_a(\bar{n}_{\mathrm{e}})\bar{n}_{\mathrm{e}}$. To calculate $\bar{S}_{\mathrm{e}}^+$ and $\bar{S}_{\mathrm{e}}^-$, we consider the equation $\frac{\partial n_{\mathrm{e}}}{\partial t} = S_{\mathrm{e}}^{\pm}$ and we follow the same procedure as in equations (2.30) and (2.31).

Finally, the streamer model discretized equations are the following:

$$\bar{n}_{\mathrm{e}}^{t+\delta t} = \bar{n}_{\mathrm{e}}^{t} + \frac{\delta t}{V_{ij}} \sum F - \frac{\delta t}{V_{ij}} \sum F^D - \delta t(\bar{S}_{\mathrm{ph}} + \bar{S}_e^+ - \bar{S}_{\mathrm{e}}^-) \tag{2.37}$$

$$\bar{n}_{\mathrm{p}}^{t+\delta t} = \bar{n}_{\mathrm{p}}^{t} + \frac{\delta t}{6}(\bar{S}_1^+ + 2\bar{S}_2^+ + 2\bar{S}_3^+ + \bar{S}_4^+) \tag{2.38}$$

$$\bar{n}_{\mathrm{n}}^{t+\delta t} = \bar{n}_{\mathrm{n}}^{t} + \frac{\delta t}{6}(\bar{S}_1^- + 2\bar{S}_2^- + 2\bar{S}_3^- + \bar{S}_4^-) \tag{2.39}$$

$$\phi_{ij}^{N+1} = \phi_{ij}^{N} + W(\alpha(\beta\phi_{ij-1}^{N} + \gamma\phi_{ij+1}^{N} + \xi(\phi_{i+1j}^{N} + \phi_{i-1j}^{N}) - (1/\alpha)\phi_{ij}^{N}) + \frac{\rho_{ij}}{\epsilon_0})) \tag{2.40}$$

$$\phi_{i1}^{N+1} = \phi_{i1}^{N} + W(\alpha(\beta\phi_{i2}^{N} + \gamma(\phi_{i+11}^{N} + \phi_{i-11}^{N}) - (1/\alpha)\phi_{i1}^{N}) + \frac{\rho_{i1}}{\epsilon_0})) \tag{2.41}$$

$$\bar{S}_{\rm ph}(\bar{n}_{\rm e}) = \iint \Gamma\zeta \bar{S}_i(\bar{n}_{\rm e}) M_{\rm ph}(r, z, r^{'}, z^{'}) dz^{'} dr^{'} \tag{2.42}$$

where $\bar{S}_i = \nu_i(\bar{n}_{\rm e})\bar{n}_{\rm e}$. Depending on the studied configuration such as plane-to-plane electrodes in large scale external electric field or point-to-plane electrodes, equations (2.15), (2.17) and (2.18), (2.19) and (2.20) need to be added to the above system of equations, respectively.

### 2.3.7 Flux corrected transport (FCT) technique for tracking steep gradients

The electric field in the streamer head region varies within short time scales and short characteristic lengths (respectively, picoseconds and micrometers), which is illustrated by steep gradients. To capture these steep gradients, a specific numerical scheme to solve the drift-diffusion equation (2.29) is required. Indeed, the simple use of either high order schemes ($2^{nd}$ or higher) or low order scheme ($1^{st}$ order), both lead to significant numerical dispersion or numerical diffusion, respectively. Usually, numerical dispersion is the appearance of a numerical noise and its amplification to strong numerical oscillations through time of simulation. These are generated by the use of high order schemes. The numerical diffusion generated by the use low order schemes results in smoothing and decrease of the amplitude of the solution. To illustrate the numerical dispersion and diffusion, we conducted numerical tests over a one-dimension advection equation under periodic spatial conditions transporting from the left to right a Gaussian and rectangular functions (see Figure 2.8 and 2.9) using high, and low order schemes, respectively:

$$\frac{\partial n_{\rm e}}{\partial t} + v\frac{\partial n_{\rm e}}{\partial z} = 0 \tag{2.43}$$

where $v$ is a propagation velocity.

An example of a low order scheme is the upwind scheme [*Zalesak*, 1979, see Appendix]. In this case, the drift flux is calculated as follows:

$$\begin{cases} F_{i+\frac{1}{2}} = n_{e_i} v_{e_{i+\frac{1}{2}}} S_{i+\frac{1}{2}} \text{ if } v_{e_{i+\frac{1}{2}}} \geq 0 \\ F_{i+\frac{1}{2}} = n_{e_{i+1}} v_{e_{i+\frac{1}{2}}} S_{i+\frac{1}{2}} \text{ if } v_{e_{i+\frac{1}{2}}} < 0 \end{cases}$$

The above first-order scheme produces significant diffusion (see Figure 2.9).

An example of high order scheme is the $2^{nd}$ order finite difference scheme [*Zalesak*, 1979, see Appendix]. The drift flux is calculated as follows: $F_{i+\frac{1}{2}} = \frac{n_{e_i}+n_{e_{i+1}}}{2} v_{e_{i+\frac{1}{2}}} S_{i+\frac{1}{2}}$ The latter generates numerical oscillations in the electron density solution, along with negative values, and amplify them through time (see Figure 2.8). To avoid numerical dispersion, in some situations diffusive fluxes are added to the high-order fluxes.

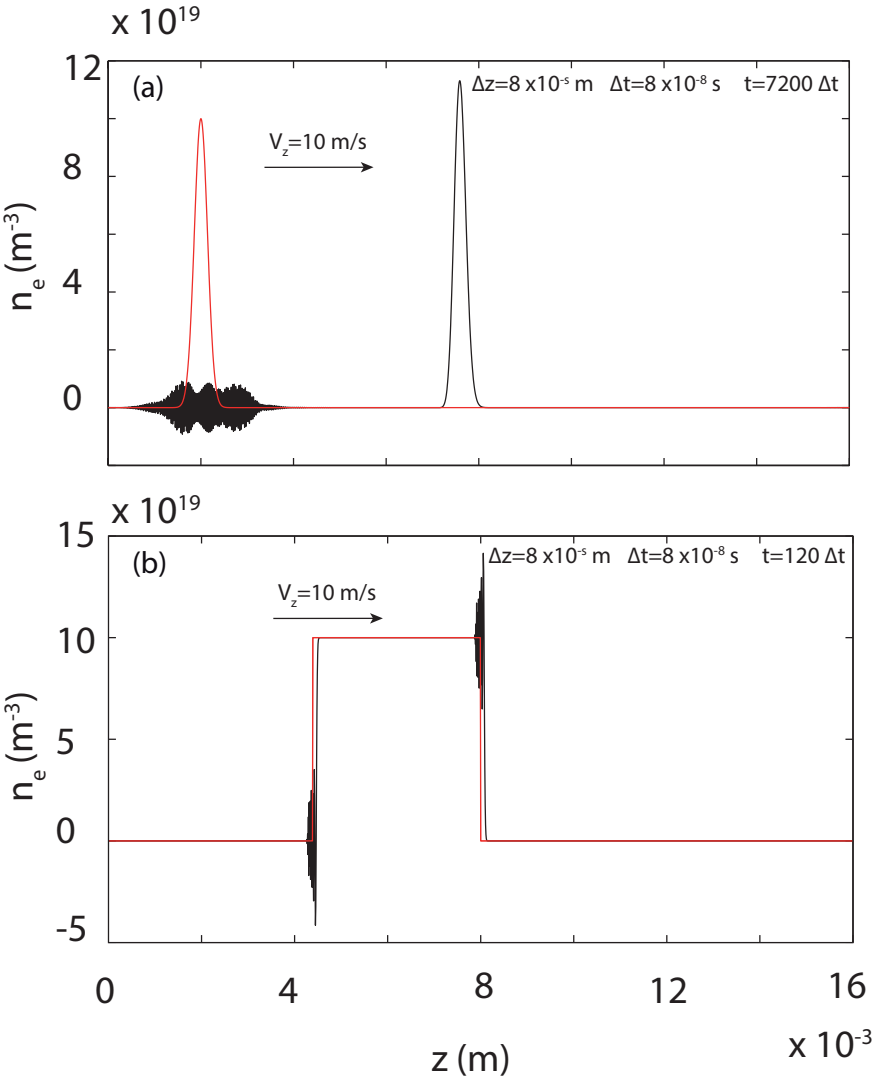


Figure 2.8 – (a)-(b) Illustration of the numerical oscillations generated by the use of $2^{nd}$ order fluxes in the advection equation while transporting a Gaussian and rectangular functions under spatially periodic conditions. Red and black lines are the initial conditions and the transported solutions, respectively.

For the numerical diffusion, we use a FCT numerical technique that involves anti-diffusive fluxes and which we expose just below.

To solve numerically the problem of capturing steep gradients in the streamer discharge problem, a flux corrected transport (FCT) technique is employed. Developed by *Boris and Book* [1973] in one dimension to solve fluid shocks numerically, it was later generalized by *Zalesak* [1979] to multi-dimensional fluid problems. The FCT technique preserves the correct transport of the solution of the equation (2.37) through time. The Figure 2.9 shows a transport from left to right (after $3 \times 10^4$ time steps $\Delta t = 8 \times 10^{-8}$s) of both a Gaussian function and a rectangular function using equation (2.43) with FCT (solid lines) and without the use of FCT using the upwind numerical scheme (dashed lines) [see online supporting information]. The non-diffusive and non-dispersive aspects of the FCT and the diffusion produced by the use of the upwind can be clearly seen in Figure 2.9. The FCT technique was used by several groups in association with various techniques to solve related numerical issues. [e.g., *Morrow*, 1981; *Morrow and Cram*, 1985; *Dhali and Williams*, 1985, 1987; *Kunhardt and Wu*, 1987; *Vitello et al.*, 1994; *Bourdon et al.*, 2007].

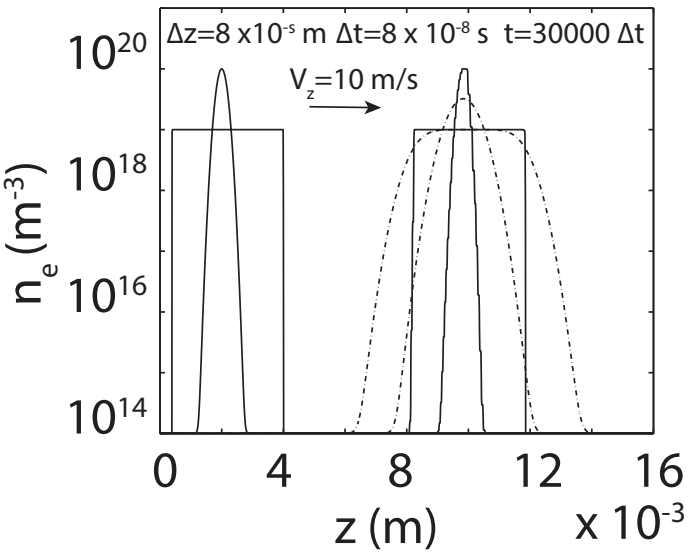


Figure 2.9 – Left: initial conditions. Right: numerical solution calculated using the FCT technique (solid lines) and without FCT, using the upwind numerical scheme (dashed lines) after $30000\Delta t$ transport time.

The FCT combines two kinds of fluxes: high order and low order. In the present

work, the low order fluxes are calculated in a unique time step ($\delta t$) using the upwind scheme and high order fluxes are computed in two time steps, namely predictive and corrective (see Appendix A). In the present model, we use the least time consuming scheme which is the Lax-Wendroff predictive-corrective time steps. The high order fluxes are calculated using either finite difference method or Lagrange polynomial approach (see below). In a standard case, the $m^{th}$ order flux is defined as:

$$F^m_{i+\frac{1}{2}} = n^m_{\mathrm{e}_{\mathrm{i}+\frac{1}{2}}} v_{e_{i+\frac{1}{2}}} S_{i+\frac{1}{2}} \tag{2.44}$$

where $n^m_{\mathrm{e}_{\mathrm{i}+\frac{1}{2}}}$ is the density at the $m^{th}$ order evaluated at the interface between the grid cells $i$ and $i+1$.

However, in case of streamer simulations, the use of the FCT technique developed by [*Zalesak*, 1979] produces numerical oscillations along the axis of symmetry of the streamer. To solve this problem, we have developed a technique which is based on the use of a logarithmic function to calculate the density at the $m^{th}$ order, and combined with $4^{th}$ order dissipative fluxes (see [*Kuzmin et al.*, 2012, pp. 23-65]). The logarithmic function reduces the dispersive character of the high order flux and ensures the positivity of the solution. Hence, we redefine the $m^{th}$ order flux as:

$$F^m_{i+\frac{1}{2}} = 10^{\left(n^m_{\mathrm{e}_{\mathrm{i}+\frac{1}{2}}}\right)} v_{e_{i+\frac{1}{2}}} S_{i+\frac{1}{2}} \tag{2.45}$$

where $10^{\left(n_{\mathrm{e}_{\mathrm{i}+\frac{1}{2}}}\right)}$ is the $m^{th}$ order density estimated at the interface $i+\frac{1}{2}$ using a logarithmic function.

**Finite differences approach**

Using the finite differences approach (see also the appendix in [*Zalesak*, 1979]) we write the $2^{nd}$, $4^{th}$, $6^{th}$, and $8^{th}$ high order schemes, respectively, as follows:

$$n^{m=2}_{\mathrm{e}_{\mathrm{i}+\frac{1}{2}}} = \frac{1}{2}(\log(n_{e_{i+1}}) + \log(n_{e_i})) \tag{2.46}$$

$$n_{e_{i+\frac{1}{2}}}^{m=4} = \frac{7}{12}(\log(n_{e_{i+1}}) + \log(n_{e_i})) - \frac{1}{12}(\log(n_{e_{i+2}}) + \log(n_{e_{i-1}})) \tag{2.47}$$

$$n_{e_{i+\frac{1}{2}}}^{m=6} = \frac{87}{80}(\log(n_{e_{i+1}})+\log(n_{e_i}))-\frac{2}{15}(\log(n_{e_{i+2}})+\log(n_{e_{i-1}}))+\frac{1}{60}(\log(n_{e_{i+3}})+\log(n_{e_{i-2}})) \tag{2.48}$$

$$n_{e_{i+\frac{1}{2}}}^{m=8} = \frac{533}{840}(\log(n_{e_{i+1}}) + \log(n_{e_i})) - \frac{130}{840}(\log(n_{e_{i+2}}) + \log(n_{e_{i-1}})) + \frac{29}{840}(\log(n_{e_{i+3}}) + \log(n_{e_{i-2}})) - \frac{1}{280}(\log(n_{e_{i+4}}) + \log(n_{e_{i-3}})) \tag{2.49}$$

The different coefficients of the above high order fluxes are calculated based on the $m^{th}$ order spatial derivative

$$\frac{\partial f^m}{\partial x}\Big|_{x_i} = \frac{F_{i+\frac{1}{2}}^m - F_{i-\frac{1}{2}}^m}{\Delta x} \tag{2.50}$$

Through the finite difference methods, the fourth order approximation of the derivative $\frac{\partial f^m}{\partial x}\,|_{x_i}$, is written as:

$$\frac{\partial f^{m=4}}{\partial x}\Big|_{x_i} = \frac{8}{12\Delta x}(f_{i+1} - f_{i-1}) - \frac{1}{12\Delta x}(f_{i+2} - f_{i-2}) \tag{2.51}$$

and the associated fourth-order centered fluxes related to grid cell $(i, j)$ can be written as:

$$F_{i+\frac{1}{2}}^{m=4} = \alpha f_{i+1} + \beta f_i + \gamma f_{i+2} + \delta f_{i-1} \tag{2.52}$$

$$F_{i-\frac{1}{2}}^{m=4} = \alpha f_i + \beta f_{i-1} + \gamma f_{i+1} + \delta f_{i-2} \tag{2.53}$$

From equation (2.50), (2.52) and (2.53), we get:

$$\frac{\partial f^{m=4}}{\partial x}\Big|_{x_i} = \frac{(\alpha - \gamma)}{\Delta x} f_{i+1} + \frac{(\beta - \alpha)}{\Delta x} f_i + \frac{\gamma}{\Delta x} f_{i+2} + \frac{(\delta - \beta)}{\Delta x} f_{i-1} - \delta f_{i-2} \tag{2.54}$$

From equations (2.51) and (2.54), we get:

$$\begin{cases} \alpha - \gamma = 8/12 \\ \beta - \alpha = 0 \\ \gamma = \text{-}1/12 \\ \delta - \beta = \text{-}8/12 \\ \delta = \text{-}1/12 \end{cases}$$

Hence, the values of the coefficients of the fourth-order flux are: $\delta = -1/12$, $\gamma = -1/12$, $\alpha = 7/12$, and $\beta = 7/12$. The same procedure can be applied to the other high order fluxes.

**Lagrange polynomial approach**

High order flux coefficients can also be derived using a Lagrange polynomial approach:

$$n_{\mathrm{e_{i+\frac{1}{2}}}}^{m=2} = \frac{1}{2}(\log(n_{e_{i+1}}) + \log(n_{e_i})) \tag{2.55}$$

$$n_{\mathrm{e_{i+\frac{1}{2}}}}^{m=4} = \frac{9}{16}(\log(n_{e_{i+1}}) + \log(n_{e_i})) - \frac{1}{16}(\log(n_{e_{i+2}}) + \log(n_{e_{i-1}})) \tag{2.56}$$

$$n_{\mathrm{e_{i+\frac{1}{2}}}}^{m=6} = \frac{75}{128}(\log(n_{e_{i+1}})+\log(n_{e_i}))-\frac{25}{256}(\log(n_{e_{i+2}})+\log(n_{e_{i-1}}))+\frac{3}{256}(\log(n_{e_{i+3}})+\log(n_{e_{i-2}})) \tag{2.57}$$

$$\begin{aligned} n_{\mathrm{e_{i+\frac{1}{2}}}}^{m=8} = {} & \frac{1225}{2048}(\log(n_{e_{i+1}}) + \log(n_{e_i})) - \frac{245}{2048}(\log(n_{e_{i+2}}) + \log(n_{e_{i-1}}))+ \\ & \frac{49}{2048}(\log(n_{e_{i+3}}) + \log(n_{e_{i-2}})) - \frac{5}{2048}(\log(n_{e_{i+4}}) + \log(n_{e_{i-3}})) \end{aligned} \tag{2.58}$$

Through a Lagrange polynomial definition, we calculate the fourth-order centered flux coefficients as follows:

$$P^m = \sum_{i=1}^{i=m} n_{\mathrm{e_i}} L_i(x) \tag{2.59}$$

$$\text{where } L_i(x) = \Pi_{j=1, j\neq i}^{j=m} \frac{x - x_j}{x_i - x_j}$$

For $m = 4$ and using equation (2.59) of Lagrange polynomial, one gets:

$$P^{m=4} = n_{\mathrm{e_1}} L_1 + n_{\mathrm{e_2}} L_2 + n_{\mathrm{e_3}} L_3 + n_{\mathrm{e_4}} L_4 \tag{2.60}$$

$$L_1(x) = \frac{x - x_2}{x_1 - x_2}\frac{x - x_3}{x_1 - x_3}\frac{x - x_4}{x_1 - x_4} \tag{2.61}$$

$$L_2(x) = \frac{x - x_1}{x_2 - x_1}\frac{x - x_3}{x_2 - x_3}\frac{x - x_4}{x_2 - x_4} \tag{2.62}$$

$$L_3(x) = \frac{x - x_1}{x_3 - x_1}\frac{x - x_2}{x_3 - x_2}\frac{x - x_4}{x_3 - x_4} \tag{2.63}$$

$$L_4(x) = \frac{x - x_1}{x_4 - x_1}\frac{x - x_2}{x_4 - x_2}\frac{x - x_3}{x_4 - x_3} \tag{2.64}$$

where $x_1 = 0$, $x_2 = \Delta x$, $x_3 = 2\Delta x$ and $x_4 = 3\Delta x$ and when $x_{i+\frac{1}{2}} = x_2 + \frac{\Delta x}{2}$ (for centered flux)

$$L_1(x) = -\frac{1}{16} \tag{2.65}$$

$$L_2(x) = \frac{9}{16} \tag{2.66}$$

$$L_3(x) = \frac{9}{16} \tag{2.67}$$

$$L_4(x) = -\frac{1}{16} \tag{2.68}$$

and finally:

$$P^{m=4} = \frac{9}{16}(n_{e_{i+1}} + n_{e_i}) - \frac{1}{16}(n_{e_{i+2}} + n_{e_{i-1}}) \tag{2.69}$$

If one wishes to use $8^{th}$ order fluxes (equations (2.49) and (2.58)) mentioned in the present work, everywhere in the simulation domain, which are more accurate (less diffusive than the $4^{th}$ order fluxes) [*Kuzmin et al.*, 2012, pp. 23-65] but time consuming, at cells located at $(i, j = 1)$, $(i, j = 2)$, or $(i, j = 3)$ near the axis of symmetry, we need to define the fluxes based on densities: ($n_{e_{j-3}}$, $n_{e_{j-2}}$, $n_{e_{j-1}}$), ($n_{e_{j-3}}$, $n_{e_{j-2}}$), and ($n_{e_{j-3}}$), respectively. Hence, non-centered fluxes with new coefficients need to be calculated. We use a Lagrange polynomial approach and develop $8^{th}$ order non-centered fluxes at $j$=1, 2, and 3, which correspond to radial distances $y = \frac{\Delta r}{2}$, $y = 3\frac{\Delta r}{2}$, and $y = 5\frac{\Delta r}{2}$, respectively:

$j = 1$

$$n^{m=8}_{e_{j+\frac{1}{2}}} = \frac{1}{2048}(429\log(n_{e_j}) + 3003\log(n_{e_{j+1}}) - 3003\log(n_{e_{j+2}}) + 3003\log(n_{e_{j+3}}) \\ -2145\log(n_{e_{j+4}}) + 1001\log(n_{e_{j+5}}) - 273\log(n_{e_{j+6}}) + 33\log(n_{e_{j+7}}) \tag{2.70}$$

$j = 2$

$$n^{m=8}_{e_{j+\frac{1}{2}}} = \frac{1}{2048}(-33\log(n_{e_{j-1}}) - 693\log(n_{e_j}) + 2079\log(n_{e_{j+1}}) - 1155\log(n_{e_{j+2}}) \\ -693\log(n_{e_{j+3}}) - 297\log(n_{e_{j+4}}) + 77\log(n_{e_{j+5}}) - 9\log(n_{e_{j+6}}) \tag{2.71}$$

$j = 3$

$$n^{m=8}_{e_{j+\frac{1}{2}}} = \frac{1}{2048}(9\log(n_{e_{j-2}}) - 105\log(n_{e_{j-1}}) + 945\log(n_{e_j}) + 1575\log(n_{e_{j+1}}) \\ -525\log(n_{e_{j+2}}) + 189\log(n_{e_{j+3}}) - 45\log(n_{e_{j+4}}) + 5\log(n_{e_{j+5}}) \tag{2.72}$$

We also evaluate the fluxes at radial distances $y = 9\frac{\Delta r}{2}$, $y = 11\frac{\Delta r}{2}$, and $y = 13\frac{\Delta r}{2}$, which correspond, respectively to grid cells coordinates:

$j = N_r - 3$

$$n^{m=8}_{e_{j+\frac{1}{2}}} = \frac{1}{2048}(5\log(n_{e_{j-4}}) - 45\log(n_{e_{j-3}}) - 189\log(n_{e_{j-2}}) - 525\log(n_{e_{j-1}}) \\ -1575\log(n_{e_j}) - 945\log(n_{e_{j+1}}) - 105\log(n_{e_{j+2}}) + 9\log(n_{e_{j+3}}) \tag{2.73}$$

$j = N_r - 2$

$$n^{m=8}_{e_{j+\frac{1}{2}}} = \frac{1}{2048}(-9\log(n_{e_{j-5}}) - 77\log(n_{e_{j-4}}) - 297\log(n_{e_{j-3}}) - 693\log(n_{e_{j-2}}) \\ -1155\log(n_{e_{j-1}}) + 2079\log(n_{e_j}) + 693\log(n_{e_{j+1}}) - 33\log(n_{e_{j+2}}) \tag{2.74}$$

$j = N_r - 1$

$$n_{e_{j+\frac{1}{2}}}^{m=8} = \frac{1}{2048}(33\log(n_{e_{j-6}}) - 273\log(n_{e_{j-5}}) - 1001\log(n_{e_{j-4}}) - 2145\log(n_{e_{j-3}}) \\ -3003\log(n_{e_{j-2}}) - 3003\log(n_{e_{j-1}}) + 3003\log(n_{e_j}) + 429\log(n_{e_{j+1}}) \tag{2.75}$$

The same $8^{th}$ order fluxes to be applied to the cells located at coordinates $(j, i = 1, 2, 3, N_z - 3, N_z - 2, \text{ and } N_z - 1)$.

In this manuscript, we use the $4^{th}$ order flux based on finite differences in the simulation domain and a modified $4^{th}$ order flux around $j = 1$. In cylindrical symmetry, we suppose $n_{e_{j-1}} = n_{e_{j+1}}$ and thus at $j = 1$:

$$n_{e_{j+\frac{1}{2}}}^{m=4} = \frac{7}{12}(\log(n_{e_{j+1}}) + \log(n_{e_j})) - \frac{1}{12}(\log(n_{e_{j+2}}) + \log(n_{e_{j+1}})) \tag{2.76}$$

As mentioned previously, the high order schemes are accurate but very dispersive and produce spurious oscillations along and near the axis of symmetry of streamers. An example that shows the kind of oscillations produced by the FCT along the streamer axis is illustrated in Figure 2.10 (a). In order to damp these numerical oscillations in streamer simulations, a predictive-corrective time step method coupled with the use of the logarithmic function is not sufficient. Indeed, we have observed the amplification of small density fluctuations in the process of transport due to the source terms. Thus, fourth order dissipative fluxes are added in the corrective-time step to the high order fluxes to reduce their highly dispersive propriety (see [*Kuzmin et al.*, 2012, pp. 23-65]). An illustration of the power of this solution to remove oscillations is illustrated in Figure 2.10 (b). The fourth-order dissipative fluxes [*Kuzmin et al.*, 2012, pp. 23-65] are the following:

$$F_{i+\frac{1}{2}}^{D,m=4} = -\mid v_{e_{i+\frac{1}{2}}} \mid (\frac{3}{16}(n_{e_{i+1}} - n_{e_i}) - \frac{1}{16}(n_{e_{i+2}} - n_{e_{i-1}}))S_{i+\frac{1}{2}} \tag{2.77}$$

Note that we do not apply a logarithmic approximation to the dissipative fluxes because they are diffusive. They are only added to the drift fluxes along the $z$-axes because of the relative importance of the drift along $z$-axes compared to that along the $r$-axes.

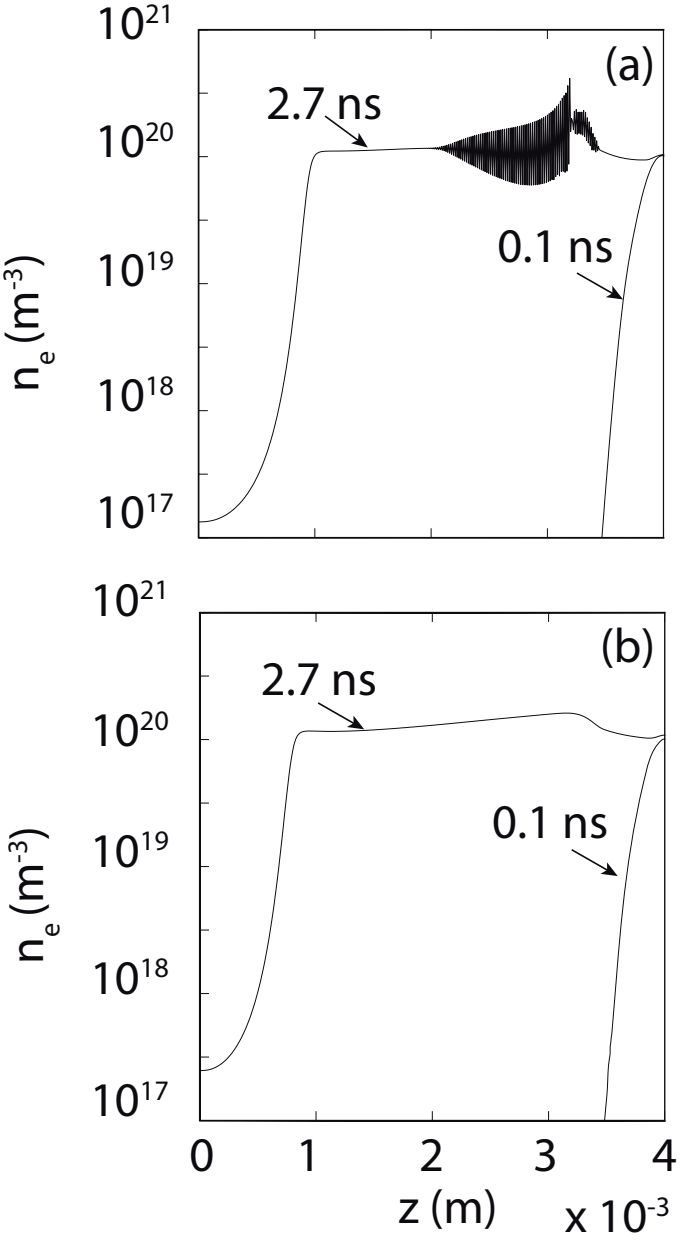


Figure 2.10 – (a) Illustration of the FCT numerical oscillations generated in case of a positive streamer. This is a simulation of double headed streamer: positive and negative in parallel plane-to-plane electrodes configuration. The applied external electric field is $E_0 = 50$ kV/cm and streamers propagate in a background homogeneous electron density $n_{back} = 10^{14}$ m$^{-3}$. The streamers are ignited by placing a Gaussian of plasma cloud in the middle of the axis of symmetry, with characteristic sizes: $\sigma_z = 0.0002$ m, $\sigma_r = 0.0002$ m, and $n_{e_0} = 10^{20}$ m$^{-3}$. We show only the positive streamer part moving from the right to the left. (b) The same simulation as in Figure 2.10, but numerical oscillations produced by the FCT were removed through the use of the $4^{th}$ order dissipative fluxes combined with the logarithmic function.

**The diffusive fluxes** The diffusive fluxes of equation (2.35) are evaluated based on the $1^{st}$ order forward finite differences scheme as follows: $F^D_{i+\frac{1}{2}} = D_{\mathrm{e}} \frac{n_{\mathrm{e}_{i+1}} - n_{\mathrm{e}_i}}{\Delta z} S_{i+\frac{1}{2}}$ and the same method is applied to $j$-axis.

### 2.3.8 Upwind scheme and boundary conditions

In case of streamer modeling, the upwind flux along z-axis is:

$$F_{i+\frac{1}{2}} = n_{e_i} v_{e_{i+\frac{1}{2}}} S_{i+\frac{1}{2}} \text{ if } v_{e_{i+\frac{1}{2}}} \geq 0$$
$$F_{i+\frac{1}{2}} = n_{e_{i+1}} v_{e_{i+\frac{1}{2}}} S_{i+\frac{1}{2}} \text{ if } v_{e_{i+\frac{1}{2}}} < 0$$

where $v_{e_{i+\frac{1}{2}}} = \mu_{i+\frac{1}{2}} E_{i+\frac{1}{2}}$, $\mu_{i+\frac{1}{2}} = \frac{\mu_i + \mu_{i+1}}{2}$ and $E_{i+\frac{1}{2}} = -\frac{\partial \phi}{\partial z} = -\frac{\phi_{i+1} - \phi_i}{\Delta z}$ are the electron drift velocity, the electron mobility and electric field evaluated at the interface $i + \frac{1}{2}$ (see Figure 2.2). The same procedure to be applied for the $r$-axis. From the formulation of the above fluxes, one can see that they are not symmetric if either $v_{\mathrm{e}} < 0$ or $v_{\mathrm{e}} \geq 0$. In order to get a symmetrical results (same properties: electric field, velocity, etc) for a given streamer ignited from the right or the left of the simulation domain, the mobility needs to be evaluated at the interface $i + \frac{1}{2}$ as well as the velocity as mentioned above. Moreover, the total electric field at a given point of coordinate $(i, j)$ must be averaged to estimate the mobility $\mu_{i,j}$:

$$E_{i,j} = \sqrt{E_r^2 + E_z^2} = \sqrt{\left(\frac{E_{i+\frac{1}{2}} + E_{i-\frac{1}{2}}}{2}\right)^2 + \left(\frac{E_{j+\frac{1}{2}} + E_{j-\frac{1}{2}}}{2}\right)^2}$$

For the boundary conditions, we assume the equality between the flux going in and out of the cell $(i, j)$ at the boundaries of the simulation domain, in order to avoid the accumulation of electron density and hence high density of charge. Thus, we implement the following conditions:

For $v_{e_z} \geq 0$ and $i = 1$:

$$F_{i-\frac{1}{2}} = n_{e_{i-1}} v_{e_{i-\frac{1}{2}}} S_{i-\frac{1}{2}} = n_{e_i} v_{e_{i+\frac{1}{2}}} S_{i+\frac{1}{2}} = F_{i+\frac{1}{2}}$$

For $v_{e_z} < 0$ and $i = 1$:

$$F_{i-\frac{1}{2}} = n_{e_i} v_{e_{i-\frac{1}{2}}} S_{i-\frac{1}{2}} = n_{e_i} (2 v_{e_{i+\frac{1}{2}}} - v_{e_{i+\frac{3}{2}}}) S_{i-\frac{1}{2}} \text{ where } v_{e_{i+\frac{1}{2}}} = \frac{v_{e_{i-\frac{1}{2}}} + v_{e_{i+\frac{3}{2}}}}{2}$$

This condition prevents the development of extremely high non-physical values of the electric field at $(i = 1, j = 1, N_r)$ in case of open boundary conditions and sphere-to-plane configuration.

For $v_{e_r} \geq 0$ and $j = 1$:

$F_{j-\frac{1}{2}} = n_{e_{j-1}} v_{e_{j-\frac{1}{2}}} S_{j-\frac{1}{2}} = 0$ where the surface along the axis is equal to zero.

For $v_{e_r} < 0$ and $j = N_r$:

$$F_{j+\frac{1}{2}} = n_{e_{j+1}} v_{e_{j+\frac{1}{2}}} S_{j+\frac{1}{2}} = n_{e_j} v_{e_{j-\frac{1}{2}}} S_{j-\frac{1}{2}} = F_{j-\frac{1}{2}}$$

### 2.3.9 Simulation time step

For the accuracy of simulation, one needs to verify that the numerical transport velocity of the information is greater than the physical velocity of the treated problem. This is called Courant-Friedrichs-Lewy condition, which is translated as $\delta t < \frac{\Delta x}{v_e}$ and must be respected to avoid the appearance of non-physical values of the electron density (e.g., negative values). In case of the FCT, the condition becomes $\delta t < \frac{\Delta x}{2v_e}$ [*Morrow*, 1981, references therein]. The time step $\delta t$ used in the simulation is calculated as in [*Vitello et al.*, 1994]. Three time scales, courant, ionization and dielectric relaxation are defined, respectively:

$$\delta t_C = \min_{\mathrm{i,j}}^{\mathrm{N_z,N_r}} \left( \frac{\Delta \mathrm{r}}{\mathrm{v_r}}, \frac{\Delta \mathrm{z}}{\mathrm{v_z}} \right) \tag{2.78}$$

$$\delta t_I = \min_{\mathrm{i,j}}^{\mathrm{N_z,N_r}} \left( \frac{1}{(\nu_\mathrm{i} - \nu_\mathrm{a})} \right) \tag{2.79}$$

$$\delta t_D = \min_{\mathrm{i,j}}^{\mathrm{N_z,N_r}} \left( \frac{\epsilon_0}{\mathrm{e}\mu_\mathrm{e}\mathrm{n_e}} \right) \tag{2.80}$$

The above times are evaluated in every simulation cell of coordinates $(i, j)$ and the mininum value of each is chosen, then the smallest value among the three values is chosen as follows:

$$\delta t = \min \left( \mathrm{A_c}\delta \mathrm{t_C}, \mathrm{A_I}\delta \mathrm{t_I}, \mathrm{A_D}\delta \mathrm{t_D} \right) \tag{2.81}$$

where $A_c = 0.5$, $A_I = 0.05$, and $A_D = 0.5$, respectively.

Note that if one considers the motion and diffusion of the ions, the FCT needs to be applied to the drift-diffusion equations of the ions as well.

### 2.3.10 Optical emission model

We apply a similar procedure as in equations (2.2) and (2.3) to solve the equation (2.8). Nevertheless, negative values of the density of the excited species $n_k$ could

appear if the time step of simulation $\delta t$ is larger than the lifetime $\tau_k$. In this case, we use another time step $\delta t^{'} = \frac{\tau_{C^3\Pi_u}}{10}$ to solve the equation (2.8) within every interval of simulation time step $\delta t$.

In order to obtain a projected image along the x-axis in units of Rayleighs (see Figure 2.11) the integral of the equation (2.9) is calculated as follows:

One has $l^2 + y^2 = r^2$ and $dl = \frac{r}{\sqrt{r^2-y^2}}dr$, thus the equation (2.9) becomes:

$$I_k = 2\times10^{-6}\int_{l=0}^{l} A_k n_k dl = 2\times10^{-6}\int_{r=y_{j=j_0}}^{r=y_{j=N_r}} A_k n_k \frac{r}{\sqrt{r^2-y^2}}dr \simeq 2\times10^{-6}A_k \sum_{m=j_0}^{m=N_r} n_k \frac{r_m}{\sqrt{r_m^2-y_{j_0}^2}}\Delta r \tag{2.82}$$

where the total line of sight $L = 2l$, and when $y = r$, $I_k \simeq A_k n_k \Delta r$, and when $y = 0$, $I_k \simeq \sum_{j=1}^{j=N_r} A_k n_k \Delta r$.

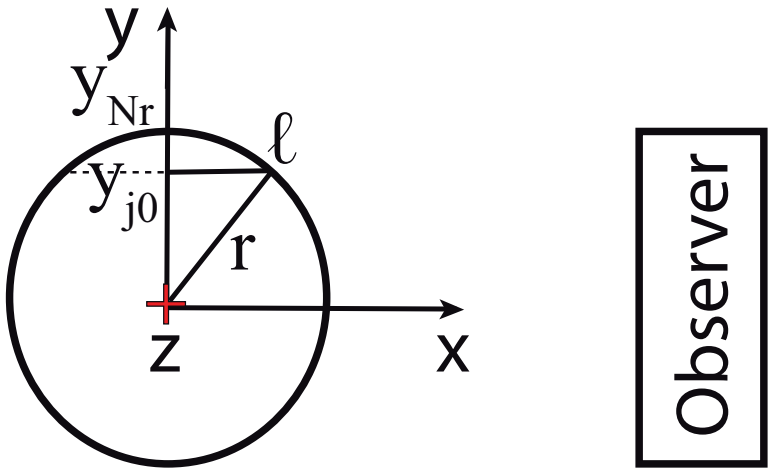


Figure 2.11 – Geometrical view of the line of sight. The circle represents a section of streamer and $z$ is the axis of symmetry.

### 2.3.11 Streamer fluid model algorithm

In summary the streamer model is organized as follows:

1. Set initial conditions: $n_e = n_{e_0} \exp^{-(z-z_0)^2/\sigma_z^2} \exp^{-r^2/\sigma_r^2}$, $n_p = n_e$, $n_n = 0$
2. Calculate the density of charge $\rho = (n_p - n_n - n_e)$
3. Calculate potential $\phi$ and electric field $E$

4. Calculate the transport parameters ($\nu_i, \nu_{2a}, \nu_{3a}, D_\mathrm{e}, \mu_\mathrm{e}, v_\mathrm{e}$) [*Morrow and Lowke*, 1997]
5. Calculate the time step $\delta t$
6. Calculate: $\bar{S}_\mathrm{e}$, $\bar{S}^+$, $\bar{S}^-$, $n_\mathrm{p}^{t+dt}$, $n_\mathrm{n}^{t+dt}$
7. Calculate the diffusive fluxes $\sum F^D$
8. Calculate the drift fluxes $\sum F$ with the FCT technique and the corrected density $n_{\mathrm{e}_\mathrm{corrected}}^{t+dt}$ (see Appendix A)
9. Calculate $n_\mathrm{e}^{t+dt}$ taking into account the source terms $\bar{S}$ and the diffusive fluxes
10. Calculate optical emissions
11. Go back to 2

## 2.4 Conclusions

The main conclusions of this chapter can be summarized as follows:

1. We have developed a plasma fluid streamer model that simulates different configurations: plane-to-plane parallel and point-to-plane electrodes using an open and Dirichlet boundary conditions for Poisson's equation.
2. We have developed a successive overrelaxation (SOR) Poisson's equation solver.
3. We have used an integral approach of photoionization combined with a linear interpolation technique, which is efficient for simulating single, double, and streamers head-on collisions.
4. We have developed a flux corrected transport (FCT) technique to constrain the numerical diffusion produced by the use of low order upwind scheme and the numerical dispersion produced by the use of high order finite differences scheme (or Lagrange-based scheme) and track accurately steep gradients in streamer discharge.
5. We have developed a model simulating the populations of the excited species during the propagation of the streamer and the associated optical emissions

# Chapter 3

# Increase of the electric field in head-on collisions between negative and positive streamers

**Abstract in French**

Une des problématiques actuelles concernant la physique des streamers porte sur la capacité de ces décharges à produire des rayons X. Il a en effet été démontré que les streamers obtenus dans les expériences de laboratoire à pression atmosphérique sont associés à des bouffées de rayons X. Dans la littérature récente, un des mécanismes envisagés est basé sur la collision entre streamers négatifs et positifs. Si ce mécanisme est viable, les sprites qui possèdent de nombreux streamers positifs et négatifs pourraient eux-mêmes produire des rayons X. Ce phénomène, qui n'a encore jamais été observé, est donc important pour la mission TARANIS qui pourra à la fois identifier les sprites et les photons de haute énergie, et plus généralement pour la physique des streamers et des évènements lumineux transitoires (TLEs). Dans ce chapitre, on expose et on étudie le processus de collision frontale entre décharges streamers via la simualtion numérique et on présente les résultats et leur analyse concernant l'augmentation du champ électrique lors d'un tel évènement et l'émission éventuelle

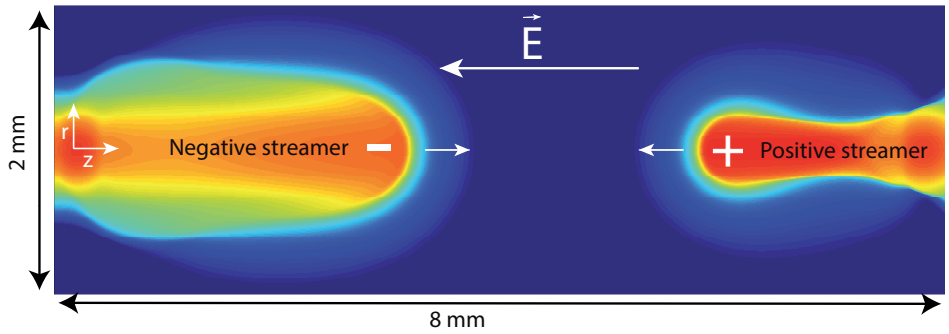


Figure 3.1 – Illustration of a head-on collision between a positive (right) and a negative streamer (left) moving toward each other under an external electric field $\vec{E}$.

associée des rayons X.

## 3.1 Introduction

Head-on collisions between negative and positive streamer discharges have recently been suggested to be responsible for the production of high electric fields leading to X-rays emissions [*Cooray et al.*, 2009; *Kochkin et al.*, 2012]. However, the estimation of the increase in the electric field during encounters of streamers with opposite polarities (see Figure 3.1) is a complicated problem. Indeed, an increase of the field beyond the conventional breakdown threshold would rapidly increase the electron density at the location of the encounter. In turn, one expects that the field would swiftly collapse due to the corresponding increase in the electron density. In this chapter, we use the streamer model developed in the previous chapter to simulate head-on collisions between negative and positive streamers, we investigate this non-linear problem and estimate upper limits on fluxes of high-energy electrons and photons possibly produced in this process using Monte Carlo simulations. Moreover, we quantify optical emissions produced during the process of streamer head-on collisions. In the framework of the TARANIS space mission, this work will also help the investigation of possible X-rays emissions from sprites when upper negative and lower positive sprite streamers encounters occur under strong quasi-electrostatic electric field.

## 3.2 Model formulation

In the present study, we use the streamer model presented in the previous chapter. The boundary conditions applied to Poisson's equation are the following: $\frac{\partial \phi}{\partial r}\Big|_{r=0}$ = 0, $\phi$(0 ≤ r ≤ 1.92 mm, z = 0) = 0, $\phi$(r, z = 8 mm) = U, and $\phi$(r = 1.92 mm, 0 ≤ z ≤ 8 mm) = U×(z/8 mm) where U = 32 kV or 48 kV and corresponds to amplitudes of homogeneous Laplacian fields $E_0$ = 40 kV/cm and $E_0$ = 60 kV/cm, respectively, between the plane electrodes. Positive and negative streamers are initiated on each side of the simulation domain by placing two Gaussians of neutral plasma with characteristic sizes $\sigma_z$ = 200 $\mu$m and $\sigma_r$ = 200 $\mu$m $n_{e_0} = 10^{20}$ m$^{-3}$ in the vicinity of each electrode.

We quantify the density of excited species of $N_2(B^3\Pi_g)$, $N_2(C^3\Pi_u)$, and $N_2^+(B^2\Sigma_u^+)$ associated with optical emissions of the first positive bands system of $N_2$ ($1PN_2$), the second positive bands system of $N_2$ ($2PN_2$), and the first negative bands system of $N_2^+$ ($1NN_2^+$), respectively.

## 3.3 Modeling results

In this work, we show simulation results performed at ground level air density $N$ = 2.688×10$^{25}$ m$^{-3}$ under strong externally applied homogeneous electric fields with a spatial resolution $\Delta z$ = 8 $\mu$m and $\Delta r$ = 8 $\mu$m in a simulation domain (1001×241) discretized over regular grid points.

### 3.3.1 Case $E_0$ = 40 kV/cm

As depicted in Figure 3.2(a) that shows the electric field along the $z$-axis, one sees the positive streamer forming and propagating leftward as the negative streamer initiates and propagates rightward [see online supporting information]. The electric field in both negative and positive streamers reaches a stable value, before starting to rise when streamers start influencing each other. The local electric field strongly increases at the moment of the encounter between both streamer heads. We can clearly see the collapse of the electric field just after reaching a maximum [*Ihaddadene and Celestin*, 2015, see supporting information] while a significant rise in the electron density is produced at the same location as shown in Figure 3.2(c).

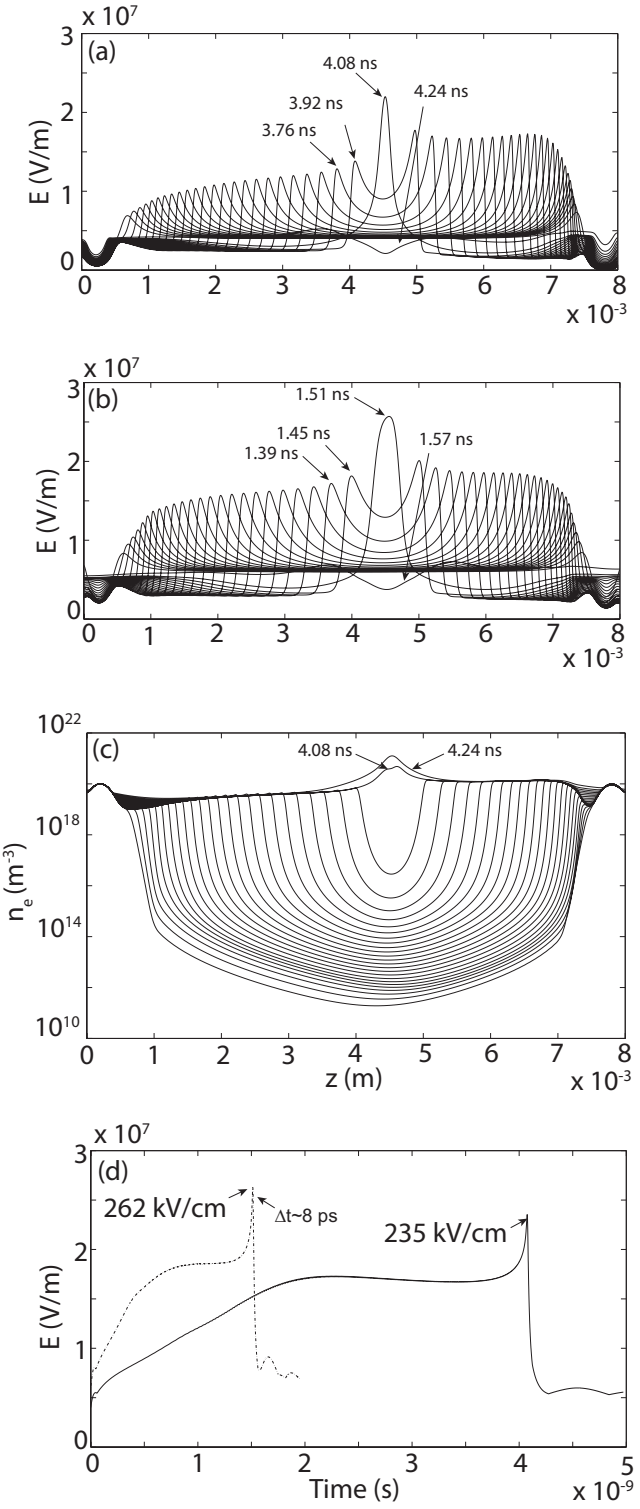


Figure 3.2 – (a) and (b) Profile of the electric field along the $z$-axis in the case $E_0 =$ 40 kV/cm and 60 kV/cm, respectively. (c) Profile of the electron density along the $z$-axis in the case $E_0 = 40$ kV/cm. (d) Evolution of the maximum electric field $E_{\max}$ as function of time. Solid and dashed line corresponds to the cases $E_0 = 40$ and 60 kV/cm, respectively. In panels (a) and (c), results are shown with a time step of 160 picoseconds. In panel (b), results are shown with a time step of 60 picoseconds.

Figure 3.2(d) (solid line) shows the behavior of the maximum electric field in the simulation domain as function of time for the case of an externally applied homogeneous electric field $E_0 = 40$ kV/cm. The maximum electric field in the simulation domain reaches 235 kV/cm, which is lower than the thermal runaway threshold as defined by the maximum electron friction force around ∼100 eV (∼260 kV/cm under ground level air density). Once the electric field in the streamer heads is stable, the average velocity before collision is estimated to be $\sim 10^6$ m/s.

### 3.3.2 Case $E_0 = 60$ kV/cm

Figure 3.2(d) (dashed line) shows the behavior of the maximum electric field in the simulation domain as function of time and (b) the electric field along the $z$-axis for the case $E_0 = 60$ kV/cm. We observe a similar behavior of the electric field as in the case $E_0 = 40$ kV/cm, however the maximum value reached is 262 kV/cm. After reaching a maximum of 262 kV/cm, the electric field collapses over a very short duration of ∼4 picoseconds. The total time over which the electric field is greater than 250 kV/cm is approximately ∼8 picoseconds. The maximum electric field reached is greater than that obtained in the situation where the homogeneous electric field is $E_0 = 40$ kV/cm and the average velocity of streamers before the encounter is greater as well ($\sim 3 \times 10^6$ m/s).

### 3.3.3 Estimate of the number of high-energy electrons and photons produced during the encounter of streamers with opposite polarities

Very high amplitudes of the electric field are obtained in both cases described above. In order to quantify the fluxes of high energy electrons and the corresponding bremsstrahlung photons produced during the streamers collision, we have used a Monte Carlo code that simulates the propagation of electrons in air with energies from sub-eV to MeVs under externally applied electric fields (see [*Celestin and Pasko*, 2011] for more details) in a two-step fashion. In the first step, we calculate the electric field during the streamer collision through our plasma fluid model as described above. In the second step, we follow the dynamics of test electrons initiated with an energy of 1 eV and distributed over space using our Monte Carlo code under

the electric fields varying in space and time that were obtained in the first step. The number of electrons needed in this configuration has proven computationally impractical on ∼100 processors to obtain an accurate estimate on the production of high energy electrons. For the sake of simplicity, we therefore estimate an upper limit of the flux of high energy electrons by using a time-varying homogeneous electric field equal to the maximum field obtained in our streamer simulation domain at each moment of time as shown in Figure 3.2(d). We emphasize that this method strongly overestimates the number and energy of electrons obtained since electric field gradients are neglected.

In the case of an applied field of $E_0 = 60$ kV/cm, at the moment of the collision the conduction current at the position of the peak electric field (see Figure 3.2(b)) reaches 20 A. For comparison, the conduction current evaluated locally in the positive streamer head when the electric field has reached a stable amplitude ($t \simeq 1$ ns, see Figure 3.2(c)) is ∼15 A, which is consistent with the amplitude of conduction current in a streamer head reported in the literature [e.g., *Liu*, 2010] considering that the external electric field applied in the present study is very strong (see Section 3.2). From this maximum current, one can directly estimate the total number of electrons passing through a surface perpendicular to the streamer axis per unit time during the streamer collision. Additionally, our Monte Carlo simulation results indicate that, in the case of $E_0 = 60$ kV/cm, the ratio between electrons with energies greater than 1 keV to the total number of electrons is lower than $1.5 \times 10^{-7}$. During the streamer collision, the strong increase in the electric field takes place over a duration shorter than 0.1 ns (see Figure 3.2(d)). Hence, one can estimate that during this time an upper limit of $20/q_e \times 1.5 \times 10^{-7} \times 0.1 \times 10^{-9} \simeq 2000$ electrons with energy greater than 1 keV could be produced.

### 3.3.4 Associated optical emissions

Figure 3.3(a)-(c) shows the associated optical emissions for $1PN_2$, $2PN_2$, and $1NN_2^+$ band systems [see online supporting information]. The maximum peaks of the density of the excited species and corresponding optical emissions are obtained after the maximum electric field was reached. In Figure 3.3, the results correspond to a time ∼30 picoseconds after the collision. We clearly see a luminosity increases

in the zone of the collision, which could be used as a signature of head-on encounters between positive and negative streamers.

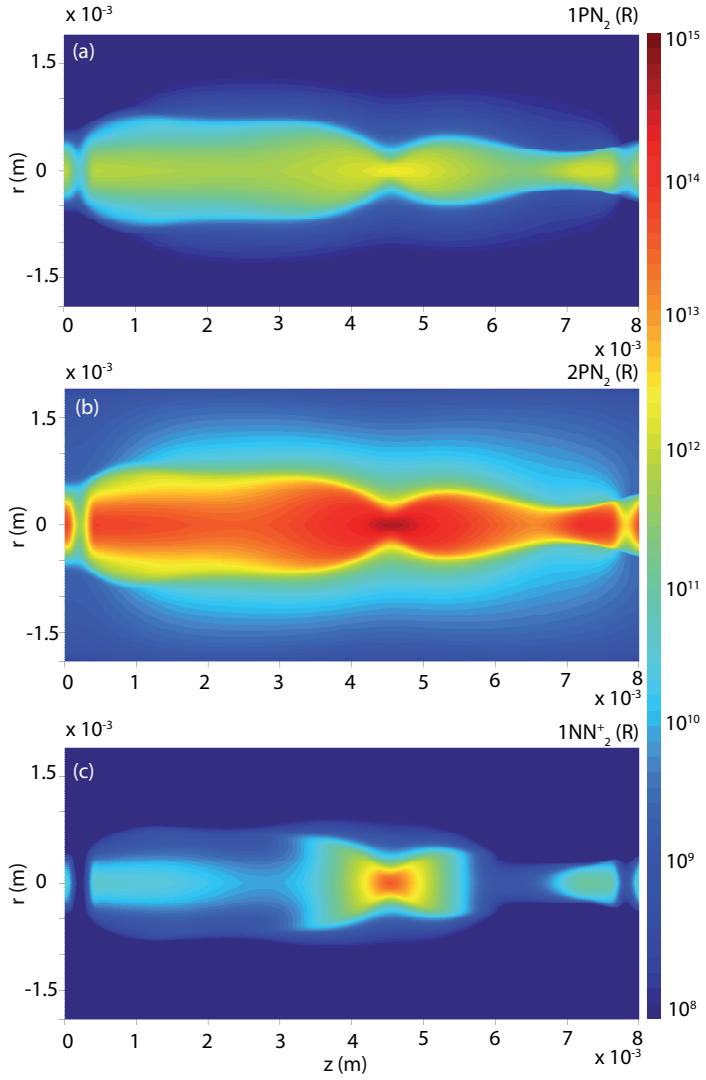


Figure 3.3 – (a)-(c) Associated optical emissions $1PN_2$, $2PN_2$, and $1NN_2^+$ 30 picoseconds after the head-on collision in the case of $E_0 = 40$ kV/cm.

## 3.4 Discussion

A very high maximum electric field of 262 kV/cm has been obtained locally during the head-on collision of negative and positive streamers propagating under a homogeneous electric field of 60 kV/cm. After a series of tests performed using a Monte Carlo model in which we have introduced the electric field obtained in

our streamer simulations, we have found that only a maximum of 2000 electrons with energy >1 keV could be produced by the encounter of streamers with opposite polarities studied in this work due to the rapid collapse of the strong field produced during the streamer collision (see Figure 3.2(d)). This estimate is done in the case of $E_0 = 60$ kV/cm and would be lower in the case of a weaker applied field since the resulting maximum field reached during the streamers collision would be weaker as well (see Figure 3.2(d)). In order to estimate the number of bremsstrahlung X-rays produced by these electrons, one can use the the Bethe-Heitler differential cross section [e.g. *Lehtinen*, 2000, pp. 45-49]. We find that the frequency of X-ray production with energy greater than 1 keV by electrons with energy of a few keVs in air at ground level is on the order of $\sim 10^5$ s$^{-1}$. For comparison, using the same cross section and air density, an electron with an energy of 1 MeV is associated with an X-ray (>1 keV) production frequency of $\sim 6 \times 10^6$ s$^{-1}$. In our simulation results, electrons with energy greater than 1 keV are only present for a very short time on the order of a few picoseconds. Assuming that these electrons could be present over a timescale corresponding to the timescale of the whole increase of the electric field ($\sim$0.1 ns), one finds that only $10^5 \times 2000 \times 0.1 \times 10^{-9} \simeq 0.02$ X-rays with energy greater than 1 keV would be produced per streamers encounter.

If one considers that, once produced, energetic electrons could still accelerate in the electrode gap [*Cooray et al.*, 2009] a longer X-ray emission timescale should be considered. Experiments of spark discharges producing X-rays usually involve electrode gaps of $\sim$1 m [e.g. *Dwyer et al.*, 2008; *Kochkin et al.*, 2012]. An electron with an energy of 1 keV has a velocity of $\sim 2 \times 10^7$ m/s, corresponding to a propagation lasting 50 ns over 1 m. Hence, one estimates an upper limit of 10 X-rays with energy >1 keV produced by the propagation of such 2000 electrons over the whole electrode gap. We emphasize that physical parameters have been maximized to obtain this upper limit. Given the very low number of X-rays obtained through the mechanism of encounters of streamers with opposite polarities, it is unlikely that these photons could be detected.

The electric field at the streamer head is partly controlled by the externally applied Laplacian electric field. The reason why we have used very strong externally applied ambient fields of 40 and 60 kV/cm is to increase the electric field at the

heads of both streamers to maximize the probability of producing thermal runaway electrons. This had an impact on the velocity of streamers as well. As obvious in Figure 3.2(d), the collision corresponding to $E_0 = 60$ kV/cm occurred earlier in time than that of $E_0 = 40$ kV/cm. We emphasize that the homogeneous fields used in this work are much stronger than fields usually present in the middle of 1 meter spark gaps.

It is important to note that the significant amount of excited species produced during the head-on encounter of streamers and the associated optical emissions can be used as a signature to determine if a collision between streamers of opposite polarity actually took place.

The head-on collision patch of the optical emission is reminiscent of luminous patches observed in sprites and named sprite-beads [e.g., *Cummer et al.*, 2006; *Stenbaek-Nielsen and McHarg*, 2008; *Luque and Gordillo-Vasquesz*, 2011]. Note that *Cummer et al.* [2006] had already found out that collisions between downward streamers and adjacent streamer channels form long-lasting sprite beads. However, the duration of the luminous patch found in our simulations is too short to account for durations up to one second, even if scaled to high altitude. Indeed, we have performed similar simulations as those presented in the present work with an air density corresponding to 70 km altitude and found that the luminous patch lasts over a few microseconds for $2PN_2$ and $1NN_2^+$ and $\sim$10 microseconds for $1PN_2$. Nevertheless, other physical processes such as chemical reactions unaccounted for in the present study or long-lasting continuing current of the sprite producing lightning discharge may have a significant effect on the overall duration of these luminous patches and sprite produced by inhomogeneities placed at different altitudes may encounter and produce associated optical patches similar to those reported in the present study.

Figure 3.4 shows the electric field of a head-on collision between a negative and a positive streamer, at 70 km altitude, propagating under a strong homogeneous electric field of $40\times\frac{N_{70}}{N_0}$ kV/cm (which is higher than the required field for the production of sprite streamers $\sim 0.9E_k$ [e.g., *Hu et al.*, 2007; *Li et al.*, 2008]) and the $1NN_2^+$ distinguishable optical luminous patch produced during the collision. Hence, the condition applied in this simulation is extreme and shows that sprite head-

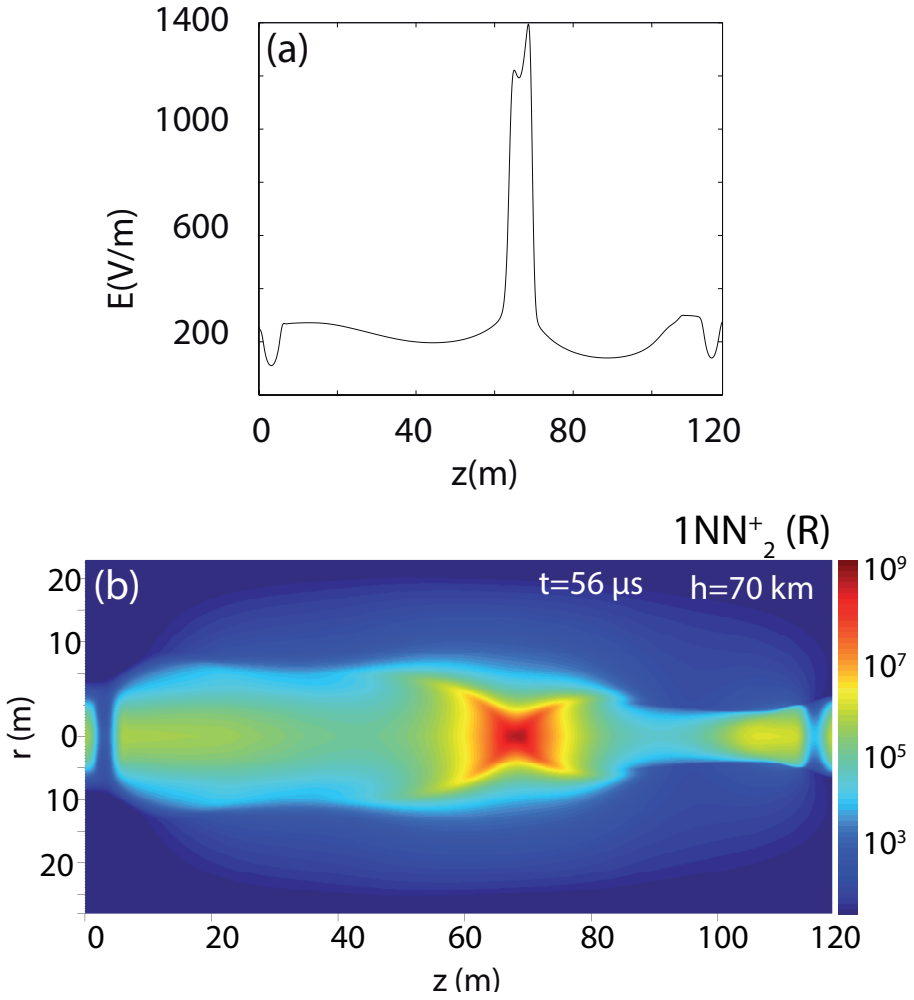


Figure 3.4 – (a)-(b) Simulation results of the electric field along the axis of symmetry and $1NN_2^+$ optical luminous patch produced during a head-on collision between a negative and a positive streamer at 70 km altitude under an homogeneous electric field $40\times\frac{N_{70}}{N_0}$ kV/cm (scaled ambient conditions as compared with the results presented in Figure 3.3 (a)) .

collision would hardly reach an electric field 1400 V/m equivalent to 200 kV/cm at ground level, which demonstrates that this process is unlikely to produce energetic electrons and the associated X-rays. Simple scaling of our results obtained at ground level leads to an emission of ∼0.02 X-rays per streamer collision altitude. It is doubtful that satellite sensors could detect such a low X-ray emission.

## 3.5 Conclusions

The main conclusions of this work can be summarized as follows:

1. We have simulated the head-on collision between positive and negative streamers and have shown that this process is not likely to produce significant number of thermal runaway electrons with energy >1 keV and the corresponding X-rays.
2. Despite the very high peak electric field obtained during the streamer collision, the corresponding rapid collapse of the electric field over a few picoseconds at ground level or a few nanoseconds at sprites altitudes, due to the large increase of the conductivity at the same location prevents efficient production of thermal runaway electrons.
3. We have quantified the amount of excited species and the associated optical emissions. We show that the occurrence of the streamer collision is followed by a peak of optical emissions associated with $1PN_2$, $2PN_2$, and $1NN_2^+$ band systems (luminous patch). This may be used as a signature of streamer head-on collisions and corresponding experimental verification of the capability of streamer collisions to produce X-rays.
4. We have found that the head-on collision of sprite streamers hardly reaches electric fields allowing the production of energetic electrons and the associated X-rays.

# Chapter 4

# Determination of sprite streamers altitude using $N_2$ spectroscopic analysis

**Abstract in french**

L'étude des TLEs (Transient Luminous Events) est l'objectif principal de la mission TARANIS qui les observera depuis le nadir. Bien que cette géométrie d'observation soit particulièrement bien adaptée à l'étude des TLEs, elle ne permet pas d'obtenir une bonne résolution en altitude des phénomènes. En outre, les photomètres (instrument MCP) fourniront une information spectroscopique intégrée spatialement. Pour surmonter cette difficulté, on a développé une méthode spectrophotométrique qui permettra d'obtenir une information sur l'altitude des streamers dans les TLEs en fonction du temps à partir des données de MCP. Cette méthode est basée sur l'analyse des ratios de différents systèmes de bandes associés à la molécule d'azote $N_2$: Lyman-Birge-Hopfield (LBH), le premier système positif ($1PN_2$), le deuxième système positif ($2PN_2$) ainsi que le premier système négatif ($1NN_2^+$) associé à l'ion $N_2^+$. Ces travaux vont donc augmenter le retour scientifique de TARANIS et des autres missions spatiales, comme par exemple GLIMS (JAXA) et ASIM (ESA). Dans ce chapitre, on expose en détail cette méthode, et on explique comment l'utiliser.

## 4.1 Introduction

One of the ways used to explore the physical properties of sprites is the spectroscopic diagnostic of their optical emissions, specifically in the following bands systems of $N_2$: the Lyman-Birge-Hopfield (LBH) ($a^1\Pi_g \rightarrow X^1\Sigma_g^+$) (∼100-260 nm), the first positive $1PN_2$ ($B^3\Pi_g \rightarrow A^3\Sigma_u^+$) (∼650-1070 nm), the second positive $2PN_2$ ($C^3\Pi_u \rightarrow B^3\Pi_g$) (∼330-450 nm), as well as the first negative bands systems of $N_2^+$ ($1NN_2^+$) ($B^2\Sigma_u^+ \rightarrow X^2\Sigma_g^+$) (∼ 390-430 nm). The experiment LSO (CEA, CNES), GLIMS (JAXA), and the future mission ASIM (ESA) are dedicated to the observation of TLEs from the International Space Station (ISS). The satellite mission Tatiana-2 (MSU) observed TLEs from a sun-synchronous orbit at 820-850 km altitude. The future satellite mission TARANIS (CNES), will observe TLEs from a sun-synchronous orbit at an altitude of ∼700 km. All the abovementioned space missions have adopted strategies based on nadir observation of TLEs. Observation from a nadir-viewing geometry is indeed especially interesting as it reduces the distance between the observation point and the event, and hence minimizes atmospheric absorption and maximizes the chance of observing TLEs and their associated phenomena, such as electromagnetic radiation or possible high-energy emissions. However, in this observation geometry, the vertical dimension is poorly resolved, and so are the speeds of sprite substructures.

In this chapter, we investigate a spectrophotometric method [*Ihaddadene and Celestin*, 2016] to trace back the altitude of sprite streamers using optical emissions that will be detected by ASIM and TARANIS, and that were detected by GLIMS. We show that, combining observations with streamer modeling results, it is possible to obtain information about the production altitude of sprite streamers.

## 4.2 Model Formulation

### 4.2.1 Streamer model

We use the streamer model presented in the Chapter Streamer Model Formulation. In order to simulate streamer propagation in weak electric field lower than the conventional breakdown field $E_k = 29 \times \frac{N}{N_0}$ kV/cm, defined by the equality of the ionization and the two body dissociative attachment frequencies in air [e.g., *Morrow*

*and Lowke*, 1997], where $N_0 = 2.688 \times 10^{25}$ m$^{-3}$ is the air density at ground level and $N$ is the local air density, we use a sphere-to-plane electrode configuration [e.g., *Babaeva and Naidis*, 1996a,b] to initiate the streamer. A sphere of a radius $R_{\rm sph} = 10^{-3} \times \frac{N_0}{N}$ m is set to a potential $\phi_0 = 0$ and 4.8 kV and placed in a weak uniform electric field $E_0 = 28 \times \frac{N}{N_0}$ kV/cm and $E_0 = 12 \times \frac{N}{N_0}$ kV/cm, respectively, in order to obtain a maximum amplitude of the electric field of $3E_k$ at the surface of the sphere [e.g., *Liu et al.*, 2006, 2009a]. In this study, we consider $E_0 = 28 \times \frac{N}{N_0}$ kV/cm and $E_0 = 12 \times \frac{N}{N_0}$ kV/cm as reasonable upper and lower limits of ambient electric fields necessary for the propagation of streamers in the early stage of sprites. This is in general agreement with observation-based estimates of *Hu et al.* [2007], *Li et al.* [2008], *Liu et al.* [2009b], and *Qin et al.* [2012]. Note that streamers are capable of propagating in electric field as low as $E_0 = 5 \times \frac{N}{N_0}$ kV/cm [e.g. *Qin and Pasko*, 2014, and references therein].

Downward propagating positive streamers are initiated by placing a Gaussian of neutral plasma with characteristic sizes $\sigma_z = 10^{-4} \times \frac{N_0}{N}$ m and $\sigma_r = 10^{-4} \times \frac{N_0}{N}$ m and $n_{e_0} = 10^{18} \times \frac{N^2}{N_0^2}$ m$^{-3}$ in the vicinity of the sphere electrode. For more information about the scaling of physical parameters in this configuration see [*Liu and Pasko*, 2006]. The simulation domain is discretized over 1001×241 regular grid points with the spatial resolution defined by $\Delta z = 8 \times 10^{-6} \times \frac{N_0}{N}$ m and $\Delta r = 8 \times 10^{-6} \times \frac{N_0}{N}$ m.

### 4.2.2 Optical emissions model

We use the optical emission model described in the Chapter Model Formulation. Along with the streamer propagation, we quantify the densities of excited species $N_2(a^1\Pi_g)$, $N_2(B^3\Pi_g)$, $N_2(C^3\Pi_u)$, and $N_2^+(B^2\Sigma_u^+)$ associated with optical emissions of the Lyman-Birge-Hopfield bands system of $N_2$ (LBH) ($a^1\Pi_g \rightarrow X^1\Sigma_g^+$), the first positive bands systems of $N_2$ (1PN$_2$) ($B^3\Pi_g \rightarrow A^3\Sigma_u^+$), the second positive bands system of $N_2$ (2PN$_2$) ($C^3\Pi_u \rightarrow B^3\Pi_g$), and the first negative bands systems of $N_2^+$ (1NN$_2^+$) ($B^2\Sigma_u^+ \rightarrow X^2\Sigma_g^+$), respectively. In this work, we only take into account the cascading from $N_2(C^3\Pi_u)$ to $N_2(B^3\Pi_g)$.

### 4.2.3 Estimation of the streamer peak electric field using optical emissions

The study of the $N_2$ and $N_2^+$ optical emissions produced by sprite streamers is useful to estimate the peak electric field in streamer heads, because the energy of the electrons depends on the amplitude of this field and the excited species responsible for the production of different bands systems are produced through collisions between electrons and $N_2$ molecules in the ground state and correspond to different energy thresholds. In this subsection, we describe how we proceed to infer the peak electric field.

We simulate downward propagating positive streamers in uniform electric fields $E_0 = 12 \times \frac{N}{N_0}$ and $28 \times \frac{N}{N_0}$ kV/cm at given altitudes $h$ = 50, 60, 70, 80, and 90 km. Using equations (2.8) and (2.9), we quantify the excited species and the associated optical emissions (see Figure 4.1). The whole volume of the streamer emits photons, mainly in the head region [e.g., *Bonaventura et al.*, 2011], and hence we integrate each band system photon flux over the whole body of the streamer including the head as $\tilde{I}_k = \int I_k ds$, where $ds = \Delta z \times \Delta r$ is an elementary surface. We then calculate the associated ratios $R_{kk'} = \frac{\tilde{I}_k}{\tilde{I}_{k'}}$.

Assuming that the steady state is reached (the production and loss rates of excited species are equal) under a given electric field and using equation (2.8) as described in [*Celestin and Pasko*, 2010], one obtains the following photon flux ratio, which is function of the electric field through $\nu_k$ and $\nu_{k'}$:

$$R_{kk'} = \frac{\nu_k}{\nu_{k'}} \frac{A_k}{A_{k'}} \frac{\tau_k}{\tau_{k'}} \tag{4.1}$$

where we neglected the cascading from higher states. In the case of $N_2(B^3\Pi_g)$, one needs to take into account the cascading from $N_2(C^3\Pi_u)$ to $N_2(B^3\Pi_g)$ and following the same procedure, one finds:

$$R_{k\mathrm{B^3\Pi_g}} = \frac{\nu_k}{\nu_{\mathrm{B^3\Pi_g}}} \frac{A_k}{A_{\mathrm{B^3\Pi_g}}} \frac{\tau_k}{\tau_{\mathrm{B^3\Pi_g}}} \frac{1}{\left(1 + \frac{\nu_{\mathrm{C^3\Pi_u}} A_{\mathrm{C^3\Pi_u}} \tau_{\mathrm{C^3\Pi_u}}}{\nu_{\mathrm{B^3\Pi_g}}}\right)} \tag{4.2}$$

As mentioned in [*Celestin and Pasko*, 2010], the steady state of excited species is not a necessary condition for equation (4.1) and (4.2) to be applicable, even though

equations (4.1) and (4.2) have been derived assuming steady state. In fact, it can be shown formally from equation (2.8) that if the streamer propagation is sufficiently stable over a timescale on the order of $\tau_k$, the equations (4.1) and (4.2) also apply in the case of non-steady state. Indeed, defining $N_k = \int n_k dV$, equation (2.8) leads to:

$$\frac{\partial N_k}{\partial t} = -\frac{N_k}{\tau_k} + \int \nu_k n_\mathrm{e} dV + \sum_m N_m A_m \tag{4.3}$$

Assuming that the streamer is sufficiently stable, i.e., its radius is approximately constant over a timescale $\tau_k$, that is $|\frac{\partial N_k}{\partial t}| \ll \frac{N_k}{\tau_k}$, one can neglect the left-hand side of equation (4.3), and therefore:

$$N_k = \tau_k \int \nu_k n_\mathrm{e} dV + \tau_k \sum_m N_m A_m \tag{4.4}$$

which leads to equations (4.1) and (4.2) for a given homogeneous electric field. However, although the homogeneous electric field assumption for steady state optical emissions is justified by the fact that the emission is confined in the streamer head (within a spatial shift mentioned in the Introduction), one might wonder whether this assumption would still be valid in the case of non-steady state emission that trails behind the streamer head. Equation (4.4) can be rewritten:

$$N_k = \tau_k \nu_k \int n^*_{\mathrm{e},\nu_\mathrm{k}} dV + \tau_k \sum_m N_m A_m \tag{4.5}$$

where $n^*_{\mathrm{e},\nu_\mathrm{k}}$ is an effective quantity defined by $\int \nu_k n_\mathrm{e} dV = \nu_k \int n^*_{\mathrm{e},\nu_\mathrm{k}} dV$. Since the excitation frequency strongly depends on the electric field one can consider that $\nu_k = \nu_k(E_h)$ and one notes $N^*_{\mathrm{e},\nu_\mathrm{k}} = \int n^*_{\mathrm{e},\nu_\mathrm{k}} dV$. Neglecting the cascading term in equation (4.5), one gets:

$$N_k = \tau_k \nu_k N^*_{\mathrm{e},\nu_\mathrm{k}} \tag{4.6}$$

and thus the ratio obtained in equation (4.1) if one assumes $\frac{N^*_{\mathrm{e},\nu_\mathrm{k}}}{N^*_{\mathrm{e},\nu_{\mathrm{k}'}}} = 1$, i.e., considering that the excitation taking place in the streamer head dominates over the excitation from other regions. It can be easily shown that equation (4.5) also results in equation (4.2) if the cascading effect is not neglected. In conclusion, the

steady/non-steady nature of optical emission does not affect the validity of the ratio found in equations (4.1) and (4.2) if the streamer can be considered as stable over a timescale $\tau_k$ and if most of the excitation is produced in the head. This point is clearly demonstrated by the simulation results of *Bonaventura et al.* [2011] for $2PN_2$ and $1NN_2^+$.

Using equations (4.1) and (4.2), one can estimate the peak electric field $E_e$ for every simulation-based ratio $R_{kk'}$ found if steady state is reached for excited species $k$ and $k^{'}$. From the estimated field $E_e$ and the peak field in the simulation $E_h$, a correction factor due mostly to the spatial shift between maxima of optical emissions and the peak electric field is calculated as $\gamma_{kk'}^{h,E_0} = \frac{E_h}{E_e}$ [*Celestin and Pasko*, 2010]. The correction factors calculated in the present work are shown in Tables 4.1 and 4.2.

Table 4.1 – Correction factors calculated at different altitudes under $E_0 = 12 \times \frac{N}{N_0}$ kV/cm using equations (4.1) and (4.2).

| Altitude (km) | 50 | 60 | 70 | 80 | 90 |
|---|---|---|---|---|---|
| $\frac{2PN_2}{1PN_2}$ | 1.57 | 1.60 | 1.68 | 1.62 | 1.64 |
| $\frac{LBH}{1PN_2}$ | 2.06 | 2.09 | 2.05 | 2.02 | 1.79 |
| $\frac{2PN_2}{1NN_2^+}$ | 1.40 | 1.41 | 1.40 | 1.41 | 1.41 |
| $\frac{LBH}{1NN_2^+}$ | 1.36 | 1.36 | 1.38 | 1.38 | 1.41 |

Table 4.2 – Correction factors calculated at different altitudes under $E_0 = 28 \times \frac{N}{N_0}$ kV/cm using equations (4.1) and (4.2).

| Altitude (km) | 50 | 60 | 70 | 80 | 90 |
|---|---|---|---|---|---|
| $\frac{2PN_2}{1PN_2}$ | 1.49 | 1.65 | 2.03 | 2.24 | 2.39 |
| $\frac{LBH}{1PN_2}$ | 5.86 | 6.41 | 6.45 | 4.81 | 2.73 |
| $\frac{2PN_2}{1NN_2^+}$ | 1.61 | 1.61 | 1.60 | 1.61 | 1.62 |
| $\frac{LBH}{1NN_2^+}$ | 1.34 | 1.35 | 1.40 | 1.49 | 1.62 |

However, in general, a sprite streamer can be considered as expanding exponentially in time [e.g., *Liu et al.*, 2009b]. The rate of expansion $\nu_e$ is a strong function of the ambient electric field [*Kosar et al.*, 2012]. In fact, equation (4.3) can be rewritten in the form:

$$\frac{\partial N_k}{\partial t} = -\frac{N_k}{\tau_k} + \nu_k N^*_{e,\nu_k} + \sum_m A_m N_m \tag{4.7}$$

As we mentioned just above, one considers that $N_k = N_{k,0} \exp(\nu_e t)$, and equa-

tion (4.7) leads to:

$$N_k = \frac{\nu_k \tau_k N^*_{\mathrm{e},\nu_\mathrm{k}}}{(1+\nu_\mathrm{e}\tau_k)} \tag{4.8}$$

if one neglects the cascading effect, and otherwise:

$$N_k = \frac{\nu_k \tau_k}{(1+\nu_\mathrm{e}\tau_k)} \left( N^*_{\mathrm{e},\nu_\mathrm{k}} + \frac{1}{\nu_k} \frac{\sum_m \nu_m A_m \tau_m N^*_{\mathrm{e},\nu_\mathrm{m}}}{(1+\nu_\mathrm{e}\tau_m)} \right) \tag{4.9}$$

Hence, for significantly quick streamer expansion ($\nu_\mathrm{e} \sim \frac{1}{\tau_k}$), without taking into account the cascading effect, one obtains:

$$R_{kk'} = \frac{\nu_k}{\nu_{k'}} \frac{A_k}{A_{k'}} \frac{\tau_k}{\tau_{k'}} \left( \frac{1+\nu_\mathrm{e}\tau_{k'}}{1+\nu_\mathrm{e}\tau_k} \right) \frac{N^*_{\mathrm{e},\nu_\mathrm{k}}}{N^*_{\mathrm{e},\nu_{\mathrm{k}'}}} \tag{4.10}$$

and taking into account the cascading effect:

$$R_{k\mathrm{B}^3\Pi_\mathrm{g}} = \frac{\nu_k}{\nu_{\mathrm{B}^3\Pi_\mathrm{g}}} \frac{A_k}{A_{\mathrm{B}^3\Pi_\mathrm{g}}} \frac{\tau_k}{\tau_{\mathrm{B}^3\Pi_\mathrm{g}}} \frac{\left( \frac{1+\nu_\mathrm{e}\tau_{\mathrm{B}^3\Pi_\mathrm{g}}}{1+\nu_\mathrm{e}\tau_k} \right)}{\left[ \frac{N^*_{\mathrm{e},\nu_{\mathrm{B}^3\Pi_\mathrm{g}}}}{N^*_{\mathrm{e},\nu_\mathrm{k}}} + \frac{\nu_{\mathrm{C}^3\Pi_\mathrm{u}} A_{\mathrm{C}^3\Pi_\mathrm{u}} \tau_{\mathrm{C}^3\Pi_\mathrm{u}}}{\nu_{\mathrm{B}^3\Pi_\mathrm{g}} (1+\nu_\mathrm{e}\tau_{\mathrm{C}^3\Pi_\mathrm{u}} \frac{N^*_{\mathrm{e},\nu_{\mathrm{C}^3\Pi_\mathrm{u}}}}{N^*_{\mathrm{e},\nu_\mathrm{k}}})} \right]} \tag{4.11}$$

For all the cases used in the present work, we have verified that the population of $\mathrm{N}_2(C^3\Pi_u)$ is in steady state and $\nu_\mathrm{e}\tau_{\mathrm{C}^3\Pi_\mathrm{u}} \ll 1$. The excitation frequencies $\nu_k$ and their dependence on the electric field are computed based on [*Moss et al.*, 2006]. Using equations (4.10) and (4.11) and assuming $\frac{N^*_{\mathrm{e},\nu_\mathrm{k}}}{N^*_{\mathrm{e},\nu_{\mathrm{k}'}}} = 1$, i.e, considering that the excitation taking place in the streamer head dominates over the excitation from other regions, one can estimate the peak electric field $E_e$ for every simulation-based ratio $R_{kk'}$ found as described above even in the case of non-steady state of excited species accompanied by rapid expansion of the streamer ($\nu_e \sim \frac{1}{\tau_k}$). Precisely, because in reality the ratios $\frac{N^*_{\mathrm{e},\nu_\mathrm{k}}}{N^*_{\mathrm{e},\nu_{\mathrm{k}'}}} \neq 1$, correction factors need to be quantified using modeling results and taken into account in photometric-based observational studies to correct the estimated value of the peak electric field. The expansion frequency $\nu_\mathrm{e}$ and the various correction factors calculated in the present work for different altitudes and under different uniform electric fields $E_0 = 12 \times \frac{N}{N_0}$ and 28 $\times \frac{N}{N_0}$ kV/cm are shown in Tables 4.3, 4.4 and 4.5.

Table 4.3 – The expansion frequency $\nu_e$ ($s^{-1}$) calculated at different altitudes.

| Altitude (km) | 50 | 60 | 70 | 80 | 90 |
|---|---|---|---|---|---|
| $E_0 = 12 \times \frac{N}{N_0}$ kV/cm | 1.2 $10^5$ | 3.5 $10^4$ | 1.0 $10^4$ | 2.3 $10^3$ | 3.5 $10^2$ |
| $E_0 = 28 \times \frac{N}{N_0}$ kV/cm | 3.96 $10^5$ | 1.2 $10^5$ | 3.4 $10^4$ | 7.75 $10^3$ | 1.2 $10^3$ |

Table 4.4 – Correction factors calculated at different altitudes under $E_0 = 12 \times \frac{N}{N_0}$ kV/cm using equations (4.10) and (4.11).

| Altitude (km) | 50 | 60 | 70 | 80 | 90 |
|---|---|---|---|---|---|
| $\frac{2PN_2}{1PN_2}$ | 1.88 | 1.84 | 1.81 | 1.66 | 1.66 |
| $\frac{LBH}{1PN_2}$ | 1.39 | 1.39 | 1.39 | 1.58 | 1.69 |
| $\frac{LBH}{1NN_2^+}$ | 1.48 | 1.47 | 1.47 | 1.43 | 1.42 |

Table 4.5 – Correction factors calculated at different altitudes under $E_0 = 28 \times \frac{N}{N_0}$ kV/cm using equations (4.10) and (4.11).

| Altitude (km) | 50 | 60 | 70 | 80 | 90 |
|---|---|---|---|---|---|
| $\frac{2PN_2}{1PN_2}$ | 2.65 | 2.63 | 2.61 | 2.43 | 2.44 |
| $\frac{LBH}{1PN_2}$ | 1.95 | 1.93 | 1.94 | 2.03 | 2.21 |
| $\frac{LBH}{1NN_2^+}$ | 1.72 | 1.71 | 1.71 | 1.67 | 1.67 |

## 4.3 Results

### 4.3.1 Streamer modeling

We conducted simulations at altitudes $h$ = 50, 60, 70, 80, and 90 km under $E_0$ = 12 and 28 $\times \frac{N}{N_0}$ kV/cm, which represents 10 simulations in total.

As an example, we show the results for a positive downward propagating sprite streamer in uniform electric field $E_0 = 12 \times \frac{N}{N_0}$ kV/cm, initiated at 70 km altitude in Figures 4.1 and 4.2. Figure 4.1(a)-(b) shows the cross-sectional views of the electron density and the electric field. Cross-sectional views of photon fluxes from LBH, $1PN_2$, $2PN_2$, and $1NN_2^+$ bands systems at time $t$ = 0.27 ms are shown in Figure 4.1(c)-(f). The quenching altitude is defined so that above this altitude, the radiative de-excitation of given $N_2$ or $N_2^+$ excited state $k$ dominates the collisional one. Based on the quenching coefficients that we have applied to quantify the densities of $N_2$ and $N_2^+$ excited species and their associated bands systems, we have deduced the quenching altitudes shown in Table 2.1.

Figure 4.2(a)-(b) shows the electron density and electric field profiles along the

axis of the streamer every 0.054 ms. Figure 4.2(c) shows the optical emission from bands systems profiles LBH, $1PN_2$, $2PN_2$, and $1NN_2^+$, along the axis of the streamer at $t = 0.27$ ms in terms of photon flux.

### 4.3.2 Estimation of the altitude of the sprite streamers using optical emissions

We first define an array of electric field ranging from 0 to 600 $\times\frac{N}{N_0}$ kV/cm representing actual peak electric fields in the streamer head and then we compute the ratio associated with each value of the electric field $E_e = \frac{E_h}{\gamma_{kk'}^{h,E_0}}$. Figures 4.3(a) and (b) show two parametric representations of selected optical emission ratios through the implicit parameter $E_e$. The upper and lower curves that delimit shaded areas in Figure 4.3 correspond to background electric fields $E_0 = 12 \times\frac{N}{N_0}$ and 28 $\times\frac{N}{N_0}$ kV/cm, respectively at given altitudes. Between two shaded areas the altitude is $h_1 < h < h_2$ where $h_2$-$h_1 = 10$ km. For the sake of illustration, we show how the results of our simulations are located in this parametric representation (Figure 4.3). Red and yellow marks correspond to cases of ambient electric field amplitudes $E_0 =$ 12 $\times\frac{N}{N_0}$ and 28 $\times\frac{N}{N_0}$ kV/cm, respectively. Since the correction factors $\gamma_{kk'}^{h,E_0}$ are obtained from the same simulations, one sees that the obtained intensity ratios fall exactly on the estimated lines. One also sees that a descending streamer would take a specific path in the parametric representation illustrated in Figure 4.3(a) and (b). This particular behavior can be used to infer physical properties of sprite streamers from photometric observations such as the electric field and mean velocity.

The mark X located by coordinates $(R_{kk'}, R_{k''k'})$ within a shaded area illustrates a situation where the peak electric field $E_h$ would be such that: $E_h^{E_0=12\text{kV/cm}} < E_h < E_h^{E_0=28\text{kV/cm}}$, where $E_h^{E_0=12\text{kV/cm}}$ and $E_h^{E_0=28\text{kV/cm}}$ are shown in Table 4.6.

Table 4.6 – Electric field at the head of the positive streamer $E_h$ (V/m) at different altitudes under different ambient electric fields $E_0$.

| Altitude (km) | 50 | 60 | 70 | 80 | 90 |
|---|---|---|---|---|---|
| $E_0$=12 $\times\frac{N}{N_0}$ kV/cm | 8735 | 2597 | 745.9 | 165.9 | 26.4 |
| $E_0$=28 $\times\frac{N}{N_0}$ kV/cm | 1.1 $10^4$ | 3269 | 940.5 | 209.1 | 33.21 |

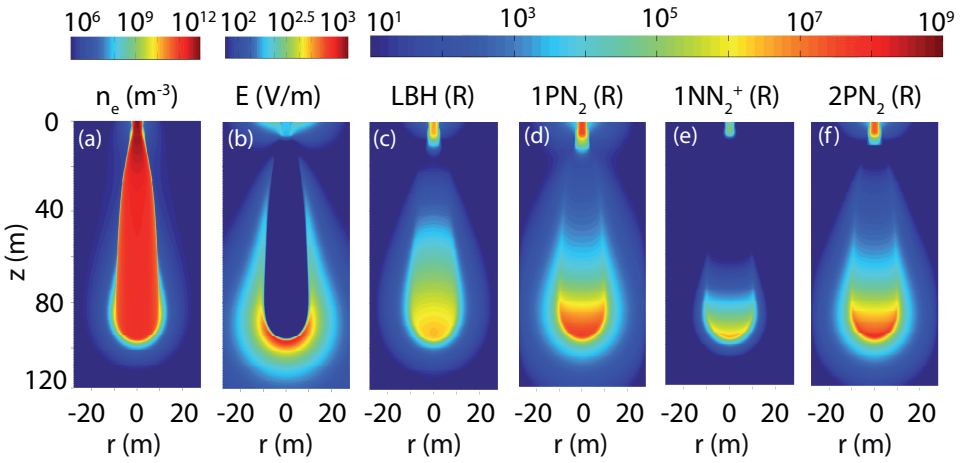


Figure 4.1 – (a)-(b) Electron density and electric field cross-sectional views. (c)-(f) Cross-sectional views of optical emission from LBH, $1PN_2$, $1NN_2^+$, and $2PN_2$ bands systems, respectively, in units of Rayleighs (R). The ambient field is $E_0 = 12 \times \frac{N}{N_0}$ kV/cm, the altitude is $h = 70$ km, and the time is $t = 0.27$ ms.

## 4.4 Discussion

For a given ambient electric field $E_0$, one sees in Figure 4.3 that curves corresponding to different altitudes are not overlapped. This is due to the different amounts of quenching that excited states are subjected to at different altitudes. Indeed, the excited states $N_2(a^1\Pi_g)$ and $N_2(B^3\Pi_g)$, that are responsible for LBH and $1PN_2$ bands systems, respectively, have quenching altitudes of 77 km and 67 km, while $N_2(C^3\Pi_u)$ and $N_2^+(B^2\Sigma_u^+)$, that are responsible for the $2PN_2$ and $1NN_2^+$ bands systems, respectively, can be considered as not strongly affected by quenching over the altitude range covered by sprites (see Table 2.1). This discrimination in altitude, which exists over a large range of electric fields in the streamer head for the selected ratios in Figure 4.3 is of first interest to determine the altitude of sprite streamers at various moments of time from photometric measurements. It especially applies to satellite observations in a nadir-viewing geometry. It is important to note that the quenching coefficients for $N_2(a^1\Pi_g)$ are not well known [e.g., *Liu and Pasko*, 2005]. However, one also notes that *Liu et al.* [2009a] obtained a satisfying agreement with observational results from the instrument ISUAL (Imager of Sprites and Upper Atmospheric Lightning) on the FORMOSAT-2 Taiwanese satellite using the quenching coefficients reported in Table 2.1 concerning $N_2(a^1\Pi_g)$.

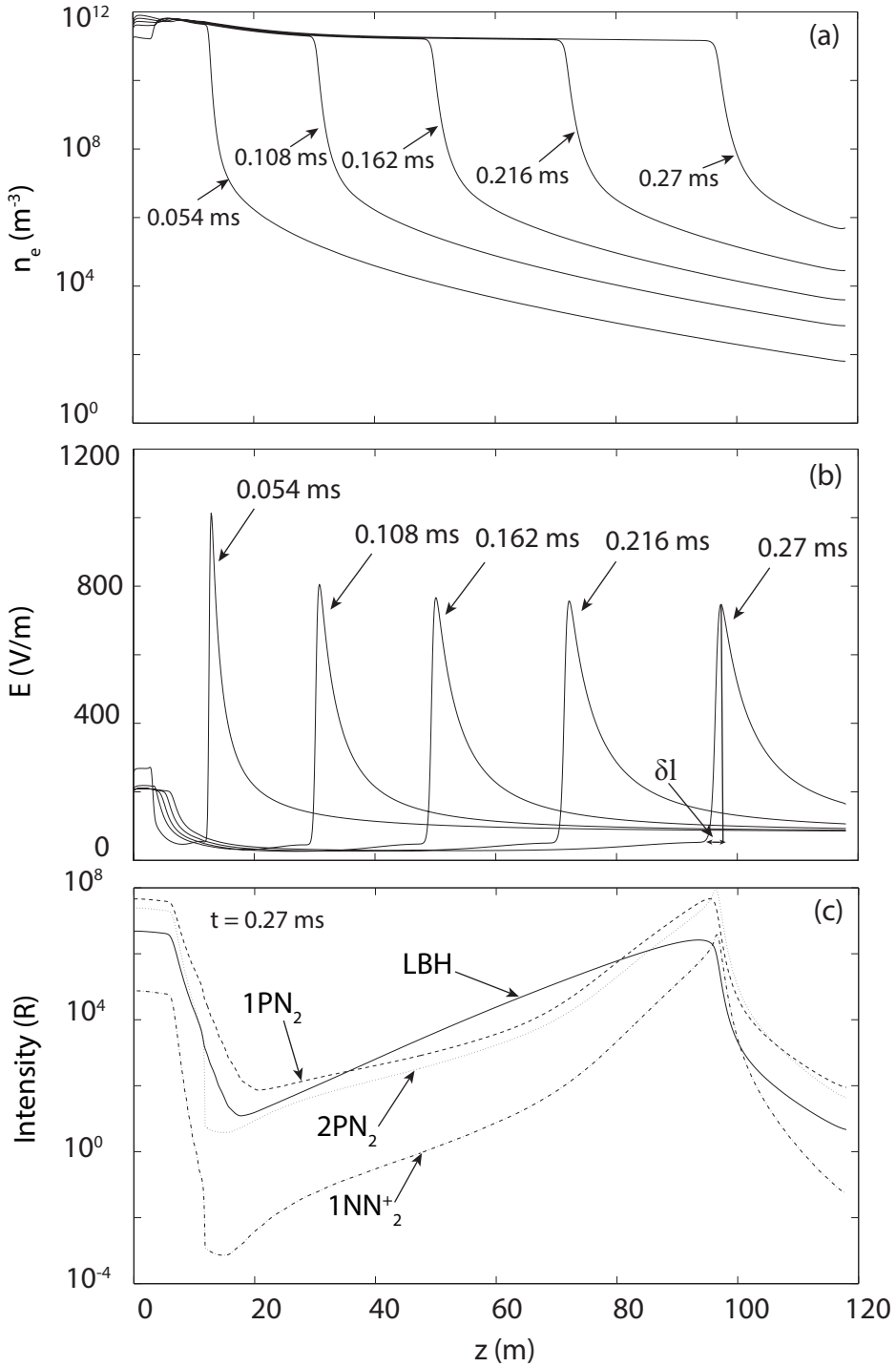


Figure 4.2 – (a)-(c) Electron density, electric field and optical emission profiles from LBH, $1PN_2$, $1NN_2^+$, and $2PN_2$ bands systems, respectively, along the axis of the streamer. The ambient field is $E_0 = 12 \times \frac{N}{N_0}$ kV/cm and the altitude is $h = 70$ km. The quantity $\delta l$ is the characteristic distance over which the gradient of the electric field is strong in the streamer head.

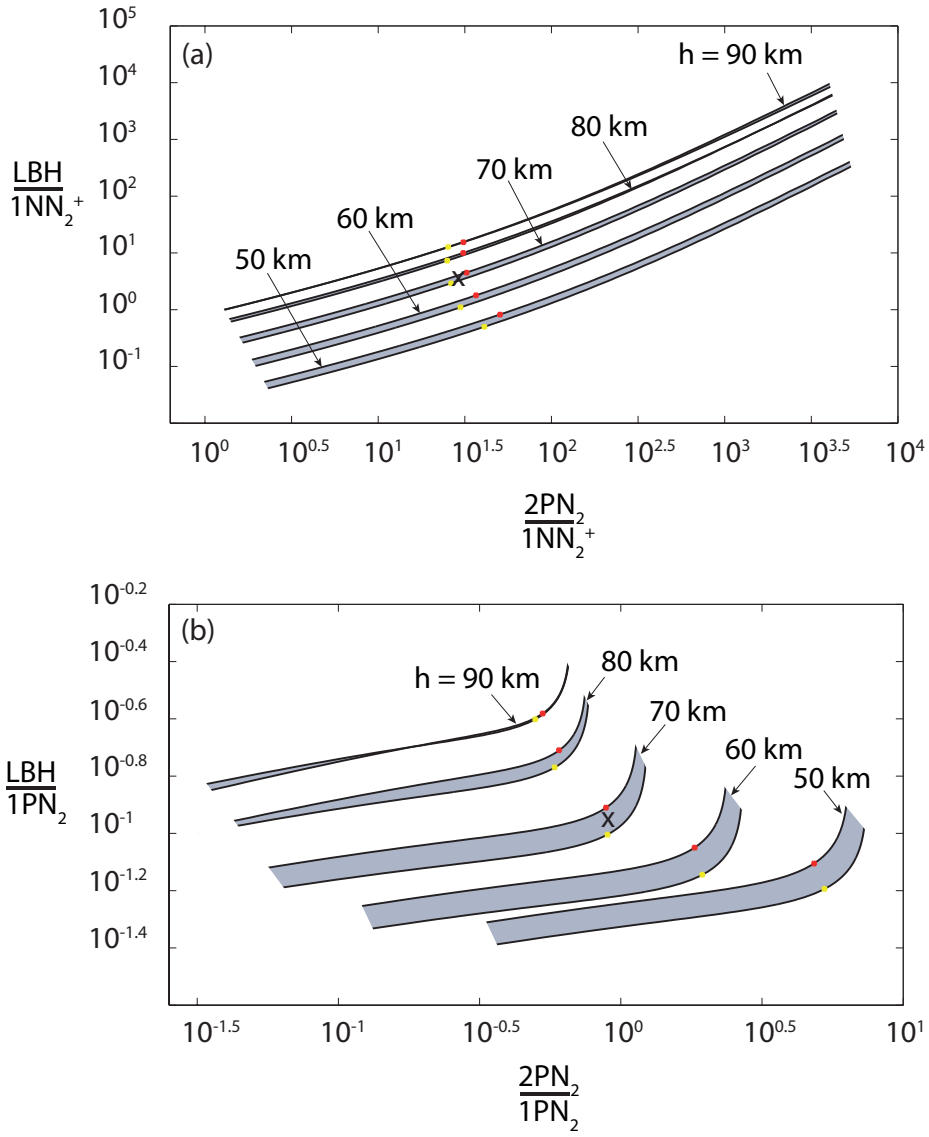


Figure 4.3 – (a)-(b) Parametric representation of optical emission ratios at different altitudes. Marks in red and yellow correspond to streamer simulation results under $E_0 = 12 \times \frac{N}{N_0}$ and $28 \times \frac{N}{N_0}$ kV/cm, respectively.

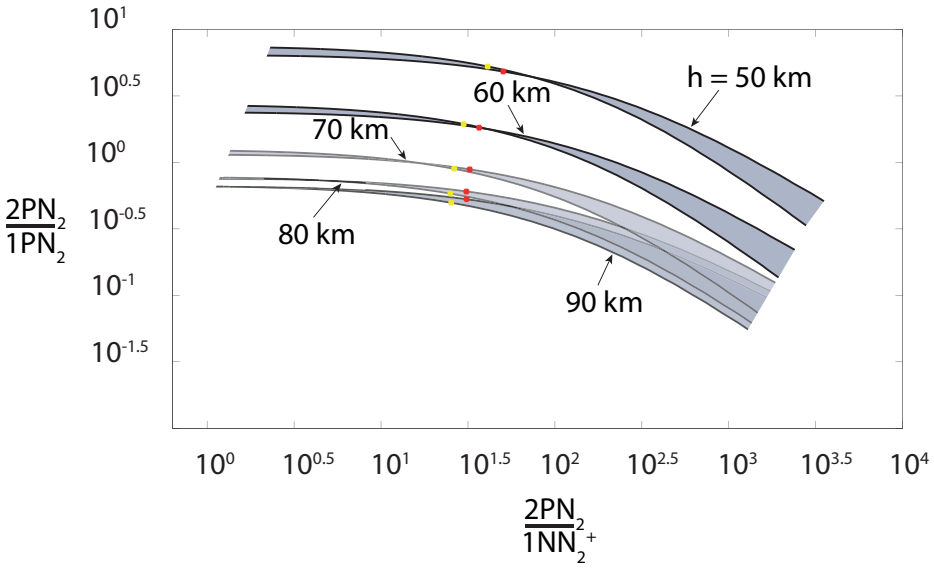


Figure 4.4 – Parametric representation of optical emission ratios at different altitudes, to be used for comparison between satellite measurements and ground observations. Marks in red and yellow correspond to streamer simulation results under $E_0 = 12 \times \frac{N}{N_0}$ and $28 \times \frac{N}{N_0}$ kV/cm, respectively.

At a given location, the electric field at the streamer head varies within a timescale $\delta t \sim \frac{\delta l}{V_{str}}$ (see Figure 4.2), where $V_{str}$ is the streamer velocity, compared to the characteristic lifetime $\tau_k$ of the excited species. From the simulations, $\delta t$ is estimated to be ∼5.7 and 2.5 $\mu$s at 70 km altitude under $12 \times \frac{N}{N_0}$ and $28 \times \frac{N}{N_0}$ kV/cm, respectively, while $\tau_k$ of the excited species $N_2(a^1\Pi_g)$, $N_2(B^3\Pi_g)$, $N_2(C^3\Pi_u)$, and $N_2^+(B^2\Sigma_u^+)$ are estimated to be ∼14.5, 3.4, 0.049, 0.067 $\mu$s, respectively. Therefore, one sees that the populations of $N_2(a^1\Pi_g)$ and $N_2(B^3\Pi_g)$ are not in steady state ($\tau_k > \delta t$) although $N_2(C^3\Pi_u)$ and $N_2^+(B^2\Sigma_u^+)$ are in steady state ($\tau_k < \delta t$).

Moreover, the lifetime $\tau_k$ of a given bands system does not change significantly with altitude above its corresponding quenching altitude as it is mostly defined by its Einstein coefficient $A_k$. Below the quenching altitude, $\tau_k$ is mostly controlled by quenching and scales as $1/N$. However, the characteristic timescale $\delta t$ of electric field variation in the streamer head scales as $1/N$ for all altitudes. As discussed above, the comparison between $\delta t$ and $\tau_k$ determines whether the population of an excited state giving rise to a bands system is in steady state [see also *Celestin and Pasko*, 2010, Section 3]. Since $\tau_k$ is constant above the quenching altitude, there is an altitude above which $\delta t > \tau_k$ and hence steady state is reached. For example,

although $N_2(a^1\Pi_g)$ is not in steady state over most of the altitude range covered by sprites streamers (40-80 km), it can be considered to be in steady state at an altitude of 90 km. However, since $\delta t$ scales as $\tau_k$ below the quenching altitude, the steady/non-steady state nature of an excited species is locked below this altitude.

It is usually considered that LBH cannot be observed from the ground due to absorption in the atmosphere. However ground observations have access to $2PN_2$, $1PN_2$, and $1NN_2^+$ bands systems (see references in the Introduction section). A similar parametric representation as in Figure 4.3 is shown in Figure 4.4 with these bands systems. One sees that the altitude discrimination given by parametric representation is valid only for altitudes ranging between 50 to ∼70 km because of the overlap of different altitude curves that occurs above 70 km. This is an illustration of the suppression of quenching (specifically on $1PN_2$), upon which the method presented in this chapter is based. As the ratio $\frac{2PN_2}{1NN_2^+}$ mostly depends on the electric field in the streamer head [e.g., *Celestin and Pasko*, 2010] and $\frac{2PN_2}{1PN_2}$ is weakly dependent on this field, the parametric representation presented in Figure 4.4 is well defined to measure altitude. It is interesting to note that *Garipov et al.* [2013] have used the ratio $\frac{2PN_2}{1PN_2}$ to make an estimate on the altitude of events observed by the Tatiana-2 satellite. The method we propose here is expected to be much more accurate because it is based on simulations of streamers and we take into account the corrected streamer electric field.

It is also interesting to note that the assumption $\frac{N^*_{e,\nu_k}}{N^*_{e,\nu_{k'}}} = 1$ is not necessary. In fact, one could keep this quantity in the functional dependence of the optical emission ratios (equations (4.10) and (4.11)). In this case, the correction factors become close to one. The development of the corresponding field measurements method and its accuracy with respect to that use in the present chapter is beyond the focus of the present work. However, for the sake of completeness, we have tabulated the ratios $\frac{N^*_{e,\nu_k}}{N^*_{e,\nu_{k'}}}$, for the cases studied in this chapter in Tables 4.7 and 4.8. As shown in Tables 4.7 and 4.8, the ratio $\frac{N^*_{e,\nu_k}}{N^*_{e,\nu_{k'}}}$ varies between 0.57 and 2.76 in the cases studied in this chapter. As explained in Section 4.2.3, correction factors are introduced to compensate the error on the estimated peak field involved by the assumption that $\frac{N^*_{e,\nu_k}}{N^*_{e,\nu_{k'}}} = 1$.

Table 4.7 – Estimated ratio $\frac{N^*_{e,\nu_k}}{N^*_{e,\nu_{k'}}}$ under $E_0 = 12\times\frac{N}{N_0}$ kV/cm, at different altitudes.

| Ratio-Alt (km) | 50 | 60 | 70 | 80 | 90 |
|---|---|---|---|---|---|
| $\frac{2PN_2}{1PN_2}$ | 0.70 | 0.71 | 0.70 | 0.71 | 0.70 |
| $\frac{LBH}{1PN_2}$ | 0.72 | 0.72 | 0.72 | 0.72 | 0.72 |
| $\frac{2PN_2}{1NN_2^+}$ | 2.06 | 2.05 | 2.05 | 2.04 | 2.06 |
| $\frac{LBH}{1NN_2^+}$ | 2.10 | 2.10 | 2.10 | 2.09 | 2.11 |

Table 4.8 – Estimated ratio $\frac{N^*_{e,\nu_k}}{N^*_{e,\nu_{k'}}}$ under $E_0 = 28\times\frac{N}{N_0}$ kV/cm, at different altitudes.

| Ratio-Alt (km) | 50 | 60 | 70 | 80 | 90 |
|---|---|---|---|---|---|
| $\frac{2PN_2}{1PN_2}$ | 0.58 | 0.57 | 0.57 | 0.57 | 0.57 |
| $\frac{LBH}{1PN_2}$ | 0.59 | 0.59 | 0.59 | 0.59 | 0.59 |
| $\frac{2PN_2}{1NN_2^+}$ | 2.72 | 2.65 | 2.66 | 2.63 | 2.66 |
| $\frac{LBH}{1NN_2^+}$ | 2.76 | 2.75 | 2.75 | 2.72 | 2.76 |

Figure 4.3(a)-(b) shows a gap between the curves corresponding to given altitudes under $E_0 = 12 \times\frac{N}{N_0}$ and $28 \times\frac{N}{N_0}$ kV/cm, which is larger at 50 km than at 90 km altitude. The gap is caused by the difference between the correction factors calculated under $E_0 = 12 \times\frac{N}{N_0}$ and $28 \times\frac{N}{N_0}$ kV/cm and the significance of the product $\nu_e\tau_k$ compared to unity (see equations (4.10) and (4.11)) under either one of these ambient fields. The curves tend to overlap at higher altitudes because the correction factors in both cases are getting closer. Under $E_0 = 12 \times\frac{N}{N_0}$ kV/cm the relative contribution of the optical emissions coming from the streamer channel to the total emission is less than that coming from the streamer channel propagating under $E_0 = 28 \times\frac{N}{N_0}$ kV/cm. The reason is twofold: on the one hand, the electric field in the streamer channel is relatively more intense in the $E_0 = 28 \times\frac{N}{N_0}$ kV/cm case which affects the correction factors, and on the other hand, the LBH and $1PN_2$ bands systems are not in a steady state below ∼77 and 67 km, respectively. The latter effect plays a role in increasing the emission in the streamer channel more significantly under $E_0 = 28 \times\frac{N}{N_0}$ kV/cm than under $12 \times\frac{N}{N_0}$ kV/cm. Indeed, the emission in the channel is a contribution of both the streamer head that moves rapidly under $E_0 = 28 \times\frac{N}{N_0}$ kV/cm and the streamer channel itself. In contrast, when the steady state is reached, for example for the $2PN_2$ and $1NN_2^+$ bands systems, the emission profile in the streamer only depends on the local electric field and the electron density at the given time (see Figure 4.2(c)).

Figures 4.3 and 4.4 of the present study are established based on the equations (4.10) and (4.11). These equations are valid for both steady and non-steady state and they take into account the exponential expansion of the streamer. Considering the exponential expansion of streamers with a characteristic timescale $\tau_e = \frac{1}{\nu_e}$, one can see that if $\tau_k \ll \tau_e$ equations (4.10) and (4.11) tend to the equations (4.1) and (4.2) obtained assuming that steady state is reached. This condition is fulfilled only in case of streamers propagating in weak electric field $E_0 \lesssim$10 kV/cm (high $\tau_e$). The exponential expansion of streamers particularly needs to be taken into account at altitudes lower than 80 km and under high background electric fields for the case of ratios composed of LBH and 1PN2 bands systems. However, the steady state assumption remains valid for the ratio $\frac{2PN_2}{1NN_2^+}$. The quantities $\nu_e$ and $\tau_e$ define the characteristic frequency and characteristic time of the streamer expansion, respectively. Within the time $\tau_e$ one can consider that the streamer moves within a distance proportional to the streamer radius $\beta r_s$ and thus:

$$\nu_e \simeq \frac{V_{str}}{\beta r_s} \simeq \frac{\delta l \nu_h}{\beta \alpha r_s} \simeq \frac{\nu_h}{\beta \alpha^2} \tag{4.12}$$

See Figure 4.2 for an illustration of the characteristic length $\delta l \sim \frac{r_s}{\alpha}$ [e.g., *D'yakonov and Kachorovskii*, 1989]. $V_{str} = \frac{\delta l \nu_h}{\alpha}$ is the streamer velocity and $\alpha = \ln(\frac{n_{e_c}}{n_{e_0}})$ [e.g., *Kulikovsky*, 1997; *Babaeva and Naidis*, 1997], where $n_{e_c}$ is the electron density in the streamer channel and $n_{e_0}$ is the electron density taken at a distance $r_s$ from the position of the peak electric field. In the present study, we have $\alpha \sim$13. The quantity $\nu_h$ is the ionization frequency in the streamer head. We estimate $\beta$ using $\nu_e$ obtained in the simulations and equation (4.12) and found it to be between $\sim$1.4 and 2.4 under $E_0 = 12 \times \frac{N}{N_0}$ and $28 \times \frac{N}{N_0}$ kV/cm, respectively. Based on the simulation and equations (4.8) and (4.9), the exponential expansion of the number of excited molecules $N_k$ is caused by the exponential expansion of $N^*_{e,\nu_k}$, which is related to the exponential expansion of the radius $r_s$ of the streamer and hence the volume of the streamer head region.

Moreover, the integration of the optical emissions chosen in this work does not take into account the non physical contribution to the optical emissions produced in the region near the sphere electrode used in our simulations, where the electric field is strong enough ($\sim 3\ E_k$) to generate excited species. However we have included

the emission from the streamer channel since it is considered to be physical [*Liu*, 2010].

We expect that the proposed method is particularly applicable in case of column-niform sprite events that consist of only a few descending streamers. The altitude of positive streamers at the beginning of the developments of carrot sprites could be obtained as well. However, it is predicted that the complexity introduced by the many ascending negative streamers will prevent from obtaining clear results at later moments of the carrot sprite development.

It is expected that the various optical emissions involved in the presented method will not be significantly modified by the transmission through the atmosphere. Preliminary estimates show that emissions between 200 and 240 nm produced at 50 km and observed in a nadir-viewing geometry would be reduced by only ∼10% [T. Farges, personal communication, 2016]. In fact, as the signal is detected by photometers on board the satellite at known location, the effect of atmospheric transmission can be accounted for in a given geometry for the proposed method to be applicable. For an estimation of the altitude within 10 km using the approach developed in the present paper, the maximum uncertainties that are acceptable on different observed ratios have been estimated approximately under $E_0 = 28 \times \frac{N}{N_0}$ kV/cm and are indicated in Table 4.9. We note, that more precise models of populations of excited species (e.g., see [*Eastes*, 2000]), along with accurate quenching coefficients may need to be implemented to improve the accuracy of the parametric representations shown in Figures 4.3 and 4.4 and the method should be first calibrated using joint campaigns associating ground-based (which can resolve the streamers altitudes) and satellite measurments.

Table 4.9 – Estimated maximum uncertainties (%) on different ratios to discriminate between different altitudes within 10 km.

| Altitude (km) | 50-60 | 60-70 | 70-80 | 80-90 |
|---|---|---|---|---|
| $\frac{2PN_2}{1PN_2}$ | 46 | 36.82 | 21.21 | 7.87 |
| $\frac{LBH}{1PN_2}$ | 5.69 | 15.94 | 26.46 | 19 |
| $\frac{2PN_2}{1NN_2^+}$ | 15.72 | 6.27 | 2.55 | 0.635 |
| $\frac{LBH}{1NN_2^+}$ | 37.72 | 44.96 | 43.12 | 27.14 |

Because of the restrictions imposed by the model, the method developed in the present paper is based on separate local simulations conducted at different altitudes

under similar conditions and reasonable values of the ambient electric field needed for the propagation of sprite streamers $\frac{E_0}{E_k}$ ∼0.4 and 0.9 [e.g., *Hu et al.*, 2007; *Li et al.*, 2008; *Liu et al.*, 2009b; *Qin et al.*, 2013b] and it will be very interesting to push the simulation beyond and compare with simulations of streamers initiated under more realistic conditions of ambient electric field, charges species, and ionospheric inhomogeneities [e.g., *Liu et al.*, 2015, 2016] and to study the application of the method introduced in the present chapter.

Finally, we note that the method might also be used for other streamer-based TLEs like upward propagating gigantic jets [e.g., *Kuo et al.*, 2009].

## 4.5 Summary and conclusions

1. We have developed a simulation-based method to infer the altitude of propagating sprite streamers from photometric measurements.
2. The method can also be used to estimate the electric field $E_h$ at the head of propagating sprite streamers and to give information about their velocities.
3. We have estimated analytically the photon flux ratios under a non-steady state assumption of optical emissions taking into account the exponential growth of sprite streamers.
4. We have derived a relation between the frequency $\nu_{\mathrm{e}}$ associated with the expansion of the streamer and the ionization frequency $\nu_h$ at the streamer head.
5. We have calculated correction factors at different altitudes corresponding to different optical emission ratios under different background electric fields $E_0 = 12 \times \frac{N}{N_0}$ and $28 \times \frac{N}{N_0}$ kV/cm under steady and non-steady state assumptions.
6. The method needs to be tested and calibrated because of its sensitivity to the excited species model and the quenching coefficients. We suggest that the verification of the method could be performed using joint observation campaigns associating ground-based and satellite measurements.
7. We suggest that a new method could be developed using simulation-driven values of the optical emission ratios ($\frac{N^*_{\mathrm{e},\nu_{\mathrm{k}}}}{N^*_{\mathrm{e},\nu_{\mathrm{k}'}}} \neq 1$). Its accuracy should be compared with the method elaborated in the present chapter.

8. The method is expected to improve the scientific return of ISUAL, GLIMS, ASIM, and TARANIS space missions and ground observation campaigns.

# Chapter 5

# Some points about the energetics of streamer discharges

**Abstract in French:** Dans le contexte de la compréhension des processus de production d'électrons énergétiques et leurs radiations associées par les décharges streamers, on propose dans ce chapitre, une étude particulière des émissions de ces électrons par des décharges streamers négatives sous des conditions de faible densité de l'air et un champ Laplacien appliqué de l'ordre de 50 kV/cm avec un temps de montée de 3 ns. Ce principe a déja été testé dans une expérience et a prouvé l'existence d'une quantité considérable de rayons X. En plus de l'estimation des électrons énergétiques, on quantifie l'énergie déposée dans l'air par les têtes de streamers et on explore la possible production de rayons X par les streamers de sprite à haute altitude. La possibilité de la production des rayons X par les sprites est une question à laquelle XGRE á bord du satellite TARANIS essaiera de répondre. Nous apportons ici des élements théoriques de réponse à cette question.

## 5.1 Introduction

Streamer discharges are non-thermal plasma filaments characterized by a region of enhanced electric field at their heads, where it usually reaches up to 150 kV/cm

at ground level air. However, under particular conditions, electric fields greater than ∼250 kV/cm can be reached and thermal runaway electrons and associated X-ray emissions can be produced. Laboratory spark discharges in air and lightning stepped leaders are known to produce X-rays [e.g., *Dwyer et al.*, 2005; *Nguyen et al.*, 2010; *Rahman et al.*, 2008; *March and Montanyà*, 2010, 2011]. However, as demonstrated in Chapter 3, the processes behind the production of these X-rays are still not fully understood. Recently, the encounter between negative and positive streamers has been suggested as a plausible mechanism for the production of X-rays by spark discharges [e.g., *Cooray et al.*, 2009; *Kochkin et al.*, 2012, 2015b], but the increase of the electric field involved in this process is accompanied by a strong increase of the conductivity, which in turn makes this electric field collapse over a few tens of picoseconds, preventing the production of significant X-ray emissions [*Ihaddadene and Celestin*, 2015].

Moreover, there is a significant body of studies in the field of laboratory gas discharge experiments, where authors mentioned the production of X-rays in their results [e.g., *Stankevich and Kalinin*, 1968; *Tarasova and Khudyakova*, 1970; *Kremnev and Kurbatov*, 1972; *Mesyats et al.*, 1972]. High electric fields (100-1000 kV/cm) in narrow air gaps were used [e.g., *Mesyats and Bychkov*, 1968]. Emission of runaway electrons, X-rays, and the energy deposited by a streamer discharge were also investigated [e.g., *Gurevich*, 1961; *Aleksandrov*, 1966; *Stankevich*, 1971; *Babich and Stankevich*, 1973]. Cathode related microphysics phenomena such as field amplification processes, field emission, explosive electron emission, cathode erosion process and microrelief, and local plasma burst or cathode-flares, were studied as well [e.g., *Borukhov et al.*, 1973; *Bugaev et al.*, 1975; *Litvinov et al.*, 1983, and references therein]. *Bugaev et al.* [1975, see Section 6] explained that the observed X-rays, were produced by the strong field emission process near the cathode, which is the ejection of conduction electrons from the cathode material when their energy gained due to the high electric field at the surface of the cathode exceeds the metal potential barrier. The high electric field also causes erosion of the cathode [*Bugaev et al.*, 1975, see Section 6] and the appearance of microrelief [*Litvinov et al.*, 1983, see Section3-a] that have been observed using electron microscope [*Bugaev et al.*, 1975; *Litvinov et al.*, 1983]. One of the specific experimental conditions under which

energetic radiations were detected, was the ignition of negative streamer discharges in a low air density environment, in a small gap (4 mm), and parallel electrodes exposed to a given Laplacian electric field $E_0 = 50$ kV/cm with a rise time of 3 ns per pulse [*Kremnev and Kurbatov*, 1972]. The energy deposited by X-rays in the detector per pulse was experimentally measured and theoretically estimated as function of a ratio of the Laplacian applied electric field to the air pressure $E_0/p$ (see Figure 5.1). In this context, we use our previous numerical streamer model to reproduce and investigate this process in a similar configuration as experimental conditions leading to the increase of the electric field and the production of significant amount of thermal runaway electrons at the head of a single negative streamer discharge. We estimate the energies of produced runaway electrons, and the associated X-rays energy deposited per pulse, and compare with the experimental results of *Kremnev and Kurbatov* [1972] (see Figure 5.1). We also quantify the energy deposited at the front of the streamer discharge. This quantity is directly related to the amount of chemical species that can be produced by a streamer discharge [Ihaddadene and Celestin, AGU poster presentation, AE33A-0473, 2015]. In the context of sprites, we also investigate a possible production by sprite streamers at high altitudes of thermal runaway electrons and the associated energetic radiation following the mentioned experimental conditions, and we introduce the notion of energy deposited by sprite streamers. This work seeks to improve the understanding of the energetics behind the X-ray emissions produced by streamer discharges in both laboratory streamers and natural discharges at high altitudes, and the estimation of the energy deposited by a discharge.

## 5.2 Estimation of the energy of the runaway electrons produced by streamers and the corresponding X-ray photons energy

Assuming an electron with an initial energy $\varepsilon_{th}$ located in the streamer head region moving significantly faster than the streamer (see Figure 5.2), this electron will gain energy under the effect of the streamer electric field and lose energy due to the friction force which is function of its own energy (see Figure 1.4). In the present

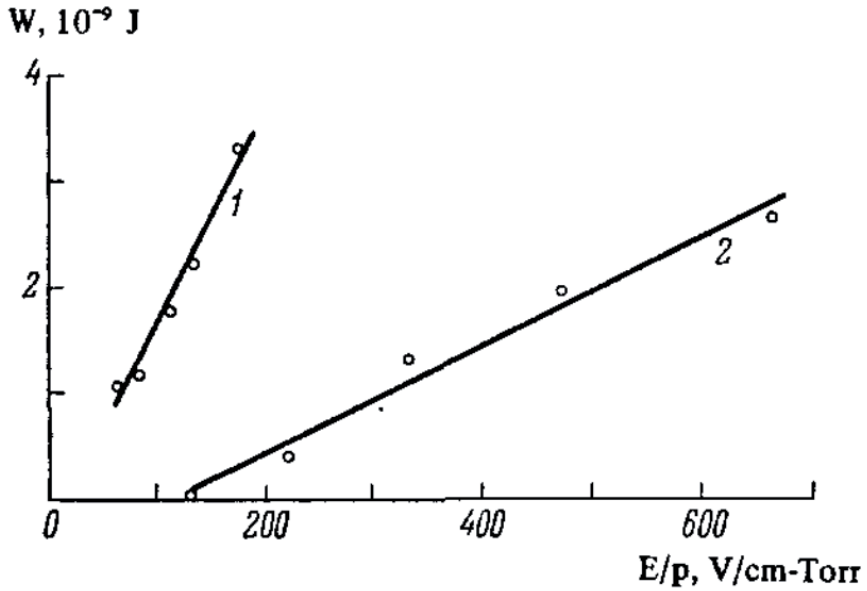


Figure 5.1 – X-ray energy deposited in the detector per pulse versus the reduced Laplacian field in helium (1) and in air (2). Reproduced from [*Mesyats et al.*, 1972].

study, we choose the initial energies: 0, 15, and 126 eV, to quantify the impact on the final energy of the runaway electrons and the associated X-rays. To estimate the energy of the runaway electron at the anode, we use the following equation of a non-relativistic electron moving in an homogeneous electric field $E$ exposed to a friction force $F$ in a given air density $N$:

$$m_e \frac{dV}{dt} = qE - F \tag{5.1}$$

where $F$ is estimated based on [*Moss et al.*, 2006]. This friction is well approximated by the Bethe-Heitler formula [*Lehtinen*, 2000]:

$$F = NZK \left[ \log\left( \frac{m_e^2 v_e^4}{2\epsilon} \right) - 2\log(2) + 1 \right] \tag{5.2}$$

where $K = \frac{2\pi q_e^4}{(4\pi\epsilon_0)^2 m_e v_e^2}$, $\epsilon \simeq 85$ eV for air [*ICRU Report 37*, 1984], $Z = 14.5$, and $N$ the local air density.

The flux of runaway electrons $\Theta$, is calculated as follows:

$$\Theta = n_{e_h} S_{str} v_d R \tag{5.3}$$

where $n_{e_h}$, $S_{str} \simeq \pi r_s^2$, $v_d$, and $R$, are respectively the electron density at the location of the peak electric field in the streamer head, the streamer section, the electron drift velocity, and the portion of runaway electrons with energies $> \varepsilon_{th}$ to the total number of electrons at the streamer head. Assuming a Maxwell-Boltzmann distribution of the electrons as function their energies, the quantity $R$ is estimated as follows:

$$R = \frac{2}{\sqrt{\pi}(k_B T_e)^{\frac{3}{2}}} \int_{\varepsilon_{th}}^{\infty} \sqrt{\varepsilon} \exp\left(\frac{-\varepsilon}{k_B T_e}\right) d\varepsilon = \text{erfc}(\sqrt{\varepsilon_{th}}) + \frac{2}{\sqrt{\pi}} \sqrt{\frac{\varepsilon_{th}}{k_B T_e}} \exp\left(-\frac{\varepsilon_{th}}{k_B T_e}\right) \tag{5.4}$$

where $\text{erfc}(x) = \frac{2}{\sqrt{\pi}} \int_x^{\infty} \exp\left(-t^2\right) dt$ is the complementary error function. The quantities $k_B$ and $T_e$ are respectively the Boltzmann constant and the electron temperature.

If one assumes a runaway electron with an energy $\varepsilon > 1$ keV, this electron produces an X-ray with a maximum energy $\varepsilon$. In the following, one assumes that X-rays are produced when electrons impact the anode and that, given the energy range considered here, photoelectric effect is dominant in the transport of electrons through the anode. When photons pass through an aluminum anode characterized with an absorption coefficient $\mu$ and thickness $x$, the final total energy of X-rays $W_X$ deposited in the detector is [*Kremnev and Kurbatov*, 1972]:

$$W_X = \sum_i \Theta \varepsilon \delta t \exp(-\mu x) \tag{5.5}$$

where $i = 1, 2, 3$, etc., refers to a streamer discharge at a given instant $t_i$, and $i = 1$ corresponds to a streamer discharge with an electric field at the head $E_h \geq 260 \times \frac{N}{N_0}$. The quantity $\delta t$ is a characteristic duration between two different instants of time $t_i$ and $t_{i+1}$ of a streamer discharge ($\delta t = t_{i+1} - t_i$).

## 5.3 Estimation of the energy deposited in the gas by the streamer discharge

Electrons gain energy from the electric field and contribute to the different processes such as ionization, and attachment involved in the formation of the streamer discharge. One can express the power density ($\frac{dQ}{dt}$) [e.g., *Stankevich*, 1971] using

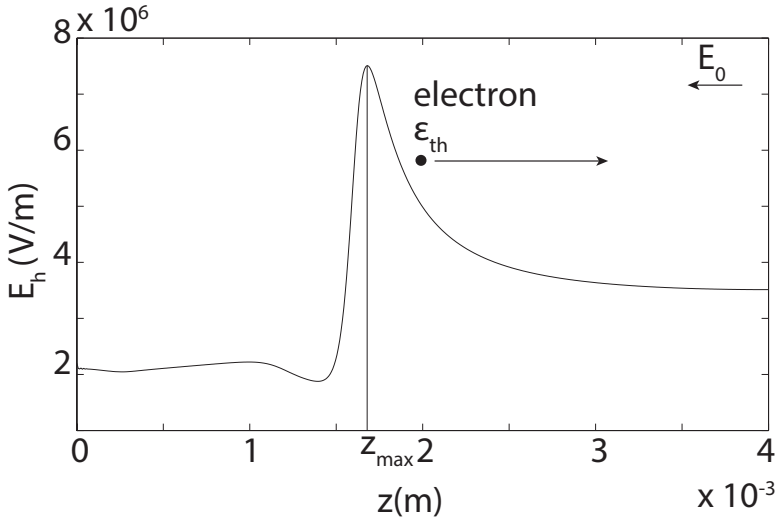


Figure 5.2 – Illustration of the acceleration of an electron with an initial energy $\varepsilon_{th}$ in a negative streamer electric field. The negative streamer propagates in weak air density medium $\frac{N_0}{5}$ (see details of simulation conditions in the Section 5.4)

streamer parameters as follows:

$$\frac{dQ}{dt} = q_e n_e v_d E = q_e n_e \mu_e E^2 = \frac{\epsilon_0}{\tau_r} E^2 \tag{5.6}$$

where $\tau_r = \frac{\epsilon_0}{q_e n_e \mu_e}$ is the relaxation time. When the electron density stops raising and the saturation regime is reached, the relaxation time ($\tau_r$) is almost equal to the ionization time ($\tau_i = \frac{1}{\nu_i}$) in the streamer head [*Qin and Pasko*, 2015], $\tau_r = \frac{1}{\nu_i}$ and thus the above rate ($\frac{dQ}{dt}$) can be expressed differently:

$$\frac{dQ}{dt} = \epsilon_0 \nu_i E^2 \tag{5.7}$$

The quantity $Q$ is the density of the energy deposited by the electric field $E$ during the time $\tau_r$.

## 5.4 Modeling results and discussion

In the present study, we use the streamer model presented in the Chapter Streamer Model Formulation. The boundary conditions applied to Poisson's equation are the following: $\left.\frac{\partial \phi}{\partial r}\right|_{r=0} = 0$, $\phi(0 \leq \text{r} \leq 1.92 \text{ mm}, \text{z} = 0) = 0$, $\phi(\text{r}, \text{z}{=}4 \text{ mm}) = \text{U}$, and $\phi(\text{r} = 1.92 \text{ mm}, 0 \leq \text{z} \leq 4 \text{ mm}) = \text{U}\times(\text{z}/4 \text{ mm})$ where U = 12 kV and

corresponds to an amplitude of homogeneous Laplacian field $E_0 = 50$ kV/cm, and a derivative $\frac{dE_0}{dt} = \frac{50}{3}$ kV/cm/ns ($E_0 = E_{00} + \frac{dE_0}{dt} \times t$) where $E_{00} = E_k(N)$, between the plane electrodes. Negative streamers are initiated on the left side of the simulation domain by placing a Gaussian of neutral plasma cloud with characteristic sizes $\sigma_z = 100$ $\mu$m, $\sigma_r = 100$ $\mu$m and $n_{e_0} = 10^{18}$ m$^{-3}$, in the vicinity of the electrode.

We quantify the densities of excited species of $N_2(B^3\Pi_g)$, $N_2(C^3\Pi_u)$, and $N_2^+(B^2\Sigma_u^+)$ associated with optical emissions of the first positive band system of $N_2$ ($1PN_2$), the second positive band system of $N_2$ ($2PN_2$), and the first negative band system of $N_2^+$ ($1NN_2^+$), respectively.

In this work, we show simulation results performed at a varying ground level air density $N_0 = 2.688\times10^{25}$ m$^{-3}$ with factors $\delta = 1$, 2, 3, 4, and 5, which correspond to neutral air densities $N = N_0, \frac{N_0}{2}, \frac{N_0}{3}, \frac{N_0}{4}$ and $\frac{N_0}{5}$, under an externally applied homogeneous electric field $E_0 = 50$ kV/cm with a rise time of 3 ns, and a spatial resolution $\Delta z = 8$ $\mu$m and $\Delta r = 8$ $\mu$m in a simulation domain (501×241) discretized over regular grid points. Moreover, extension to sprite streamers and their energy deposition, and possible emission of energetic radiation in comparison to laboratory discharges is also discussed in this Chapter.

### 5.4.1 Emission of thermal runaway electrons and the associated X-rays

Figure 5.3 (a)-(b) shows the cross sectional view of the electron density of two streamer discharges propagating respectively in ambient air density $N_0$ and $\frac{N_0}{5}$. One can see clearly that the streamer in air density $\frac{N_0}{5}$ propagates faster that the streamer in air density $N_0$. They both cross the gap (∼4 mm) between the parallel electrodes within 3.15 ns and 1.82 ns which correspond, respectively to mean velocities of $1 \times 10^6$ m/s and $1.85 \times 10^6$ m/s. We also see that the streamer propagating in air air density $\frac{N_0}{5}$ possesses a larger radius ($r_s$) than the one in air density $N_0$, as well as a higher exponential expansion rate $\nu_{e\,\frac{N_0}{5}} > \nu_e$ (see Chapter 4, equation (4.12)).

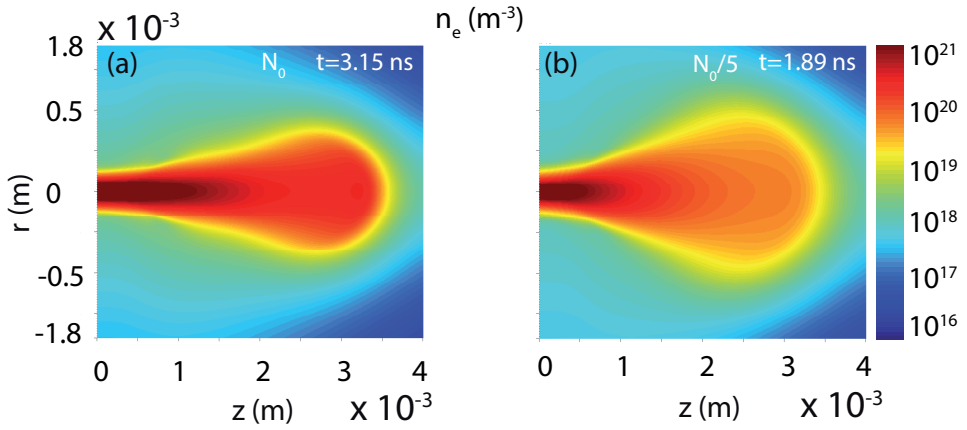


Figure 5.3 – (a)-(b) Cross sectional view of the electron density in air densities $N_0$ and $\frac{N_0}{5}$, respectively.

Figure 5.4 (a)-(b) shows the evolution of the maximum electric field at the streamer head in different ambient air densities $\frac{N_0}{\delta}$, the ratio $\frac{2\mathrm{PN}_2}{1\mathrm{NN}_2^+}$, and the ratio $\frac{2\mathrm{PN}_2}{1\mathrm{PN}_2}$ versus time. One can see clearly, that the maximum electric field is higher in the case in which air density is $N_0$ than that in other configurations. However it does not reach the limit of 260 kV/cm necessary for the production thermal runaway electrons, unless the streamer starts approaching the anode. In contrast, in the case of weak air density ($\delta > 1$), the electric field reaches values higher than $\frac{260}{\delta}$ kV/cm before the streamer reaches the anode. Precisely, the electric field starts to go beyond the limit for producing runaway electrons ($\frac{260}{\delta}$ kV/cm) at times (2.59, 1.85, 1.59, and 1.39)$\times 10^{-9}$ s, respectively for factors $\delta$ = 2,3,4, and 5. As the ambient air density decreases, the value of the breakdown electric field decreases as it scales as $E_k^{'} = \frac{E_k}{\delta}$ (see Chapter 2 for similarity laws) and the thermal runaway electrons threshold field will decrease proportionally. One sees also, that the ratio $\frac{2\mathrm{PN}_2}{1\mathrm{NN}_2^+}$ decreases as the maximum electric field increases. Indeed, as the electric field increases the relative intensity of the $1\mathrm{NN}_2^+$ starts increasing as well because of the amplification of the number of electrons with energies $>$ 18.8 eV needed for the excitation of the $B^2\Sigma_u^+$ state responsible for the $1\mathrm{NN}_2^+$. In contrary, the energy of electrons needed for the excitation of the $C^3\Pi_u$ state responsible for the $2\mathrm{PN}_2$ is only 11 eV. The same happens to the ratio $\frac{2\mathrm{PN}_2}{1\mathrm{PN}_2}$ involving $1\mathrm{PN}_2$ produced by electrons with lower energies (7.35 eV) than $2\mathrm{PN}_2$. We note that Figure 5.4 (a)-(b) is useful for applications in laboratory. One sees that the ratios $\frac{2\mathrm{PN}_2}{1\mathrm{NN}_2^+}$ and $\frac{2\mathrm{PN}_2}{1\mathrm{PN}_2}$ as

functions of time are practical quantities to use to measure the increase of the field and estimate the maximum values reached in the discharge.

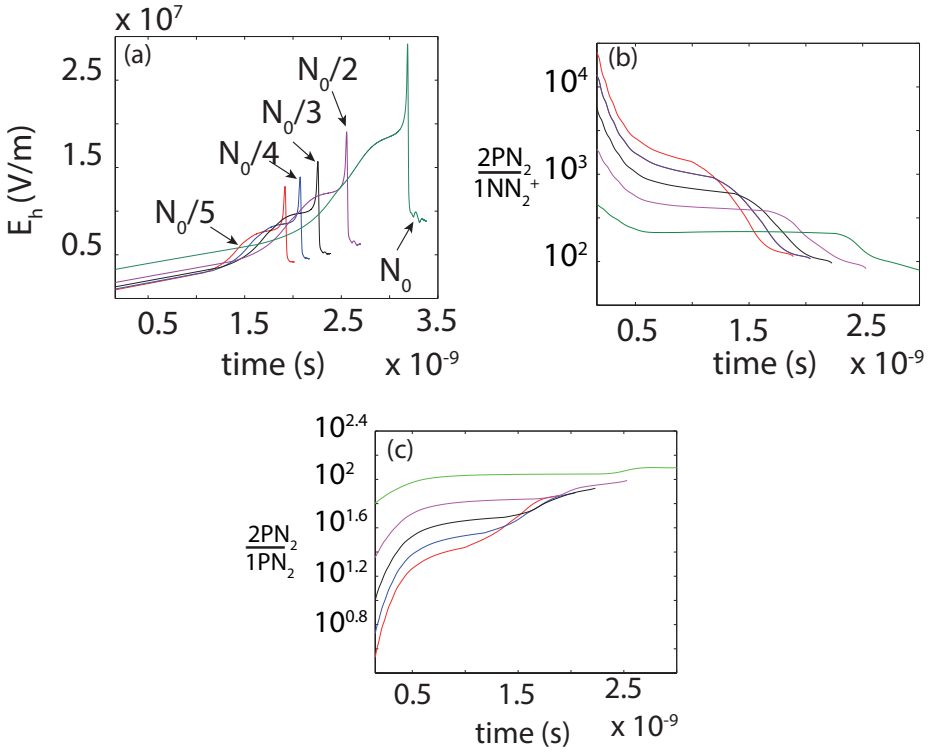


Figure 5.4 – (a)-(b) and (c): Electric field ($E_h$) at the streamer head, the ratio $\frac{2PN_2}{1NN_2^+}$, and the ratio $\frac{2PN_2}{1PN_2}$, respectively, at different ambient air densities versus time.

Figure 5.5 shows the estimated energy of the X-rays produced by runaway electrons at their arrival to the aluminum anode in each simulation, versus $E_0/p$. The results are order of magnitude approximations because of the Maxwell-Boltzmann energy distribution assumption has been found valid only for high energy electrons, the time spent by an electron to reach the anode may be higher than $\delta t$, the fixed value of the photoionization parameter $p_{O_2} = 150$ Torr in all simulation cases (despite the variation of $p_{O_2}$, the values of the energies of individual electrons $\varepsilon$ and $W$ found in this chapter decrease by ~3 and ~40 %, respectively). In Tables 5.1, 5.2, and 5.3, we show the maximum energies of the runaway electrons at their arrival at the anode and their associated X-rays based on different initial energies $\varepsilon_{th}$. One sees, that $\varepsilon_{th}$ does not affect neither the final energy of runaway electrons, nor the energy of their associated X-rays. The use of $\varepsilon_{th} = 0$ or 15 eV results in a factor ~2 difference on the energy of X-rays. However, considering $\varepsilon_{th} = 126$ eV, results

in factors ∼8000 to ∼20000 with the respect to $\varepsilon_{th}$ = 15 and 0 eV, respectively. We have used a Monte Carlo approach to verify these estimates in the case of an ambient air density of $\frac{N_0}{5}$. This Monte Carlo test has led to a value of ∼200 nJ (without taking into account photon transport through the anode), i.e., approximately within a factor of 20 to 700 of our estimate. We have also used X-rays absorption coefficients from NIST and took into account the 0.05 cm thick anode mentioned in [*Kremnev and Kurbatov*, 1972], and we have found that simulation results are a factor ∼10 to ∼2000 corresponding to initial energies $\varepsilon_{th}$ = 126 and 0 eV, respectively, compared with experimental results ([See Table 1 *Kremnev and Kurbatov*, 1972]). An experimental value of 1 nJ ($\frac{E_0}{p}$∼300 V/cm/Torr) was found in [*Kremnev and Kurbatov*, 1972]. The fact that the detector response and the uncertainty on the thikness of the anode are not taken into account, may also affect our results.

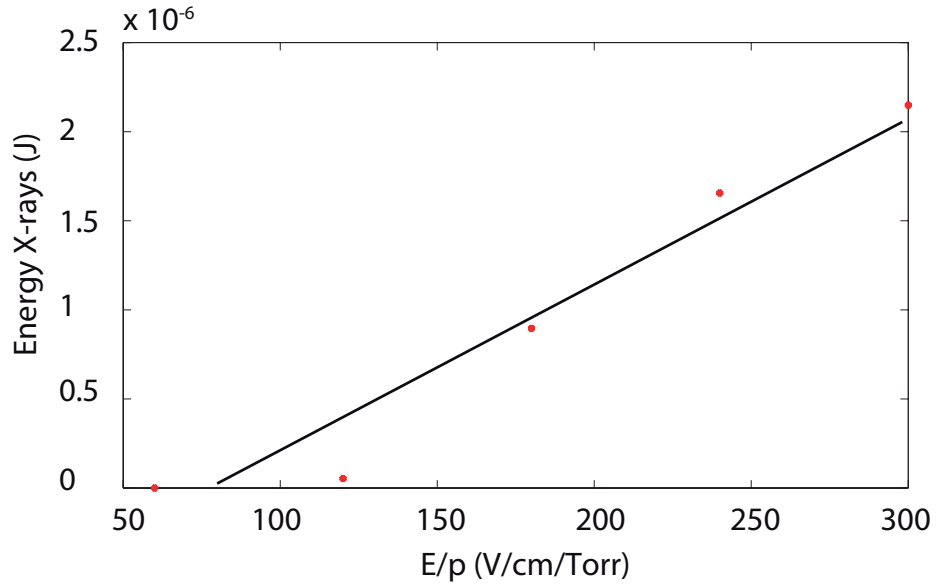


Figure 5.5 – Energy of the X-rays produced by a negative streamer discharge versus $E/p$. The quantity $\varepsilon_{th}$=15 eV.

Table 5.1 – The maximum energy of thermal runaway electrons $\varepsilon$ (keV) and the associated X-rays (without taking into account the anode) $W$ (nJ) in different ambient air densities $N$ ($m^{-3}$) and $\varepsilon_{th}$ = 126 eV.

| N | $N_0$ | $\frac{N_0}{2}$ | $\frac{N_0}{3}$ | $\frac{N_0}{4}$ | $\frac{N_0}{5}$ |
|---|---|---|---|---|---|
| $\varepsilon$ | 0 | 2.0 | 4.4 | 5.7 | 5.9 |
| $W$ | 0 | 0.00125 | 0.04000 | 0.11000 | 0.26500 |

Table 5.2 – The maximum energy of thermal runaway electrons $\varepsilon$ (keV) and the associated X-rays (without taking into account the anode) $W$ (nJ) in different ambient air densities $N$ ($m^{-3}$) and $\varepsilon_{th} = 15$ eV.

| N | $N_0$ | $\frac{N_0}{2}$ | $\frac{N_0}{3}$ | $\frac{N_0}{4}$ | $\frac{N_0}{5}$ |
|---|---|---|---|---|---|
| $\varepsilon$ | 0 | 1.1 | 3.6 | 5.0 | 5.5 |
| $W$ | 0 | 53 | 896 | 1656 | 2149 |

Table 5.3 – The maximum energy of thermal runaway electrons $\varepsilon$ (keV) and the associated X-rays (without taking into account the anode) $W$ (nJ) in different ambient air densities $N$ ($m^{-3}$) and $\varepsilon_{th} = 0$ eV.

| N | $N_0$ | $\frac{N_0}{2}$ | $\frac{N_0}{3}$ | $\frac{N_0}{4}$ | $\frac{N_0}{5}$ |
|---|---|---|---|---|---|
| $\varepsilon$ | 0 | 1.1 | 3.6 | 5.0 | 5.5 |
| $W$ | 0 | 147 | 2286 | 4006 | 4847 |

### 5.4.2 Sprite streamers

At high altitudes, local air density fluctuations (e.g., 5% atmospheric density variations produced by gravity waves [*Gardner and Shelton*, 1985]) and corresponding increase of the reduced electric field may occur. Figure 5.6 shows the simulation results of a positive sprite streamer at 80 km altitude, propagating in an ambient electric field $E_0 = 12 \times \frac{N}{N_0}$ kV/cm (situation that corresponds to a quasi-electrostatic electric field caused by a former +CG lightning) in a normal air density environment $N_{80}$ (0 m $< z <$ 200 m) for $\sim$1 ms, entering a low air density region ($z >$ 200 m and $\delta \simeq 3$ which corresponds to variation of air density of $\sim$66%). Hence, the ambient electric field passes suddenly to $29 \times \frac{N}{N_0}$ kV/cm. The results show that sprites are unlikely to produce energetic electrons even extreme conditions assumed in the present simulation, because the electric field does not reach the limit $\sim$133 kV/cm necessary to produce thermal runaway electrons in a density background $\frac{N_{80}}{\sim 3}$. In case of a negative streamer, the electric field under the same conditions will produce a weaker peak electric field than in the case of positive one. However, if conditions such as the occurence of an ambient electric field $E_0 \simeq 50 \times \frac{N_{80}}{N_0}$ kV/cm [*Qin et al.*, 2013b] with a rise time of $3 \times 10^{-9} \frac{N_0}{N_{80}} \sim$0.2 ms [*Kremnev and Kurbatov*, 1972] in the sprites halo at 80 km altitude, and local air density fluctuation with a factor of just $\delta = 2$ are filled, sprite streamers may produce energetic electrons and X-rays.

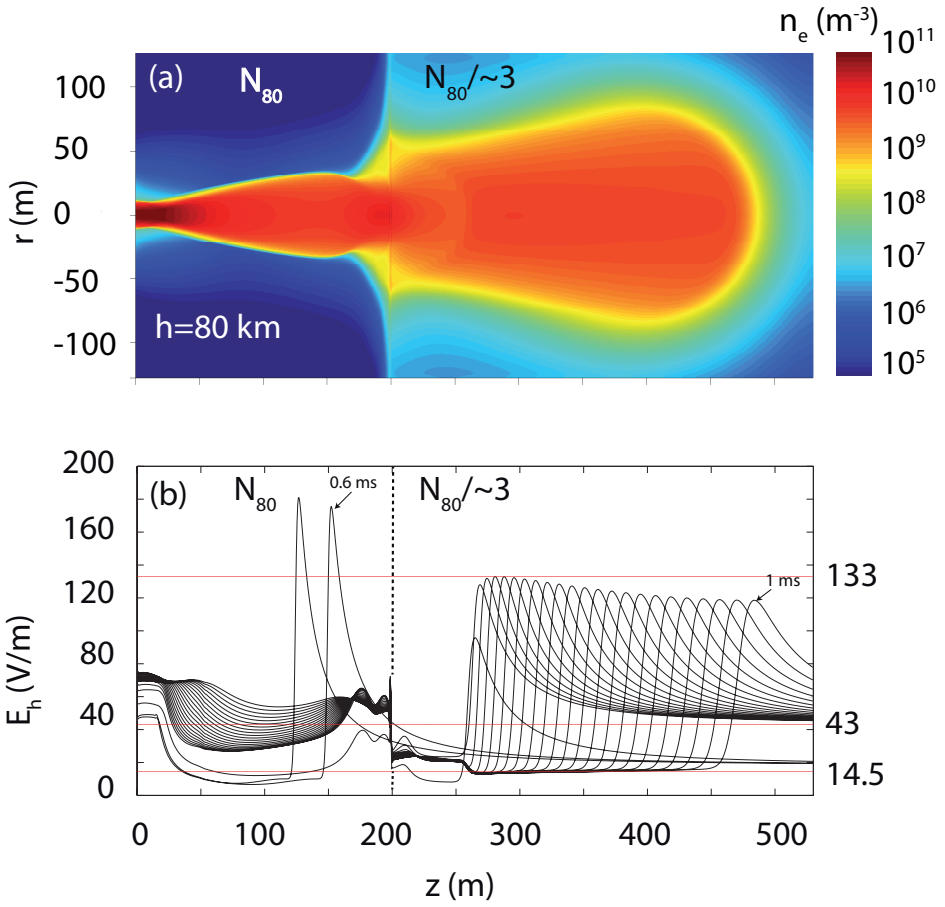


Figure 5.6 – (a) Cross sectional view of the electron density of a positive sprite streamer at 80 km altitude in background air densities $N_{80}$ and $\frac{N_{80}}{3}$, respectively. (b) Electric field along the axis in background air densities $N_{80}$ and $\frac{N_{80}}{\sim 3}$, respectively. The dotted line in (b) shows the separation between the two background air densities. The values 133 V/m, 43 V/m, and 14.5 V/m correspond to the electric field necessary to produce runaway electrons at 80 km altitude in a background air density $\frac{N_{80}}{3}$, the breakdown electric fields at 80 km altitude in $N_{80}$ and $\frac{N_{80}}{\sim 3}$, respectively. The streamer is initiated in a sphere-to-plane configuration by placing a Gaussian plasma cloud near the sphere electrode (see Section 4.2).

### 5.4.3 Energy deposited by a streamer head region

Figure 5.7 (a)-(b) shows respectively, the estimated energy deposited by the streamer head region in the case of simulation of laboratory streamer discharge, under different ambient air densities, and the energy deposited by a sprite streamer head region propagating at 70 km altitude in normal air density conditions, and in a background electric field $E_0 = 12 \times \frac{N}{N_0}$, and $28 \times \frac{N}{N_0}$ kV/cm versus time. This energy is estimated by calculating numerically the equation (5.6) locally in the simulation domain, and averaging the energy density around the maximum electric field in the streamer head region (section of cylindrical volume: $\pi r_s^2 \times \Delta l$). One can see clearly, that this energy in case of laboratory streamer discharges varies from $\mu$J to $n$J, and increases as the electric field continues to increase, and streamers in weak air density deposit a lower energy than those in normal air density $N_0$. The values of energy found via simulations are in an order of magnitude agreement with those found by *Pai et al.* [2010] in glow, and spark regimes ($\sim$1 to 1000 $\mu$J). Sprite streamers deposit higher energies than those of laboratory discharges. From Figure 5.7 we can deduce a factor of $10^4 \sim \frac{10^{-2}}{10^{-6}}$ difference. This can be explained using equation (5.7) as follows: the elementary deposited energy density $dQ = \epsilon_0 \nu_i E^2 dt$. The frequency $\nu_i$ scales as $\frac{N}{N_0}$, $E$ scales as $\frac{N}{N_0}$, time scales as $\frac{N_0}{N}$, and length scales as $\frac{N_0}{N}$, hence the energy density scales as $\frac{N^2}{N_0^2}$, and the total energy deposited scales as $\frac{N_0}{N}$. Indeed, the factor $10^4$ difference between sprite streamers, and laboratory discharges is close to $\frac{N_0}{N_{70}}$. Note that the comparison in the current study is limited by the fact that we compare positive sprite streamer and laboratory negative streamer.

## 5.5 Summary and conclusions

1. The streamer plasma fluid model was used to estimate the energy of runaway electrons and the associated X-rays in the experimental study of *Kremnev and Kurbatov* [1972]. Despite the strong overestimations made, the X-ray energy falls within factors $\sim$20 to $\sim$700 of the Monte Carlo simulation results and within factors of $\sim$10 to $\sim$2000 of the experimental results.

2. We have estimated the energy deposited by the corresponding laboratory streamer discharges to be around $\mu$J. Sprite streamer heads are found to

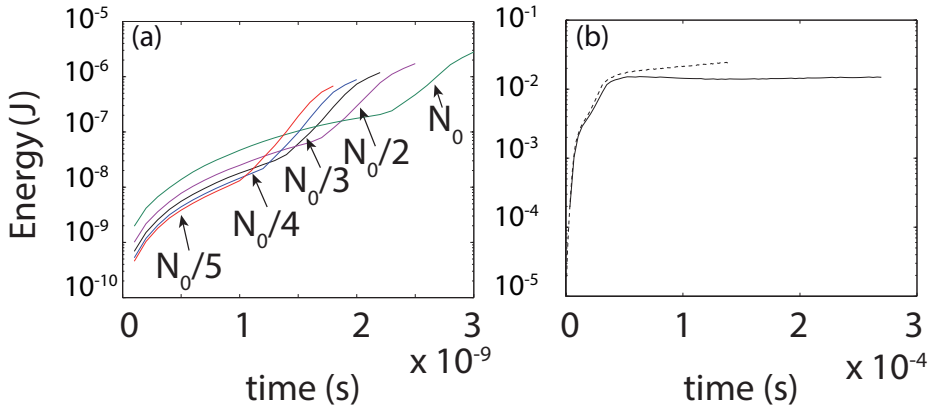


Figure 5.7 – (a) Energy (joule) deposited by laboratory streamer discharges for different values of the ambient air densities $N_0$. (b) Energy deposited by sprite streamers initiated in a sphere-to-plane configuration at 70 km altitude under $E_0 = 12 \times \frac{N}{N_0}$ (solid line) and $E_0 = 28 \times \frac{N}{N_0}$ (dashed line), respectively (see Section 4.2).

deposit energies on the order of ∼10 mJ.

3. We have found a good agreement between the simulation results of the energy deposited and that measured for laboratory streamers.

4. We have found that sprite streamers are unlikely to be a source of energetic electrons and X-rays when subjected to neutral density variations.

# Chapter 6

# Summary, conclusions, and suggestions for future work

**Abstract in French:**

Dans ce dernier chapitre, on résume les conclusions majeures du travail effectué durant le doctorat et les prospectives d'avenir. Un modèle de plasma fluide qui simule les décharges de type streamer a été developpé. Le modèle est basé sur les équations de dérive-diffusion des électrons et des ions couplées avec l'équation de Poisson. Les coefficients de transport comme l'ionisation, l'attachement, la mobilité, etc., sont des fonctions explicites du champ électrique local. Le modèle contient une méthode intégrale pour le calcul de la photoionisation et la technique FCT qui capture les gradients très forts dans les décharges. L'application simple de la méthode FCT fait apparaitre des oscillations numériques le long de l'axe du streamer. Nous avons résolu ce problème en ajoutant des flux dissipatifs et transporté une fonction exponentielle de la densité. Le modèle est aussi supplémenté du calcul des espèces excitées de la molécule d'azote et de l'ion $N_2^+$ produits par la décharge streamer et les émissions optiques associées. Notre modèle streamer permet de simuler différentes configurations: électrodes en géométrie plan-plan, électrodes en géométrie pointe-plan, des streamers de laboratoire et des streamers de sprites. Un solver SOR a été aussi développé afin de résoudre l'équation de Poisson.

Durant cette thèse, dans le but de faire progresser la compréhension des mécanismes d'émission des rayons X par les décharges streamers, nous avons abordé deux

mécanismes possibles de production d'électrons runaway thermique: l'un est la collision frontale de deux streamers positif et négatif et l'autre est la production directe par une décharge streamer négative qui se propage dans un champ électrique réduit extrême. Parmi ces deux mécanismes, le premier n'a pas permis l'obtention d'une quantité observable de rayon X tel qu'il avait été supposé au vu de certains indices expérimentaux. Le deuxième permet d'obtenir une quantité significative de rayons X et nous avons pu obtenir un accord avec l'expérience en terme d'ordre de grandeur (pour une distribution d'électrons couvrant une échelle dynamique de plus de 7 ordres de grandeurs). La question de l'émission de rayon X par les sprites a aussi été traitée et c'est l'un des objectifs de la mission TARANIS (CNES). Des simulations sous des conditions extrêmes ont été réalisées et ont montré que les sprites ne produisent pas de champs électriques suffisament forts pendant des temps suffisants pour produire une émission d'électrons runaway thermique significative et les rayons X associés. Nous avons aussi utilisé ce modèle pour estimer l'énergie déposée par un streamer de laboratoire de l'ordre du microjoule et par un streamer de sprite de l'ordre du millijoule.

La mission spatiale TARANIS (CNES) observera les TLE depuis le nadir. Cette géométrie d'observation réduit l'absorption atmosphérique mais ne permet pas d'obtenir une bonne résolution verticale du phénomène. En utilisant le modèle streamer developpé au cours de cette thèse nous avons formulé une méthode spectrophotométrique basée sur les ratios des émissions optiques produites par les sprites. Cette méthode permet d'estimer l'altitude, la vitesse de descente des streamers de sprite, et le champ électrique à leur tête. Cette méthode améliorera le retour scientifique de TARANIS et les autres missions spatiales comme ASIM (ESA) et GLIMS (JAXA).

## 6.1 Summary and conclusions

In this dissertation, we have developed a streamer discharge plasma fluid model based on drift-diffusion equations for electrons and ions, that is coupled with Poisson's equation (see Chapter 2). The transport coefficients such as ionization, attachment, mobility, and diffusion coefficients are explicit functions of the local electric field. The model includes an integral method to calculate the effect of the photoionization process [*Zheleznyak et al.*, 1982] and the FCT (flux corrected trans-

port) technique [*Zalesak*, 1979] used for capturing steep gradients that occur in streamer modeling. When the FCT technique is implemented as such, numerical oscillations and their amplifications occur in the vicinity of the streamer axis. Dissipative fluxes combined with the transport of an exponential function of the density have been used to remove these oscillations. In addition, an SOR (successive overrelaxation) Poisson's solver has been also developed. The model is also coupled with an optical emission model that quantifies the excited species of $N_2$ and their associated optical emissions produced by a streamer discharge. The model simulates streamer discharges in different configurations: plane-to-plane electrode geometry, point-to-plane electrode geometry, and both laboratory streamer discharges and sprite streamers, which are produced at high altitudes ∼40-90 km. This model has been used to address the various questions that have been exposed in the Introduction section.

The process of head-on collision between negative and positive streamer discharges has been studied [*Ihaddadene and Celestin*, 2015] (see Chapter 3). The results showed that this mechanism could not be a source of significant production of thermal runaway electrons and X-rays as it was suggested previously based on laboratory experiments [*Cooray et al.*, 2010; *Kochkin et al.*, 2012]. The conditions under which the simulations have been conducted have been maximized on purpose to observe the production of thermal runaway electrons and the associated X-rays. We have used high external Laplacian electric fields such as 50 and 60 kV/cm in plane-to-plane electrodes. However, the significant rise of the electron density that causes a quick collapse of the electric field at this location prevents efficient production of thermal runaway electrons. Moreover, estimations made with a Monte Carlo model using the results from the streamer model led to a number of X-ray photons with energies $> 1$ keV lower than 2000 per negative/positive streamer head-on collision.

Head-on collision between positive and negative streamers are found to produce transient luminous optical patches [*Ihaddadene and Celestin*, 2015] clearly visible in the $1NN_2^+$ bands system. *Cummer et al.* [2006] showed that collisions between downward sprite streamer heads and adjacent streamer channels form long lasting sprite beads. Moreover, structures called pilot systems [*Kochkin et al.*, 2012] that

create positive and negative streamers in laboratory meter scale discharges could happen at high altitude, and chances are that numerous head-on collisions between positive and negative streamers occur and might be associated with sprite beads [*Gordillo-Vázquez et al.*, 2012].

The streamer model developed in the present dissertation was also used in Chapter 5 to reproduce experimental results of laboratory streamer discharges of *Kremnev and Kurbatov* [1972]. The experiment focused on the production of runaway electrons by negative streamer discharges and the associated X-rays in low air density under high applied Laplacian electric field of 50 kV/cm with a rise time of 3 ns in between plane electrodes separated by a gap of 4 mm. In results obtained in our simulations under similar conditions, we found runaway electrons with energies between ∼1.1 and ∼5.9 keV and associated X-rays with energies between ∼0.00125 and ∼4847 nJ. Comparison with Monte Carlo simulation results show that our approximation falls within factors ∼20 to ∼700 and our results show the same behavior as in the experiment. Note that the experimental set up was not well described, and both the uncertainty on the cathode and the detector response are not taken into account in our calculations. We have found that single streamer discharges produce significant amounts of X-rays when lowering the ambient air density and hence increasing the reduced electric field. The streamer model developed in this dissertation reproduces correctly the microphysics of the problem.

The notion of energy deposited by the streamer head in relation with the peak electric field was put forward. The value of this energy was estimated locally and around the streamer head to be respectively on the order of few microjoules in case of laboratory streamer discharges and on the order of tens of millijoules for sprite streamers simulated at 70 km altitude. This energy may serve as a reference to help understand deeper the processes of gas discharge experiments and the energy deposited by sprite streamers in the upper atmosphere. It is an important question to address in the framework of the impact of sprites in the upper atmospheric chemistry and maximum electric fields reached in streamers propagating in time varying external fields [Ihaddadene and Celestin, AGU poster presentation, AE33A-0473, 2015]. this energy scales with altitude. The energy deposited by one sprite streamer head scales as $\frac{N_0}{N}$.

The TARANIS space mission (CNES) will observe TLEs from a nadir-viewing geometry. The latter minimizes the atmospheric absorption, however it also involves poor vertical resolution. The missions ASIM (ESA) and GLIMS (JAXA) have also chosen this observation geometry. In this dissertation (Chapter 4), a spectrophotometric method based on the ratios of different $N_2$ bands systems produced by TLEs, Lyman-Birge-Hopfield (LBH), first positive bands system ($1PN_2$), second positive bands system ($2PN_2$), and first negative bands system ($1NN_2^+$) have been developed to estimate the altitude, the electric field, and the velocity of downward propagating sprites streamers in columniform sprites. Given uncertainties on some quenching coefficients, the proposed method would strongly benefit from joint campaigns associating ground and satellite measurements. This method is expected to increase the scientific return of numerous space missions such as TARANIS, ASIM, and GLIMS.

## 6.2 Suggestion for future work

The processes of the emission of energetic electrons and associated X-rays by laboratory gas discharges, lightning leaders, and thunderstorms are still under debate. The answers we have brought via the scientific work presented in this dissertation regarding the head-on-collisions between negative and positive streamers is a significant step in the understanding the microphysics of streamer discharges and their links to the production of runaway electrons and the associated X-rays. Our streamer model has reproduced experimental results, and has shown a good agreement with observations as well. Further simulation of head-on collisions in configurations such as point-to-point and point-to-plane electrodes would be very interesting. From the experimental side, a simple reproduction of the simulation results using controlled streamers associated with X-ray detection capabilities would be very interesting to understand how streamers produce X-rays and whether any other additional process, such as thermodynamical processes or cathode electron emissions, would be at play.

The energy deposited by laboratory streamer discharge, and sprite streamers discussed in this dissertation need to be carefully investigated and compared to experimental results and observations. The link between the energy deposited by

the streamer head and the peak electric field is an important point to understand the increase of the peak electric field under time varying external fields.

As we have already mentioned, head-on collisions between negative and positive streamers are sources of luminous optical patches and the related investigation on the associated larger time scale chemistry is of great importance. Estimation of the exact fraction of total volume occupied by streamers to the whole sprite volume is also an important quantity to quantify the correct energy value deposited by a sprite event.

The spectrophotometric method developed in this dissertation is of a great interest to satellite missions observing TLEs from a nadir-viewing geometry. Tests of its sensitivity to the quenching coefficients, to the model of the excited species, including chemistry and vibrational modes resolution is of great importance. It is also possible that other representations of the ratio-based parametric space would allow an easier use of the method.

# Appendices

# Appendix A

# Predictive-corrective time scheme and the FCT algorithm

In this appendix, we explicit the time steps applied to calculate the high order fluxes. Three schemes are considered in this work: Lax-Wendroff, Leapfrog-Trapezoidal, and Leapfrog-Adams-Multon [e.g., *Morrow*, 1981; *Dhali and Williams*, 1987; *Vitello et al.*, 1994; *Shchepetkin and McWilliams*, 1998].

**Lax-Wendroff**: $2^{nd}$ order accurate in time and space. We first transport using high order fluxes (separately from the FCT algorithm) the density $n_{\mathrm{e}}^{t}$ at time $t$ over $\frac{\delta t}{2}$ to make a prediction of the density at $t+\frac{\delta t}{2}$, then in the FCT we use the predicted density $n_{\mathrm{e}}^{t+\frac{\delta t}{2}}$ to recalculate the high order fluxes and to combine them with low order fluxes to deduce the final corrected density at a time $t+\delta t$.

Outside the FCT algorithm:

$n_{\mathrm{e}}^{t+\frac{\delta t}{2}} = n_{\mathrm{e}}^{t} - \frac{\delta t}{2dx}(\sum F^{H}(n_{\mathrm{e}}^{t}))$

In the FCT algorithm:

– Calculate the low order fluxes $F^{L}(n_{\mathrm{e}}^{t})$ (using upwind scheme)

– Calculate the diffused solution $n_{\mathrm{e}_{\mathrm{Diff}}}^{t+\delta t} = n_{\mathrm{e}}^{t} - \frac{\delta t}{dx}(\sum F^{L}(n_{\mathrm{e}}^{t}))$

– Calculate the high order fluxes $F^{H}(n_{\mathrm{e}}^{t+\frac{\delta t}{2}})$

– Calculate the anti-diffusive fluxes $A^{H-L} = F^{H}(n_{\mathrm{e}}^{t+\frac{dt}{2}}) - F^{L}(n_{\mathrm{e}}^{t})$

– Calculate the limiters and control the correct quantity of anti-diffusion to add to the diffused solution: $0 < C < 1$

– Finally deduce the density at $t + \delta t$

$n_{\mathrm{e}_{\mathrm{corrected}}}^{t+dt} = n_{\mathrm{e}_{\mathrm{Diff}}}^{t+\delta t} - \frac{\delta t}{dx}(\sum CA^{H-L})$

**Leapfrog-Trapezoidal**: $2^{nd}$ order accurate in time and space. We first transport using high order fluxes (separately from the FCT algorithm) the density $n_{\mathrm{e}}^{t-\delta t}$ at time $t - \delta t$ with $2\delta t$ to make a prediction of a density at $t + \delta t$.

Outside the FCT algorithm:

$n_{\mathrm{e}}^{t+\delta t} = n_{\mathrm{e}}^{t-\delta t} - \frac{2\delta t}{dx}(\sum F^H(n_{\mathrm{e}}^t))$ with an additional intermediate step: $n_{\mathrm{e}}^\star = \frac{n_{\mathrm{e}}^{t+\delta t} + n_{\mathrm{e}}^t}{2}$

In the FCT algorithm:

We use the predicted density $n_{\mathrm{e}}^\star$ to recalculate again the high order fluxes and to combine them with a low order fluxes to deduce the finale corrected density at a time $t + \delta t$ following the same steps described in Lax-Wendroff

– Calculate the low order fluxes $F^L(n_{\mathrm{e}}^t)$ (using upwind scheme)

– Calculate the diffused solution $n_{\mathrm{e}_{\mathrm{Diff}}}^{t+\delta t} = n_{\mathrm{e}}^t - \frac{\delta t}{dx}(\sum F^L(n_{\mathrm{e}}^t))$

– Calculate the high order fluxes $F^H(n_{\mathrm{e}}^\star)$

– Calculate the anti-diffusive fluxes $A^{H-L} = F^H(n_{\mathrm{e}}^\star) - F^L(n_{\mathrm{e}}^t)$

– Calculate the limiters and control the correct quantity of anti-diffusion to add to the diffused solution: $0 < C < 1$

– Finally deduce the density at $t + \delta t$

$n_{\mathrm{e}_{\mathrm{Corrected}}}^{t+\delta t} = n_{\mathrm{e}_{\mathrm{Diff}}}^{t} - \frac{\delta t}{dx}(\sum CA^{H-L})$

**Leapfrog-Adams-Multon**: $3^{rd}$ accurate in time and space. We first transport using high order fluxes (separately from the FCT algorithm) the density $n_{\mathrm{e}}^{t-\delta t}$ at time $t - \delta t$ with $2\delta t$ to make a prediction of a density at $t + \delta t$.

Outside the FCT algorithm:

$n_{\mathrm{e}}^{t+\delta t} = n_{\mathrm{e}}^{t-\delta t} - \frac{2\delta t}{dx}(\sum F^H(n_{\mathrm{e}}^t))$ with an additional intermediate step: $n_{\mathrm{e}}^\star = \frac{5n_{\mathrm{e}}^{t+\delta t} + 8n_{\mathrm{e}}^t - n_{\mathrm{e}}^{t-\delta t}}{12}$

In the FCT algorithm:

we use the predicted density $n_{\mathrm{e}}^\star$ to recalculate again the high order fluxes and to combine them with a low order fluxes to deduce the finale corrected density at a time $t + \delta t$ following the same steps

– Calculate the low order fluxes $F^L(n_{\mathrm{e}}^t)$ (using upwind scheme)

– Calculate the diffused solution $n_{\mathrm{e}_{\mathrm{Diff}}}^{t+\delta t} = n_{\mathrm{e}}^t - \frac{\delta t}{dx}(\sum F^L(n_{\mathrm{e}}^t))$

– Calculate the high order fluxes $F^H(n_e^\star)$

– Calculate the anti-diffusive fluxes $A^{H-L} = F^H(n_e^\star) - F^L(n_e^t)$

– Calculate the limiters and control the correct quantity of anti-diffusion to add to the diffused solution: $0 < C < 1$

– finally deduce the density at $t + \delta t$

$n_{e_{\text{Corrected}}}^{t+\delta t} = n_{e_{\text{Diff}}}^{t} - \frac{\delta t}{dx}(\sum C A^{H-L})$

We transported rectangular and Gaussian forms and conducted streamer simulations using the three above schemes and negligible differences have been noticed, hence in the present model we use the least time consuming scheme which is the Lax-Wendroff. A more detailed numerical study about the transport properties of these different schemes can also be found in [e.g., *Morrow*, 1981; *Shchepetkin and McWilliams*, 1998].

# Appendix B

# Side project: sprites detection from Orléans

In this appendix, we present some sprite observational results from the top roof of the LPC2E that we have obtained in the framework of a ground-observation of TLEs project. The primary aim of this project is to train students and researchers and to initiate to use (optical and electronic devices, trigger algorithms, image processing, etc.) tools and techniques required for the observation of TLEs and acquaint them to the related physics. We also try to quantify the local rate of the sprite production and to understand the link between the characteristics of causative lightning and their related morphology (carrot, columniform, or jelly fish).

To perform observations, we have used a Watec 902-H2 camera equipped with a Tamron 4-12 mm F 1.2 ASIR and combined with a GPS based time inserter IOTA-VTI v1.1.42 and triggered by UFO capture HD2 V4 20 software (*http* : *//sonotaco.com/e_index.html*) running in Windows 7 system. To set up sprite observations, we have used the Meteo france website to follow thunderstorms and directed the camera to given active zones. The sprite events have been observed from the LPC2E/CNRS, Orleans, France within a radius of ∼400 km, above Bourgogne, Basse Normandie, South of England, and Nante, and we have detected them in the following months, respectively: May, June, and September 2016.

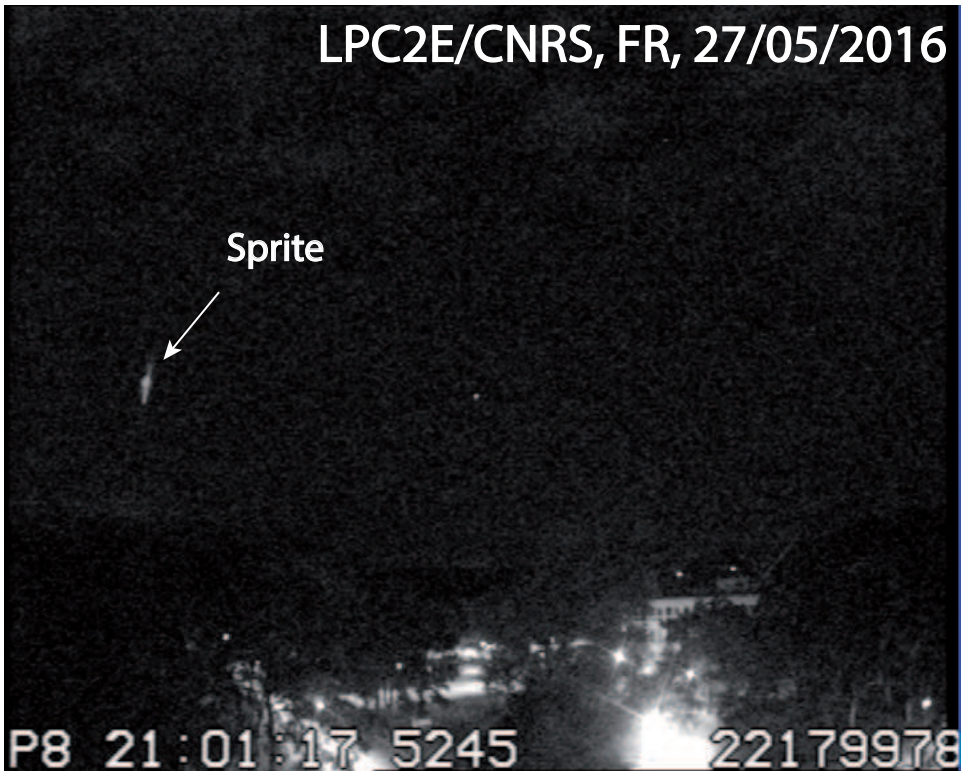


Figure B.1 – Carrot sprite event observed over Bourgogne, FR. The event is associated to a +CG lightning with a current of 18 kA.

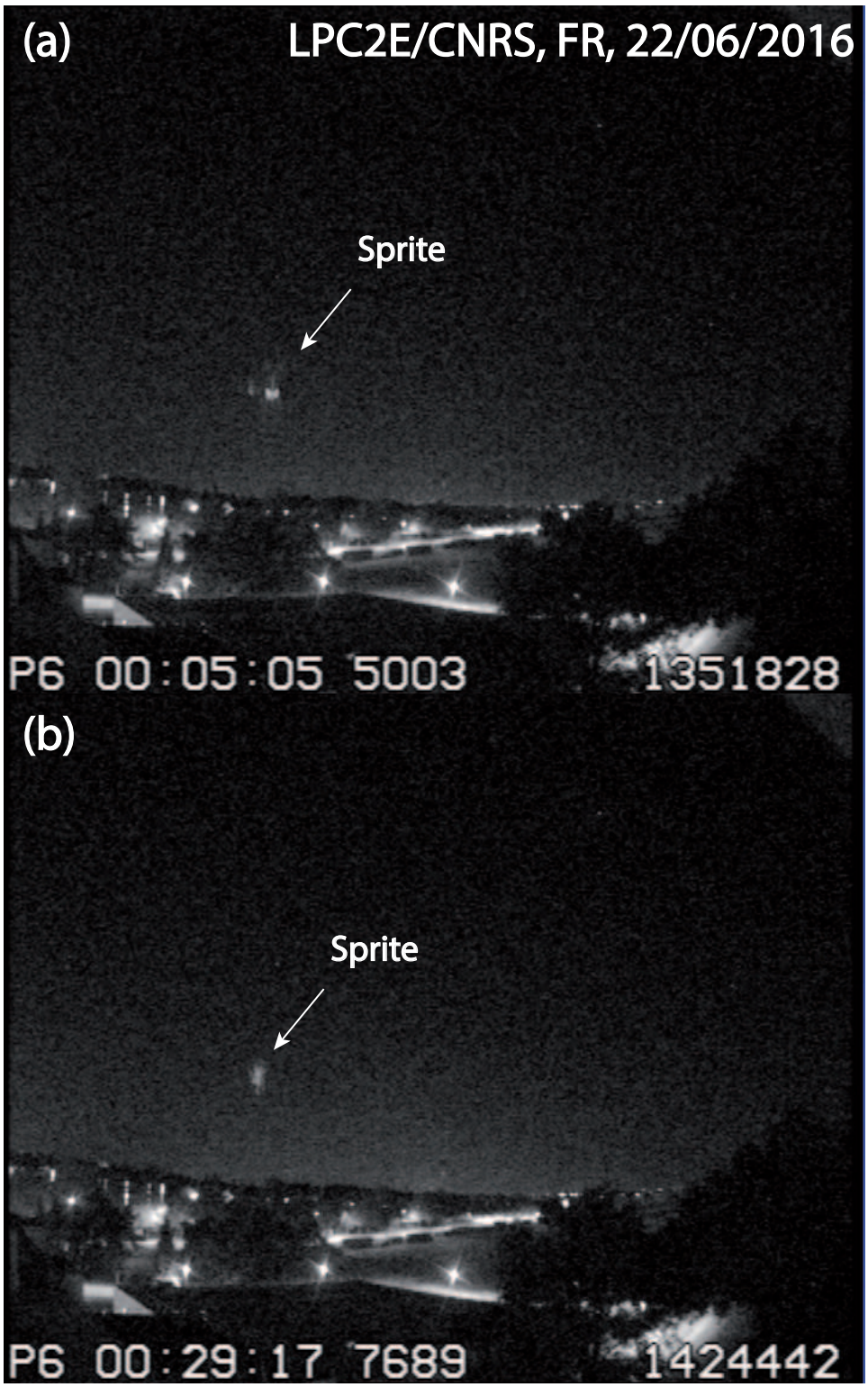


Figure B.2 – (a)-(b). Carrot sprite events observed over South England, UK. The events are associated to a +CG lightnings with currents of 104 kA (Lon.: -1.0433 Lat.: 50.4788) and 46 kA (Lon.: -1.0804 Lat.: 50.7523), respectively.

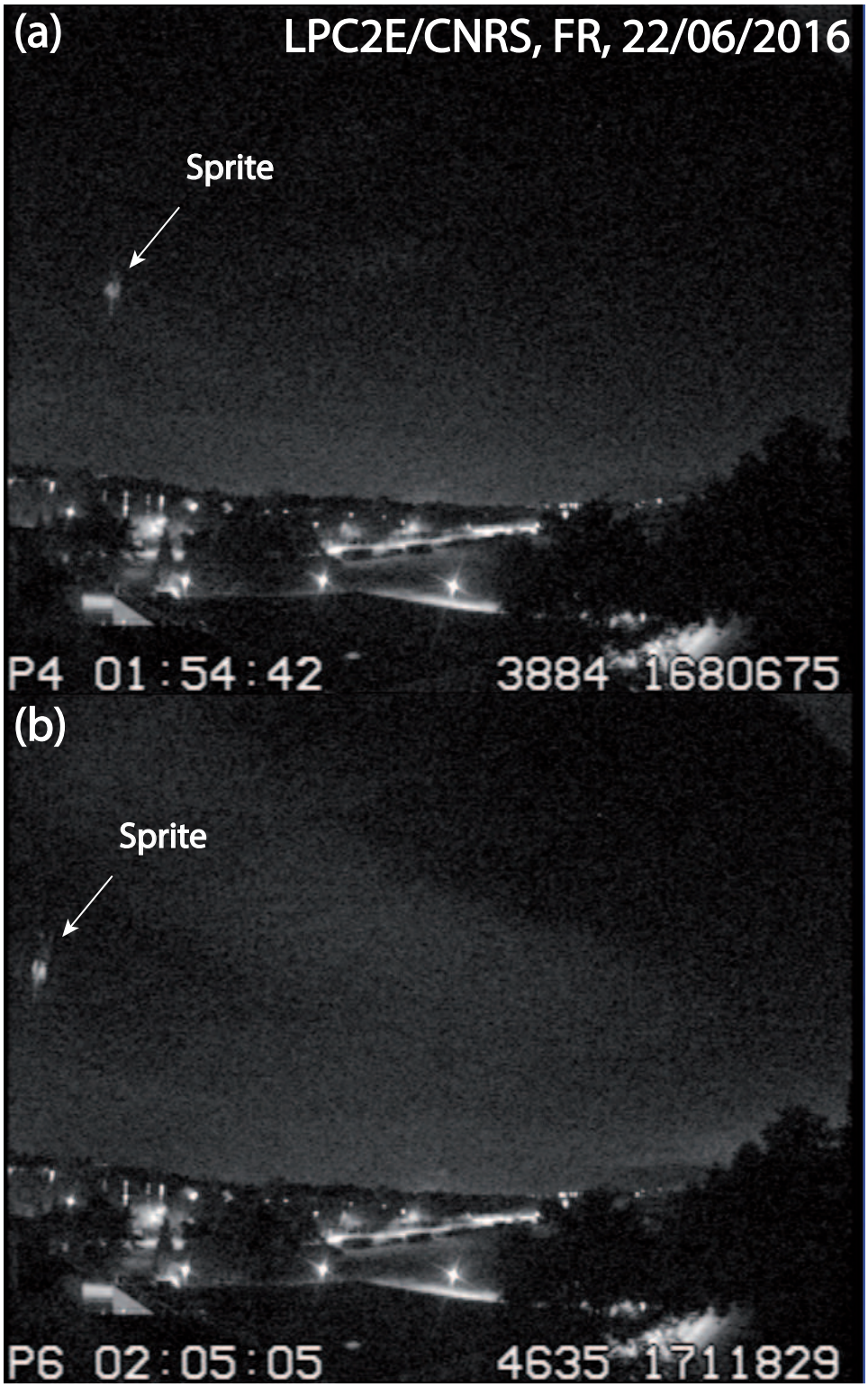


Figure B.3 – (a)-(b) Carrot sprite events observed over Basse Normandie, FR. The events are associated to a +CG lightnings with currents of 97 kA (Lon.: -0.4295 Lat.: 49.2948) and 27 kA (Lon.: -0.3179 Lat.: 48.8387), respectively.

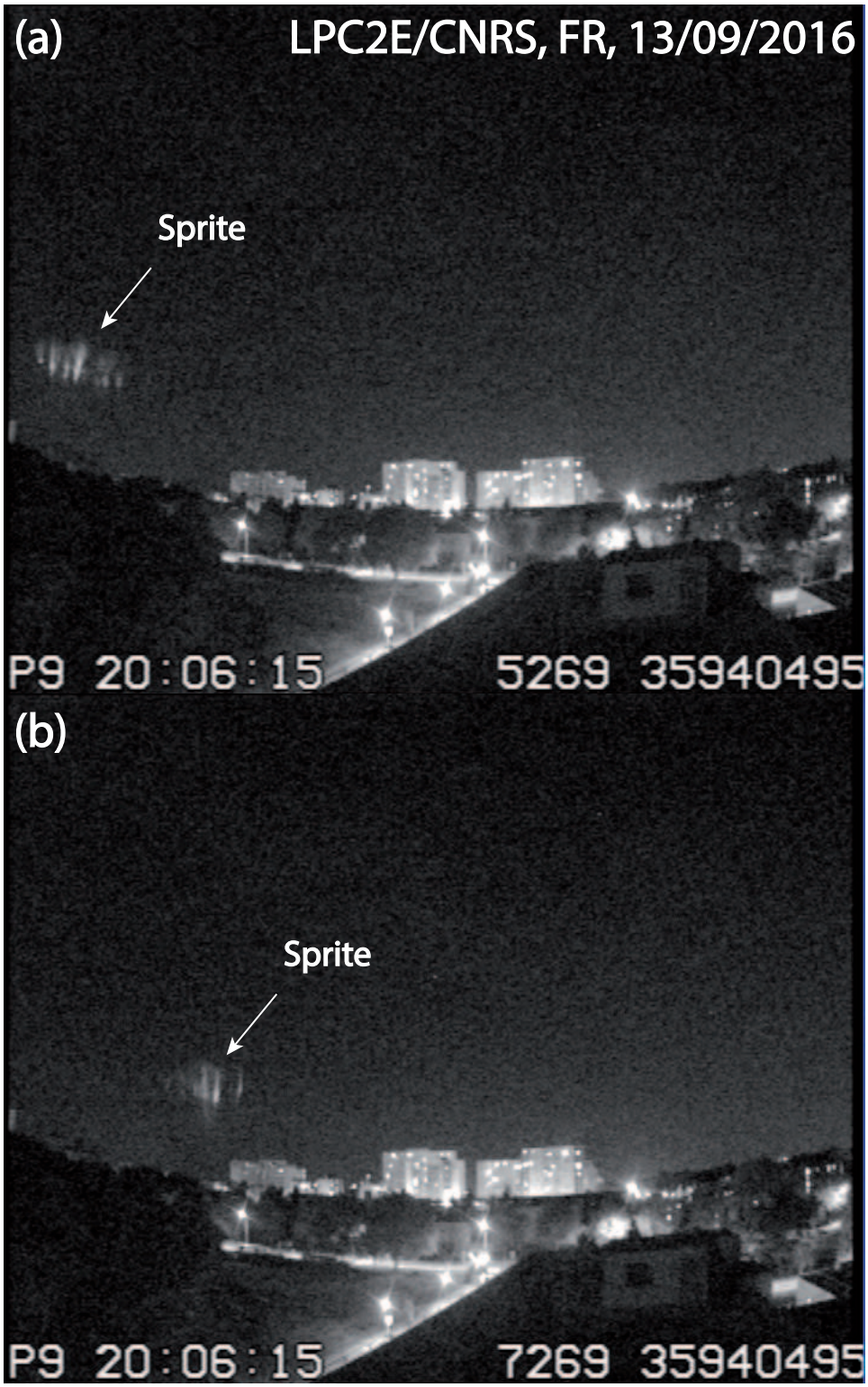


Figure B.4 – (a)-(b) Carrot sprite events observed off the coast of Ile de Ré, FR. The events are associated to a +CG lightning with a current of 139 kA (Lon.: 46.0790 Lat.: -2.2735).

## Acknowledgments

The project is funded by the French space agency (CNES) under the credit line name Sebastien Celestin Chair d'Excellence. Many thanks to all of the LPC2E contributors for their help and assistance to make this project a great success: Sebastien Celestin, Jean Louis Pinçon, Gilles Chalumeau, and Stéphane Chevrier. We also thank: Serge Soula (OMP Université de Toulouse, France), Torsten Neubert (DTU Space, Danemark), and Olivier Chanrion (DTU Space, Danemark) for their help in determining the lightning characteristics via Vaisala Global Lightning Dataset (GLD) 360, related to sprite events .

# Bibliography

Adachi, T., H. Fukunishi, Y. Takahashi, and M. Sato (2004), Roles of the EMP and QE field in the generation of columniform sprites, *Geophys. Res. Lett.*, *31*, L04107, doi:10.1029/2003GL019081.

Adachi, T., et al. (2006), Electric field transition between the diffuse and streamer regions of sprites estimated from ISUAL/array photometer measurements, *Geophys. Res. Lett.*, *33*, L17803, doi:10.1029/2006GL026495.

Aleksandrov, G. N. (1966), Mechanism of Corona-to-Spark Transition in Long Air Gaps, *Sov. Phys.-Tech. Phys.*, *10*, 948.

Armstrong, R. A., J. A. Shorter, M. J. Taylor, D. M. Suszcynsky, W. A. Lyons, and L. S. Jeong (1998), Photometric measurements in the SPRITES '95 '96 campaigns of nitrogen second positive (399.8 nm) and first negative (427.8 nm) emissions, *J. Atmos. Sol.-Terr. Phys.*, *60*, 787–799, doi:10.1016/S1364-6826(98)00026-1.

Babaeva, N. Y., and M. J. Kushner (2010), Intracellular electric fields produced by dielectric barrier discharge treatment of skin, *J. Phys. D: Appl. Phys.*, *43*(18), 185206, doi:10.1088/0022-3727/43/18/185206.

Babaeva, N. Y., and G. V. Naidis (1996a), Simulation of positive streamers in air in weak uniform electric fields, *Phys. Lett. A*, *215*, 187–190, doi:10.1016/0375-9601(96)00225-3.

Babaeva, N. Y., and G. V. Naidis (1996b), Two-dimensional modelling of positive streamer dynamics in non-uniform electric fields in air, *J. Phys. D: App. Phys.*, *29*, 2423–2431, doi:10.1088/0022-3727/29/9/029.

Babaeva, N. Y., and G. V. Naidis (1997), Dynamics of positive and negative streamers in air in weak uniform electric fields, *IEEE Trans. Plasma Sci.*, *25*, 375–379, doi:10.1109/27.602514.

Babich, L. P., and Y. L. Stankevich (1973), Transition from Streamers to Continuous Electron Acceleration, *Sov. Phys.-Tech. Phys.*, *17*, 1333.

Babich, L. P., E. I. Bochkov, I. M. Kutsyk, T. Neubert, and O. Chanrion (2015), A model for electric field enhancement in lightning leader tips to levels allowing X-and gamma ray emissions, *J. Geophys. Res.*, *120*, 5087–5100, doi: 10.1002/2014JA020923.

Blanc, E., T. Farges, R. Roche, D. Brebion, T. Hua, A. Labarthe, and V. Melnikov (2004), Nadir observations of sprites from the International Space Station, *J. Geophys. Res.*, *109*, A02306, doi:10.1029/2003JA009972.

Bonaventura, Z., A. Bourdon, S. Celestin, and V. P. Pasko (2011), Electric field determination in streamer discharges in air at atmospheric pressure, *Plasma Sources Sci. Technol.*, *20*(3), 035012, doi:10.1088/0963-0252/20/3/035012.

Boris, J. P., and D. L. Book (1973), Flux-Corrected Transport. I. SHASTA, A Fluid Transport Algorithm That Works, *J. Comput. Phys.*, *11*, 38–69, doi:10.1016/0021-9991(73)90147-2.

Borukhov, M. Y., I. K. Bek-Bulatov, L. L. Lukashevich, R. B. Nagaibekov, and N. Umurzakov (1973), Modelling of Field-Amplification Processes on Cathode Protuberances in Vaccum Arcs, *Sov. Phys.-Tech. Phys.*, *17*, 1199.

Bourdon, A., V. P. Pasko, N. Y. Liu, S. Célestin, P. Ségur, and E. Marode (2007), Efficient models for photoionization produced by non-thermal gas discharges in air based on radiative transfer and the Helmholtz equations, *Plasma Sources Sci. Technol.*, *16*, 656–678, doi:10.1088/0963-0252/16/3/026.

Bucsela, E., J. Morrill, M. Heavner, C. Siefring, S. Berg, D. Hampton, D. Moudry, E. Wescott, and D. Sentman (2003), $N_2(B^3\Pi_g)$ and $N_2{}^+(A^2\Pi_u)$ vibrational distributions observed in sprites, *J. Atmos. Sol.-Terr. Phys.*, *65*, 583–590, doi: 10.1016/S1364-6826(02)00316-4.

Bugaev, S. P., E. A. Litvinov, G. A. Mesyats, and D. I. Proskurovskiĭ (1975), REVIEWS OF TOPICAL PROBLEMS: Explosive emission of electrons, *Sov. Phys. Usp.*, *18*, 51–61, doi:10.1070/PU1975v018n01ABEH004693.

Celestin, S., and V. P. Pasko (2010), Effects of spatial non-uniformity of streamer discharges on spectroscopic diagnostics of peak electric fields in transient luminous events, *Geophys. Res. Lett.*, *37*, L07804, doi:10.1029/2010GL042675.

Celestin, S., and V. P. Pasko (2011), Energy and fluxes of thermal runaway electrons produced by exponential growth of streamers during the stepping of lightning leaders and in transient luminous events, *J. Geophys. Res.*, *116*, A03315, doi:10.1029/2010JA016260.

Chen, A. B., et al. (2008), Global distributions and occurrence rates of transient luminous events, *J. Geophys. Res.*, *113*, A08306, doi:10.1029/2008JA013101.

COESA (1976), *US Standard Atmosphere, 1976, U.S. Government Printing Office, Washington, D.C.*

Cooray, V., L. Arevalo, M. Rahman, J. Dwyer, and H. Rassoul (2009), On the possible origin of X-rays in long laboratory sparks, *J. Atmos. Sol.-Terr. Phys.*, *71*, 1890–1898, doi:10.1016/j.jastp.2009.07.010.

Cooray, V., J. Dwyer, V. Rakov, and M. Rahman (2010), On the mechanism of X-ray production by dart leaders of lightning flashes, *J. Atmos. Sol.-Terr. Phys.*, *72*, 848–855, doi:10.1016/j.jastp.2010.04.006.

Cummer, S. A., N. Jaugey, J. Li, W. A. Lyons, T. E. Nelson, and E. A. Gerken (2006), Submillisecond imaging of sprite development and structure, *Geophys. Res. Lett.*, *33*, L04104, doi:10.1029/2005GL024969.

Demmel, J. (1996), Solving the Discrete Poisson Equation using Jacobi, SOR, Conjugate Gradients, and the FFT, *https://people.eecs.berkeley.edu/ demmel/cs267/lecture24/lecture24.html*.

Dhali, S. K., and P. F. Williams (1985), Numerical simulation of streamer propagation in nitrogen at atmospheric pressure, *Phys. Rev. A*, *31*, 1219–1221, doi:10.1103/PhysRevA.31.1219.

Dhali, S. K., and P. F. Williams (1987), Two-dimensional studies of streamers in gases, *J. Appl. Phys.*, *62*, 4696–4707, doi:10.1063/1.339020.

Duten, X., M. Redolfi, N. Aggadi, A. Vega, and K. Hassouni (2011), Spatial and temporal evolutions of ozone in a nanosecond pulse corona discharge at atmospheric pressure, *J. Phys. D: Appl. Phys.*, *44*, 415202, doi:10.1088/0022-3727/44/41/415202.

Dwyer, J. R. (2004), Implications of x-ray emission from lightning, *Geophys. Res. Lett*, *31*, L12102, doi:10.1029/2004GL019795.

Dwyer, J. R., et al. (2003), Energetic Radiation Produced During Rocket-Triggered Lightning, *Science*, *299*, 694–697, doi:10.1126/science.1078940.

Dwyer, J. R., H. K. Rassoul, Z. Saleh, M. A. Uman, J. Jerauld, and J. A. Plumer (2005), X-ray bursts produced by laboratory sparks in air, *Geophys. Res. Lett.*, *32*, L20809, doi:10.1029/2005GL024027.

Dwyer, J. R., Z. saleh, H. K. Rassoul, D. Concha, M. Rahman, V. Corray, J. Jerauld, M. A. Uman, and V. A. Rakov (2008), A study of X-ray emission from laboratory sparks in air at atmospheric pressure , *J. Geophys. Res.*, *113*, D23207, doi:10.1029/2008JD010315.

Dwyer, J. R., M. Schaal, H. K. Rassoul, M. A. Uman, D. M. Jordan, and D. Hill (2011), High-speed X-ray images of triggered lightning dart leaders, *J. Geophys. Res.*, *116*, D20208, doi:10.1029/2011JD015973.

D'yakonov, M. I., and V. Y. Kachorovskii (1989), Streamer discharge in a homogeneous field, *Zh. Eksp. Teor. Fiz.*, *95*.

Eastes, R. W. (2000), Modeling the $n_2$ lyman-birge-hopfield bands in the dayglow: Including radiative and collisional cascading between the singlet states, *J. Geophys. Res.*, *105*(A8), 18,557–18,573, doi:10.1029/1999JA000378.

Franz, R. C., R. J. Nemzek, and J. R. Winckler (1990), Television Image of a Large Upward Electrical Discharge Above a Thunderstorm System, *Science*, *249*, 48–51, doi:10.1126/science.249.4964.48.

Gardner, C. S., and J. D. Shelton (1985), Density response of neutral atmospheric layers to gravity wave perturbations, *J. Geophys. Res.*, *90*, 1745–1754, doi:10.1029/JA090iA02p01745.

Garipov, G. K., et al. (2013), Global transients in ultraviolet and red-infrared ranges from data of Universitetsky-Tatiana-2 satellite, *J. Geophys. Res.*, *118*, 370–379, doi:10.1029/2012JD017501.

Gerken, E. A., U. S. Inan, and C. P. Barrington-Leigh (2000), Telescopic imaging of sprites, *Geophys. Res. Lett.*, *27*, 2637–2640, doi:10.1029/2000GL000035.

Gordillo-Vázquez, F. J. (2010), Vibrational kinetics of air plasmas induced by sprites, *J. Geophys. Res.*, *115*, A00E25, doi:10.1029/2009JA014688.

Gordillo-Vázquez, F. J., A. Luque, and M. Simek (2011), Spectrum of sprite halos, *J. Geophys. Res.*, *116*, A09319, doi:10.1029/2011JA016652.

Gordillo-Vázquez, F. J., A. Luque, and M. Simek (2012), Near infrared and ultraviolet spectra of TLEs, *J. Geophys. Res.*, *117*, A05329, doi:10.1029/2012JA017516.

Green, B. D., et al. (1996), Molecular excitation in sprites, *Geophys. Res. Lett.*, *23*, 2161–2164, doi:10.1029/96GL02071.

Gurevich, V. V. (1961), On the theory of runaway electrons, *Sov. Phys. JETP*, *12*, 904.

Hale, L. C. (1994), Coupling of ELF/ULF energy from lightning and MeV particles to the middle atmosphere, inosphere, and global circuit, *J. Geophys. Res.*, *99*, 21, doi:10.1029/94JD00357.

Hampton, D. L., M. J. Heavner, E. M. Wescott, and D. D. Sentman (1996), Optical spectral characteristics of sprites, *Geophys. Res. Lett.*, *23*, 89–92, doi: 10.1029/95GL03587.

Heavner, M. J., J. S. Morrill, C. Siefring, D. D. Sentman, D. R. Moudry, E. M. Wescott, and E. J. Bucsela (2010), Near-ultraviolet and blue spectral observations of sprites in the 320-460 nm region: $N_2$ (2PG) emissions, *J. Geophys. Res.*, *115*, A00E44, doi:10.1029/2009JA014858.

Howard, J., M. A. Uman, J. R. Dwyer, D. Hill, C. Biagi, Z. Saleh, J. Jerauld, and H. K. Rassoul (2008), Co-location of lightning leader x-ray and electric field change sources, *Geophys. Res. Lett.*, *35*, L13817, doi:10.1029/2008GL034134.

Hu, W., S. A. Cummer, and W. A. Lyons (2007), Testing sprite initiation theory using lightning measurements and modeled electromagnetic fields, *J. Geophys. Res.*, *112*, D13115, doi:10.1029/2006JD007939.

ICRU Report 37 (1984), Stopping power for electrons and positrons, *International Commission on Radiation Units and measurements*, *37*.

Ihaddadene, M. A., and S. Celestin (2015), Increase of the electric field in head-on collisions between negative and positive streamers, *Geophys. Res. Lett.*, *42*, 5644–5651, doi:10.1002/2015GL064623.

Ihaddadene, M. A., and S. Celestin (2016), Determination of Sprite Streamers Altitude Based on $N_2$ Spectroscopic Analysis, *Accepted for a publication in J. Geophys. Res.*, doi:10.1002/2016JA023111.

Kadowaki, K., and I. Kitani (2010), Physics and Application of Streamer Discharge Produced by Polarity-Reversed Voltage Pulse for Environmental Protection Technology, *IEEJ Transactions on Fundamentals and Materials*, *130*, 871–878, doi:10.1541/ieejfms.130.871.

Kanmae, T., H. C. Stenbaek-Nielsen, and M. G. McHarg (2007), Altitude resolved sprite spectra with 3 ms temporal resolution, *Geophys. Res. Lett.*, *34*, L07810, doi:10.1029/2006GL028608.

Kanmae, T., H. C. Stenbaek-Nielsen, M. G. McHarg, and R. K. Haaland (2010a), Observation of blue sprite spectra at 10,000 fps, *Geophys. Res. Lett.*, *37*, L13808, doi:10.1029/2010GL043739.

Kanmae, T., H. C. Stenbaek-Nielsen, M. G. McHarg, and R. K. Haaland (2010b), Observation of sprite streamer head's spectra at 10,000 fps, *J. Geophys. Res.*, *115*, A00E48, doi:10.1029/2009JA014546.

Kochkin, P., A. P. J. van Deursen, A. de Boer, M. Bardet, and J.-F. Boissin (2015a), In-flight measurements of energetic radiation from lightning and thunderclouds, *J. Phys. D: Appl. Phys.*, *48*, 425202, doi:10.1088/0022-3727/48/42/425202.

Kochkin, P. O., C. V. Nguyen, A. P. J. van Deursen, and U. Ebert (2012), Experimental study of hard x-rays emitted from metre-scale positive discharges in air, *J. Phys. D: Appl. Phys.*, *45*, 425202, doi:10.1088/0022-3727/45/42/425202.

Kochkin, P. O., A. P. J. van Deursen, and U. Ebert (2014), Experimental study of spatio-temporal development of metre-scale negative discharges in air, *J. Phys. D: Appl. Phys.*, *47*, 145203, doi:10.1088/0022-3727/47/14/145203.

Kochkin, P. O., A. P. J. van Deursen, and U. Ebert (2015b), Experimental study on hard x-rays emitted from metre-scale negative discharges in air, *J. Phys. D: Appl. Phys.*, *48*(2), 025205, doi:10.1088/0022-3727/48/2/025205.

Kosar, B. C., N. Liu, and H. K. Rassoul (2012), Luminosity and propagation characteristics of sprite streamers initiated from small ionospheric disturbances at subbreakdown conditions, *J. Geophys. Res.*, *117*, A08328, doi:10.1029/2012JA017632.

Kossyi, I. A., A. Y. Kostinsky, A. A. Matveyev, and V. P. Silakov (1992), Kinetic scheme of the non-equilibrium discharge in nitrogen-oxygen mixtures, *Plasma Sources Sci. Technol.*, *1*, 207–220, doi:10.1088/0963-0252/1/3/011.

Kremnev, V. V., and Y. A. Kurbatov (1972), X-Rays from a Gas Discharge in a Strong Electric Field, *Sov. Phys.-Tech. Phys.*, *17*, 626.

Kulikovsky, A. A. (1997), Positive streamer between parallel plate electrodes in atmospheric pressure air, *J. Phys. D: Appl. Phys.*, *30*, 441–450, doi:10.1088/0022-3727/30/3/017.

Kunhardt, E. E., and C. Wu (1987), Towards a More Accurate Flux Corrected Transport Algorithm, *J. Comput. Phys.*, *68*, 127–150, doi:10.1016/0021-9991(87)90048-9.

Kuo, C.-L., R. R. Hsu, A. B. Chen, H. T. Su, L. C. Lee, S. B. Mende, H. U. Frey, H. Fukunishi, and Y. Takahashi (2005), Electric fields and electron energies inferred from the ISUAL recorded sprites, *Geophys. Res. Lett.*, *32*, L19103, doi:10.1029/2005GL023389.

Kuo, C. L., et al. (2008), Radiative emission and energy deposition in transient luminous events, *J. Phys. D: Appl. Phys.*, *41*(23), 234014, doi:10.1088/0022-3727/41/23/234014.

Kuo, C.-L., et al. (2009), Discharge processes, electric field, and electron energy in ISUAL-recorded gigantic jets, *J. Geophys. Res.*, *114*, A04314, doi:10.1029/2008JA013791.

Kuzmin, D., R. Löhner, and S. Turek (2012), *Flux-Corrected Transport*, doi:10.1007/978-94-007-4038-9.

Lefeuvre, F., E. Blanc, J.-L. Pinçon, R. Roussel-Dupré, D. Lawrence, J.-A. Sauvaud, J.-L. Rauch, H. de Feraudy, and D. Lagoutte (2008), TARANIS A Satellite Project Dedicated to the Physics of TLEs and TGFs, *Space Sci. Rev.*, *137*, 301–315, doi:10.1007/s11214-008-9414-4.

Lehtinen, N. G. (2000), Relativistic runaway electrons above thunderstorms, Ph.D. thesis, Standford University.

Li, J., and S. A. Cummer (2009), Measurement of sprite streamer acceleration and deceleration, *Geophys. Res. Lett.*, *36*, L10812, doi:10.1029/2009GL037581.

Li, J., S. A. Cummer, W. A. Lyons, and T. E. Nelson (2008), Coordinated analysis of delayed sprites with high-speed images and remote electromagnetic fields, *J. Geophys. Res.*, *113*, D20206, doi:10.1029/2008JD010008.

Litvinov, E. A., G. A. Mesyats, and D. I. Proskurovskiĭ (1983), REVIEWS OF TOPICAL PROBLEMS: Field emission and explosive electron emission processes in vacuum discharges, *Sov. Phys. Usp.*, *26*, 265–302, doi:10.1070/PU1983v026n02ABEH004322.

Liu, N. (2006), Dynamics of positive and negative streamers in sprites, Ph.D. thesis, The Pennsylvania State University.

Liu, N. (2010), Model of sprite luminous trail caused by increasing streamer current, *Geophy. Res. Lett.*, *37*, L04102, doi:10.1029/2009GL042214.

Liu, N., and V. P. Pasko (2004), Effects of photoionization on propagation and branching of positive and negative streamers in sprites, *J. Geophy. Res.*, *109*, A04301, doi:10.1029/2003JA010064.

Liu, N., and V. P. Pasko (2005), Molecular nitrogen LBH band system far-UV emissions of sprite streamers, *Geophys. Res. Lett.*, *32*, L05104, doi: 10.1029/2004GL022001.

Liu, N., and V. P. Pasko (2006), Effects of photoionization on similarity properties of streamers at various pressures in air, *J. Phys. D: Appl. Phys.*, *39*, 327–334, doi:10.1088/0022-3727/39/2/013.

Liu, N., et al. (2006), Comparison of results from sprite streamer modeling with spectrophotometric measurements by ISUAL instrument on FORMOSAT-2 satellite, *Geophys. Res. Lett.*, *33*, L01101, doi:10.1029/2005GL024243.

Liu, N., V. P. Pasko, H. U. Frey, S. B. Mende, H.-T. Su, A. B. Chen, R.-R. Hsu, and L.-C. Lee (2009a), Assessment of sprite initiating electric fields and quenching altitude of $a^1\Pi_g$ state of $N_2$ using sprite streamer modeling and ISUAL spectrophotometric measurements, *J. Geophys. Res.*, *114*, A00E02, doi: 10.1029/2008JA013735.

Liu, N., J. R. Dwyer, H. C. Stenbaek-Nielsen, and M. G. McHarg (2015), Sprite streamer initiation from natural mesospheric structures, *Nat. Commun.*, *6*, 7540, doi:10.1038/ncomms8540.

Liu, N., L. D. Boggs, and S. A. Cummer (2016), Observation-constrained modeling of the ionospheric impact of negative sprites, *Geophys. Res. Lett.*, *43*, 2365–2373, doi:10.1002/2016GL068256.

Liu, N. Y., V. P. Pasko, K. Adams, H. C. Stenbaek-Nielsen, and M. G. McHarg (2009b), Comparison of acceleration, expansion, and brightness of sprite streamers obtained from modeling and high-speed video observations, *J. Geophys. Res.*, *114*, A00E03, doi:10.1029/2008JA013720.

Lu, X., G. V. Naidis, M. Laroussi, and K. Ostrikov (2014), Guided ionization waves: Theory and experiments, *Phys. Rep.*, *540*, 123–166, doi: 10.1016/j.physrep.2014.02.006.

Luque, A., and F. J. Gordillo-Vasquesz (2011), Sprite beads originating from inhomogeneities in the mesospheric electron density, *Geophy. Res. Lett.*, *38*, L04808, doi:10.1029/2010GL046403.

March, V., and J. Montanyà (2010), Influence of the voltage-time derivative in X-ray emission from laboratory sparks, *Geophys. Res. Lett.*, *37*, L19801, doi: 10.1029/2010GL044543.

March, V., and J. Montanyà (2011), X-rays from laboratory sparks in air: The role of the cathode in the production of runaway electrons, *Geophys. Res. Lett.*, *38*, L04803, doi:10.1029/2010GL046540.

Mende, S. B., R. L. Rairden, G. R. Swenson, and W. A. Lyons (1995), Sprite spectra; $N_2$ 1 PG band identification, *Geophys. Res. Lett.*, *22*, 2633–2636, doi: 10.1029/95GL02827.

Mesyats, G. A., and Y. I. Bychkov (1968), Statistical Study of Nanosecond Breakdown Delay in Narrow Gas Gaps in Superhigh Electric Fields, *Sov. Phys.-Tech. Phys.*, *12*, 1258.

Mesyats, G. A., Y. I. Bychkov, and V. V. Kremnev (1972), Pulsed Nanosecond Electric Discharges in Air, *Usp. Fiz. Nauk.*, *107*, 201–228.

Milikh, G., J. A. Valdivia, and K. Papadopoulos (1998), Spectrum of red sprites, *J. Atmos. Sol.-Terr. Phys.*, *60*, 907–915, doi:10.1016/S1364-6826(98)00032-7.

Mitchell, K. B. (1970), Fluorescence Efficiencies and Collisional Deactivation Rates for $N_2$ and $N^+{}_2$ Bands Excited by Soft X Rays, *J. Chem. Phys.*, *53*, 1795–1802, doi:10.1063/1.1674257.

Moore, C. B., K. B. Eack, G. D. Aulich, and W. Rison (2001), Energetic radiation associated with lightning stepped-leaders, *Geophys. Res. Lett.*, *28*, 2141–2144.

Morrill, J., et al. (2002), Electron energy and electric field estimates in sprites derived from ionized and neutral $N_2$ emissions, *Geophys. Res. Lett.*, *29*, 1462, doi:10.1029/2001GL014018.

Morrill, J. S., E. J. Bucsela, V. P. Pasko, S. L. Berg, M. J. Heavner, D. R. Moudry, W. M. Benesch, E. M. Wescott, and D. D. Sentman (1998), Time resolved $N_2$

triplet state vibrational populations and emissions associated with red sprites, *J. Atmos. Sol.-Terr. Phys.*, *60*, 811–829, doi:10.1016/S1364-6826(98)00031-5.

Morrow, R. (1981), Numerical Solution of Hyperbolic Equations for Electron Drift in Strongly Non-Uniform Electric Fields, *J. Comput. Phys.*, *43*, 1–15, doi:10.1016/0021-9991(81)90108-X.

Morrow, R., and L. E. Cram (1985), Flux-Corrected Transport and Diffusion on a Non-uniform Mesh, *J. Comput. Phys.*, *57*, 129–136, doi:10.1016/0021-9991(85)90055-5.

Morrow, R., and J. J. Lowke (1997), Streamer propagation in air, *J. Phys. D: Appl. Phys.*, *30*, 614–627, doi:10.1088/0022-3727/30/4/017.

Moss, G. D., V. P. Pasko, N. Liu, and G. Veronis (2006), Monte Carlo model for analysis of thermal runaway electrons in streamer tips in transient luminous events and streamer zones of lightning leaders, *J. Geophys. Res.*, *111*, A02307.

Neubert, T. (2009), ASIM an Instrument Suite for the International Space Station, in *American Inst. Phys. Conf. Series*, vol. 1118, pp. 8–12, doi:10.1063/1.3137718.

Nguyen, C. V., A. P. J. van Deursen, and U. Ebert (2008), Multiple x-ray bursts from long discharges in air, *J. Phys. D: Appl. Phys.*, *41*(23), 234012, doi:10.1088/0022-3727/41/23/234012.

Nguyen, C. V., A. P. J. van Deursen, E. J. M. van Heesch, G. J. J. Winands, and A. J. M. Pemen (2010), X-ray emission in streamer-corona plasma, *J. Phys. D: Appl. Phys.*, *43*(2), 025202, doi:10.1088/0022-3727/43/2/025202.

Pai, D. Z., D. A. Lacoste, and C. O. Laux (2010), Transitions between corona, glow, and spark regimes of nanosecond repetitively pulsed discharges in air at atmospheric pressure, *J. App. Phys.*, *107*(9), 093,303, doi:10.1063/1.3309758.

Pancheshnyi, S. V., S. M. Starikovskaia, and A. Y. Starikovskii (1998), Measurements of rate constants of the $N_2$( $C^3\Pi_u$, v'=0) and $N_2^+$( $B^2\Sigma^+{}_u$, v'=0) deactivation by $N_2$, $O_2$, $H_2$, CO and $H_2O$ molecules in afterglow of the nanosecond discharge, *Chem. Phys. Lett.*, *294*, 523–527, doi:10.1016/S0009-2614(98)00879-3.

Pasko, V. P. (2006), *Theoretical modeling of sprites and jets, in Sprites, Elves and Intense Lightning Discharges, NATO Science Series II: Mathematics, Physics and Chemistry.*

Pasko, V. P. (2007), Red sprite discharges in the atmosphere at high altitude: the molecular physics and the similarity with laboratory discharges, *Plasma Sources Sci. Technol.*, *16*, S13–S29, doi:10.1088/0963-0252/16/1/S02.

Pasko, V. P., U. S. Inan, T. F. Bell, and Y. N. Taranenko (1997), Sprites produced by quasi-electrostatic heating and ionization in the lower ionosphere, *J. Geophys. Res.*, *102*, 4529–4562, doi:10.1029/96JA03528.

Pasko, V. P., U. S. Inan, and T. F. Bell (1998), Spatial structure of sprites, *Geophys. Res. Lett.*, *25*, 2123–2126, doi:10.1029/98GL01242.

Pasko, V. P., Y. Yair, and C.-L. Kuo (2012), Lightning Related Transient Luminous Events at High Altitude in the Earth's Atmosphere: Phenomenology, Mechanisms and Effects, *Space. Sci. Rev.*, *168*, 475–516, doi:10.1007/s11214-011-9813-9.

Pasko, V. P., J. Qin, and S. Celestin (2013), Toward Better Understanding of Sprite Streamers: Initiation, Morphology, and Polarity Asymmetry, *Surv. Geophys.*, *34*, 797–830, doi:10.1007/s10712-013-9246-y.

Qin, J. (2013), Numerical modeling of the inception, morphology and radio signals of sprites produced by lightning discharges with positive and negative polarity, Ph.D. thesis, The Pennsylvania State University.

Qin, J., and V. P. Pasko (2014), On the propagation of streamers in electrical discharges, *J. Phys. D: Appl. Phys.*, *47*, 435202, doi:10.1088/0022-3727/47/43/435202.

Qin, J., and V. P. Pasko (2015), Dynamics of sprite streamers in varying air density, *Geophys. Res. Lett.*, *42*, 2031–2036, doi:10.1002/2015GL063269.

Qin, J., S. Celestin, and V. P. Pasko (2012), Low frequency electromagnetic radiation from sprite streamers, *Geophys. Res. Lett.*, *39*, L22803, doi:10.1029/2012GL053991.

Qin, J., S. Celestin, V. P. Pasko, S. A. Cummer, M. G. McHarg, and H. C. Stenbaek-Nielsen (2013a), Mechanism of column and carrot sprites derived from optical and radio observations, *Geophys. Res. Lett.*, *40*, 4777–4782, doi:10.1002/grl.50910.

Qin, J., S. Celestin, and V. P. Pasko (2013b), Dependence of positive and negative sprite morphology on lightning characteristics and upper atmospheric ambient conditions, *J. Geophys. Res.*, *118*, 2623–2638, doi:10.1029/2012JA017908.

Qin, J., V. P. Pasko, M. G. McHarg, and H. C. Stenbaek-Nielsen (2014), Plasma irregularities in the D-region ionosphere in association with sprite streamer initiation, *Nat. Commun.*, *5*, 3740, doi:10.1038/ncomms4740.

Rahman, M., V. Cooray, N. Azlinda Ahmad, J. Nyberg, V. A. Rakov, and S. Sharma (2008), X rays from 80-cm long sparks in air, *Geophys. Res. Lett.*, *35*, 6805, doi:10.1029/2007GL032678.

Raizer, Y. P. (1991), *Gas Discharge Physics*.

Saleh, Z., et al. (2009), Properties of the X-ray emission from rocket-triggered lightning as measured by the Thunderstorm Energetic Radiation Array (TERA), *J. Geophys. Res.*, *114*, D17210, doi:10.1029/2008JD011618.

Sato, M., Y. Takahashi, M. Kikuchi, S. Makoto, A. Yamazaki, and T. Ushio (2011), Lightning and sprite imager (lsi) onboard jem-glims, *IEEJ Trans. FM*, *131*, 994–999.

Sato, M., et al. (2015), Overview and early results of the global lightning and sprite measurements mission, *J. Geophys. Res.*, *120*(9), 3822–3851, doi:10.1002/2014JD022428, 2014JD022428.

Schaal, M. M., J. R. Dwyer, Z. H. Saleh, H. K. Rassoul, J. D. Hill, D. M. Jordan, and M. A. Uman (2012), Spatial and energy distributions of X-ray emissions from leaders in natural and rocket triggered lightning, *J. Geophys. Res.*, *117*, D15201, doi:10.1029/2012JD017897.

Schaal, M. M., et al. (2014), The structure of X-ray emissions from triggered lightning leaders measured by a pinhole-type X-ray camera, *J. Geophys. Res.*, *119*, D020266, doi:10.1002/2013JD020266.

Schafer, M. (2006), *Computational enginnering-Introduction to numerical mehods.*

Shchepetkin, A. F., and J. C. McWilliams (1998), Quasi-Monotone Advection Schemes Based on Explicit Locally Adaptive Dissipation, *Monthly Weather Review*, *126*, 1541, doi:10.1175/1520-0493(1998)126¡1541:QMASBO¿2.0.CO;2.

Siefring, C. L., J. S. Morrill, D. D. Sentman, and M. J. Heavner (2010), Simultaneous near-infrared and visible observations of sprites and acoustic-gravity waves during the EXL98 campaign, *J. Geophys. Res.*, *115*, A00E57, doi:10.1029/2009JA014862.

Stankevich, Y. L. (1971), Initial Stage of an Electrical Discharge in a Dense Gas, *Sov. Phys.-Tech. Phys.*, *15*, 1138.

Stankevich, Y. L., and V. G. Kalinin (1968), Fast Electrons and X-Ray Radiation During the Initial Stage Growth of a Pulsed Spark Discharge in Air, *Sov. Phys. Dokl.*, *20*, 1042.

Stanley, M., P. Krehbiel, M. Brook, C. Moore, W. Rison, and B. Abrahams (1999), High speed video of initial sprite development, *Geophys. Res. Lett.*, *26*, 3201–3204, doi:10.1029/1999GL010673.

Starikovskaia, S. M. (2014), Plasma-assisted ignition and combustion: nanosecond discharges and development of kinetic mechanisms, *J. Phy. D: Appl. Phy.*, *47*, 353001, doi:10.1088/0022-3727/47/35/353001.

Stenbaek-Nielsen, H. C., and M. G. McHarg (2008), High time-resolution sprite imaging: observations and implications, *J. Phys. D: Appl. Phys.*, *41*(23), 234009, doi:10.1088/0022-3727/41/23/234009.

Stenbaek-Nielsen, H. C., D. R. Moudry, E. M. Wescott, D. D. Sentman, and F. T. S. Sabbas (2000), Sprites and possible mesospheric effects, *Geophys. Res. Lett.*, *27*, 3829–3832, doi:10.1029/2000GL003827.

Stenbaek-Nielsen, H. C., T. Kanmae, M. G. McHarg, and R. Haaland (2013), High-Speed Observations of Sprite Streamers, *Surv. Geophys.*, *34*, 769–795, doi: 10.1007/s10712-013-9224-4.

Suszcynsky, D. M., R. Roussel-Dupré, W. A. Lyons, and R. A. Armstrong (1998), Blue-light imagery and photometry of sprites, *J. Atmos. Sol.-Terr. Phys.*, *60*, 801–809, doi:10.1016/S1364-6826(98)00027-3.

Tarasova, L. V., and L. N. Khudyakova (1970), X-Rays from Pulsed Discharges in Air, *Sov. Phys.-Tech. Phys.*, *14*, 1048.

Vallance Jones, A. V. (1974), *Aurora, D. Reidel, Norwell, Mass.*

Vitello, P. A., B. M. Penetrante, and J. N. Bardsley (1994), Simulation of negative-streamer dynamics in nitrogen, *Phys. Rev. E*, *49*, 5574–5598, doi: 10.1103/PhysRevE.49.5574.

Wescott, E. M., D. D. Sentman, M. J. Heavner, D. L. Hampton, W. A. Lyons, and T. Nelson (1998), Observations of 'Columniform' sprites, *J. Atmos. Sol.-Terr. Phys.*, *60*, 733–740, doi:10.1016/S1364-6826(98)00029-7.

Wilson, C. T. R. (1925), The Acceleration of $\beta$-particles in Strong Electric Fields such as those of Thunderclouds, *Proceedings of the Cambridge Philosophical Society*, *22*, 534, doi:10.1017/S0305004100003236.

Winckler, J. R., R. C. Franz, and R. J. Nemzek (1993), Fast low-level light pulses from the night sky observed with the SKYFLASH program, *J. Geophys. Res.*, *98*, 8775–8783, doi:10.1029/93JD00198.

Xu, W., S. Celestin, and V. P. Pasko (2014), Modeling of X-ray emissions produced by stepping lightning leaders, *Geophys. Res. Lett.*, *41*, doi: 10.1002/2014GL061163.

Xu, W., S. Celestin, and V. P. Pasko (2015), Optical emissions associated with terrestrial gamma ray flashes, *J. Geophys. Res.*, *120*, 1355–1370, doi: 10.1002/2014JA020425.

Zalesak, S. T. (1979), Fully multidimensional flux-corrected transport algorithms for fluids, *J. Comput. Phys.*, *31*, 335–362, doi:10.1016/0021-9991(79)90051-2.

Zheleznyak, M. B., A. K. Mnatsakanian, and S. V. Sizykh (1982), Photoionization of nitrogen and oxygen mixtures by radiation from a gas discharge, *High Temp.*, *20*, 357–362.

Mohand Ameziane Ihaddadene

# Modélisation Numérique des Décharges Streamers pour la Préparation à la Mission Spatiale TARANIS

Résumé :

Les sprites sont de gigantesques phénomènes lumineux qui sont produits entre 40 et 90 km d'altitude généralement par des éclairs nuage-sol positifs. Les sprites sont des phénomènes très brefs (durée de quelques millisecondes) qui appartiennent à la famille des TLEs (évènements lumineux transitoires) et qui sont composés de structures filamentaires nommées streamers. Les streamers sont des filaments de plasma, qui se propagent à des vitesses allant jusqu'à $\sim 10^7$ m/s et qui possèdent des champs électriques trés forts souvent proches de 150 kV/cm (champs réduit à la pression atmosphérique). Lors de ce travail, on a développé un modèle fluide de plasma qui simule les décharges streamers couplées avec un modèle simulant les émissions optiques afin d'étudier la physique des streamers, des TLEs et plus particulièrement des sprites dans le cadre de la mission spatiale TARANIS. Cette mission a pour objectif d'étudier le système Atmosphére-Ionosphére-Magnetosphére, et observera les TLEs et leurs émissions associées: électromagnétiques, optiques, et probablement radiations énergétiques depuis le nadir. Dans cette thèse, on propose d'étudier certains problèmes liés aux streamers et aux sprites qui sont cruciaux pour préparer la mission TARANIS. Plus particulièrement nous abordons certains mécanismes de production de radiations énergétiques par les streamers récemment proposés dans la littérature et nous developpons une méthode qui permet de déterminer l'altitude, la vitesse et le champ électrique des streamers des sprites, à partir d'une analyse spectroscopique de leurs émissions optiques. Nos résultats renforceront donc le retour scientifique des futures missions spatiales observant les TLE depuis le nadir et particulièrement TARANIS.

Mots clés : Sprites, TLEs, streamers, et rayons X.

# Numerical Modeling of Streamer Discharges in Preparation of the TARANIS Space Mission

Abstract :

Sprites are large optical phenomena usually produced between 40 and 90 km altitude generally by positive cloud-to-ground lightning (+CG). These are short lifetime phenomena (duration of few milliseconds) that belong to the family of transient luminous events (TLEs) and composed of complex filamentary structures called streamers. Streamers are non-thermal plasma filament, highly collisional, propagating with velocities up to $10^7$ m/s, and characterized with high electric fields at their heads often close to 150 kV/cm when scaled to ground level air. In this work, we have developed a streamer plasma fluid model coupled with an optical emission model to investigate the physics of streamers and sprites in the framework of the TARANIS space mission. TARANIS will observe TLEs from a nadir-viewing geometry along with their related emissions (electromagnetic and particles). In this dissertation, we investigate some mechanisms of emission of energetic radiation from streamers recently proposed in the literature and we present an original spectroscopic method to determine sprite streamers altitudes, velocities, and electric fields through their optical emissions. This method is especially useful for increasing the scientific return of space missions that have adopted nadir-based observation strategies.

Keywords : Sprites, TLEs, streamers, runaway electrons and X-rays.

**Laboratoire de Physique et de Chimie de l'Environement et de l'Espace (LPC2E), 3A, Avenue de la Recherche Scientifique, 45071, Orléans, Cedex 02**